

PETROPHYSICAL ANALYSIS OF CARBONATED WATER INJECTION  
EFFECTS ON LACUSTRINE CARBONATES OF MUPE MEMBER,  
LOWER PURBECK GROUP (UPPER JURASSIC), UK

Isabela Dantas de Albuquerque

Dissertation presented to the National Observatory's  
Graduate Program in Geophysics in partial fulfillment  
of the requirements for the degree of Master in  
Geophysics.

Advisor: Dr. Fábio Pinto Vieira

Co-advisors: Dr. Silvia Lorena Bejarano Bermudez  
Dr. Claudio Rabe  
Dr. Giovanni Chaves Stael

Rio de Janeiro  
September 2022

Abstract of the Dissertation presented to the National Observatory's Graduate Program in Geophysics as a partial fulfillment of the requirements for the degree of Master in Geophysics.

## Petrophysical analysis of carbonated water injection effects on lacustrine carbonates of Mupe Member, lower Purbeck Group (Upper Jurassic), UK

Isabela Dantas de Albuquerque

September/2022

This research studies the dissolution and mineralogical alteration caused by carbonated water injection (CWI) and its effects on the petrophysical properties (porosity and permeability) of limestone samples from the Mupe Member, composed of lacustrine microbialites from the Upper Jurassic, part of the Purbeck Group lower portion, located in southern England and northern France. These limestones are a partial analogue of the Brazilian pre-salt Aptian carbonates, the most important oil reservoir in the country and which presents large amounts of CO<sub>2</sub> that is reinjected into the reservoir (which, given the high reactivity of carbonate rocks in the presence of carbonic acid generated by the reaction between CO<sub>2</sub> and water, can cause damage to the formation). Due to the few studies carried out so far directly related to the theme using these rocks, this research is presented as interesting and relevant.

To achieve the proposed objectives, the samples (four with low permeability values and two with very high permeability) underwent laboratory tests carried out before and after the carbonated water (desulphated sea water saturated by CO<sub>2</sub>) coreflood. The tests aimed to characterize (1) the porous space of the rock through quantification of the volume of grains, total porosity and permeability to gas (via routine petrophysical tests), characterization of the pore size distribution (with the use of nuclear magnetic resonance - NMR) and 3D imaging of the porous space in detail (through X-ray computed microtomography or micro-CT) and (2) the chemical and mineralogical composition through powder X-ray diffraction – XRD (identify all the mineral phases present in the samples on a macro level) and description of petrographic thin sections (allows the interpreter to analyze in detail the mineralogy of the rock and characterize the type of porosity, in order to assist in the identification of the porous space by micro-CT imaging).

After characterization, a single-phase flow of saline carbonated water was carried out to identify the physical-chemical and petrophysical changes generated by the CO<sub>2</sub> interaction with the rock (different pore volumes were injected in each sample). These changes are vital for optimizing CO<sub>2</sub> injection rates in carbon sequestration projects. During percolation, the effluent brine was sampled periodically, and ion chromatography identified elements added to the fluid due to the reaction with the rock.

Finally, post-injection tests of the plugs were carried out, performing some of the analyzes mentioned above to compare the results and identify the chemical and petrophysical alterations – changes in the values obtained by the routine petrophysical tests, variations in the pore size distribution obtained by NMR and visible changes by micro-CT in the porous space – generated by the carbonated water coreflooding.

The experimental results show that samples with high permeability showed a small decrease in permeability, indicating formation damage, while low permeability samples presented a significant increase in permeability with little change in porosity, indicating feasibility for Carbon Capture and Storage (CCS) in similar samples in likewise conditions. For samples with more pore volumes injected, the pressure stabilization seems to have favored dissolution in the later injection stages, indicated by the highest output of calcium ions in the effluent brine. Salt precipitation presented itself as a possible issue, especially in more heterogeneous rocks.

Resumo da Dissertação apresentada ao Programa de Pós-Graduação em Geofísica do Observatório Nacional como parte dos requisitos necessários para a obtenção do título de Mestre em Geofísica.

## Petrophysical analysis of carbonated water injection effects on lacustrine carbonates of Mupe Member, lower Purbeck Group (Upper Jurassic), UK

Isabela Dantas de Albuquerque

Setembro/2022

Esta pesquisa estuda a dissolução e alteração mineralógica causada pela injeção de água carbonatada e seus efeitos nas propriedades petrofísicas (porosidade e permeabilidade) de amostras de calcários do Membro Mupe, compostos por microbialitos lacustres do Jurássico Superior, parte da porção inferior do Grupo Purbeck, localizado no sul da Inglaterra e norte da França. Estes calcários são um análogo parcial dos carbonatos aptianos do pré-sal brasileiro, o qual é o mais importante reservatório de petróleo do país e que apresenta grandes quantidades de CO<sub>2</sub> que é reinjetado no reservatório (o que, dada a alta reatividade de rochas carbonáticas em presença de ácido carbônico gerado pela reação entre CO<sub>2</sub> e água, pode gerar danos à formação). Em virtude dos poucos estudos realizados até o momento diretamente relacionados ao tema utilizando estas rochas, esta pesquisa apresenta-se como interessante e relevante.

Para alcançar os objetivos propostos, as amostras (quatro com baixas permeabilidades e duas com altíssimas permeabilidades) passaram por ensaios laboratoriais realizados antes e depois da percolação de água carbonatada (água dessulfatada saturada com CO<sub>2</sub>). Os ensaios objetivaram caracterizar (1) o espaço poroso da rocha através da quantificação do volume de grãos, porosidade e permeabilidade totais a gás (via ensaios petrofísicos de rotina), caracterização da distribuição do tamanho de poros (com uso da ressonância magnética nuclear – RMN) e imageamento 3D do espaço poroso em detalhe (através da microtomografia computadorizada de raios-X ou micro-CT) e (2) a composição química e mineralógica através difração de raios-X em pó – DRX (identifica todas as fases minerais presentes nas amostras em nível macro) e descrição petrográfica da lâmina delgada (permite ao intérprete analisar em

detalhe a mineralogia da rocha e caracterizar o tipo de porosidade, de modo a auxiliar na identificação do espaço poroso pelo imageamento via micro-CT).

Após a caracterização, foi realizado um escoamento monofásico de água carbonatada salina com objetivo de identificar as alterações físico-químicas e petrofísicas geradas pela interação do CO<sub>2</sub> com a rocha (diferentes volumes de poros foram injetados em cada amostra). Estas mudanças são vitais para otimização de taxas de injetividade de CO<sub>2</sub> em projetos de sequestro de carbono. Durante a percolação, a salmoura efluente foi amostrada periodicamente e cromatografia iônica identificou elementos adicionados ao fluido devido à reação com a rocha.

Por fim, foram realizados ensaios pós-percolação dos plugues, realizando algumas das análises citadas anteriormente com o objetivo de comparar os resultados e identificar as alterações químicas e petrofísicas – alteração nos valores obtidos pelos ensaios petrofísicos de rotina, variação da distribuição do tamanho de poros obtidos pela RMN e mudanças visíveis por micro-CT no espaço poroso – geradas pela percolação de água carbonatada.

Os resultados experimentais mostraram que as amostras com altas permeabilidades apresentaram uma pequena diminuição na permeabilidade, indicando dano na formação, enquanto amostras de baixa permeabilidade apresentaram um aumento significativo na permeabilidade com pouca alteração na porosidade, indicando viabilidade para armazenamento de carbono em amostras semelhantes e em condições semelhantes. Para amostras com mais volumes de poros injetados, a estabilização da pressão parece ter favorecido a dissolução nas etapas posteriores da injeção, indicada pela maior saída de íons de cálcio na salmoura efluente. A precipitação de sal apresentou-se como um possível problema, especialmente em rochas mais heterogêneas.

# Acknowledgments

To my advisors Fabio Pinto Vieira, Silvia Bermudez, Claudio Rabe, and Giovanni Stael for all their support and encouragement.

To the National Observatory and the Brazilian National Council for Scientific and Technological Development (CNPq) for their institutional and financial support.

To Baker Hughes for donating the samples used in this research.

To André Albernaz for the routine petrophysics analyses at the Petrophysics Laboratory of the National Observatory (LabPetrON).

To the team from the Advanced Petroleum Recovery Laboratory (LRAP/UFRJ): Paulo Couto for allowing most of the tests of this dissertation to be carried out in the laboratory, Agatha Densy and Douglas Silva de Almeida for the routine petrophysics analyses, Edmilson Helton Rios for the NMR measurements, Maira Lima for the micro-CT imaging, Anete Coelho and Monica Sant'anna for the chromatography analyses, Carlos Cordeiro Junior, Heitor Leite, Denise Nunes and Felipe Eler for the coreflood injection, and Fernanda Hoerlle and all the others for the guidelines and explanations.

To the team at the Mineral Technology Center (CETEM/UFRJ): Reiner Neumann for allowing the XRD analysis to be carried out at CETEM and for the results refinement and Josimar Firmino de Lima for the samples' processing and analysis.

To the team at the Geological Laboratory for Sample Processing (LGPA/UERJ): Núbia Maria da Silva for making the petrographic thin sections and Vitalino Elizeu for receiving the order.

To Luiz Guilherme Eirado for allowing me to use the Petrography Laboratory at UERJ to perform the petrographic thin sections description.

To my fellow graduate students at the National Observatory, especially Patricia Descovi, for their support and friendship.

And, last but not least, to my parents, Antonio and Estela, and my brother, Vitor, for all their support throughout my trajectory in the master's degree. This achievement is also yours!

# List of Figures

Figure 1. Diagram explaining parameters in the Darcy equation for incompressible liquid (MCPHEE *et al.*, 2015). .....24

Figure 2. Idealized representation of water-wet and oil-wet reservoirs with depositional, interparticle porosity. All rocks had to be water-wet originally, but some became oil-wet after hydrocarbon migration, and surface chemical reactions between the hydrocarbons and the pore walls caused the rock to become oil-wet. This is especially true of carbonate reservoirs with oils containing polar organic compounds that react with carbonates (AHR, 2011).....25

Figure 3. Folk’s (1962) textural spectrum for carbonate sediments records 8 phases of sorting and rounding with the intent of capturing the deposition settings from low energy (left) to high energy (right). In very low-energy settings, micrites or mud-sized carbonate accumulate; in intermediate-energy settings, micrites with greater concentrations of allochemical particles, winnowed grain, and mud accumulations result; in high-energy settings, sorting and rounding of grains winnow most of the micrite matrix away. Textural inversions are the result of storm events that mix sediments from different settings or introduce short-lived conditions into a normally low-energy setting (KENDALL *et al.*, 2011). .....26

Figure 4. R. J. Dunham’s 1962 classification of carbonate rocks is intended to convey information related to their depositional setting. Carbonates that are supported by matrix (mud) or framework (grains) form the basis of this classification. The end members include noncrystalline limestones often characterized by referencing the major component grains (DUNHAM, 1962 *apud* AHR, 2011; KENDALL *et al.*, 2011).....26

Figure 5. Embry and Klovan (1971) modification of the Dunham’s (1962) biologic classification of organically bound rocks. “Floatstone” replaces Dunham’s “packstone”; the term “rudstone” replaces grain-supported biogenic limestones, and other organically bound rock are termed “bafflestone,” “bindstone,” or “framestone,” depending on the character of the organic structures. These latter terms are often used to describe the fabric of reefs, bioherms, and other biogenic carbonates (KENDALL *et al.*, 2011).....27

Figure 6. Microbial carbonates defined by macrofabric: leiolite (aphanitic), stromatolite (laminated), thrombolite (clotted), dendrolite (dendritic). Examples show domes and associated sediment. Not to scale. All categories are integrational. In addition to

domes/mounds, overall shape can include columns, layers, and irregular masses. A complication is that leiolite and stromatolite macrofabrics are defined by features within (i.e., internal to) the microbial carbonate, such as lamination. In contrast, thrombolite and dendrolite macrofabrics are defined by the external shape of individual masses of microbial carbonate, such as clots or small shrub-like masses. Thrombolitic stromatolite (Aitken, 1967), typified by some Shark Bay columns, is internally weakly clotted and crudely laminated. It is essentially agglutinated, in contrast to Neoproterozoic and early Palaeozoic thrombolites with calcified microbial microfabrics. In the latter, the clots may be prostrate and irregular, and also vertically extended into amalgamated elongate branches (e.g., Favosamaceria) (RIDING, 2011).....27

Figure 7. Porosity classification of CHOQUETTE and PRAY (1970). Taken from <https://www.saltworkconsultants.com/carbonate-porosity-choquette-and-pray/>.....28

Figure 8. Left: CO<sub>2</sub> solubility in water (PERKINS, 2003); Right: CO<sub>2</sub> solubility in brine relative to that in pure water, showing experimental points reported by ENICK and KLARA (1990) and correlation developed by IPCC (2005) (TDS stands for total dissolved solids). .29

Figure 9. Carbon dioxide phase diagram (Wikipedia). .....30

Figure 10. Conceptual scheme of calcite and dolomite solubility changes as affected by various factors. (a) Temperature effect, °C (at CO<sub>2</sub> pressure of 0.1 MPa), (b) CO<sub>2</sub> content effect (at temperature 25°C), and (c) Effect of CaSO<sub>4</sub> content in solution, at CO<sub>2</sub> pressure of 0.00012 MPa and temperature 25°C (after SOKOLOV, 1965 *apud* BAGRINTSEVA, 2015). .....31

Figure 11. Graphic depiction of CO<sub>2</sub> density changes with depth. ....32

Figure 12. Summary of the carbon capture and storage process (<https://ec.europa.eu/jrc/en/research-topic/carbon-capture-utilisation-and-storage>). .....33

Figure 13. Evolution of CO<sub>2</sub> storage mechanisms through time. The horizontal axis shows the time since the start of injection; the right vertical axis shows the trapping contribution percentage of the four main storage mechanisms; the left vertical axis shows the qualitative evolution of CO<sub>2</sub> storage mechanisms. The dashed line represents the simulation time of this study and percentage contribution of the CO<sub>2</sub> storage mechanisms. Modified from IPCC (2005) (Veloso *et al.*, 2016). .....34

Figure 14. CO<sub>2</sub> miscible process (GREEN and WILLHITE, 2018; DOE/NTL, 2010 *apud* PIZARRO and BRANCO, 2012). .....35

Figure 15. Snapshot of the concentration field during the unstable displacement of a more viscous fluid (dark) by a fully-miscible, less viscous fluid (light) (<http://news.mit.edu/2011/fluid-mixing-0519>). .....36

Figure 16. Overview of core analysis directed on reservoir properties (SCHÖN, 2015). .....39



Figure 17. Schematic flow diagram of permeameter (TIAB E DONALDSON, 2015).....	41
Figure 18. Illustrative scheme of CT acquisition workflow: (a) setup of $\mu$ -CT scanner for image acquisition, (b) set of single radiographic projections, (c) stack of 2D raw gray-scale horizontal image slices, and (d) volume reconstructed (LEIDERMAN <i>et al.</i> , 2017; ORHAN, 2020).....	42
Figure 19. $T_1$ -relaxation (polarization) curves indicate the degree of proton alignment, or magnetization, as a function of the time that a proton population is exposed to an external magnetic field. $M(t)$ is the magnitude of magnetization at time $t$ when the direction of $B_0$ is taken along the $z$ -axis and $M_0 =$ the final and maximum magnetization in a given magnetic field (COATES <i>et al.</i> , 1999).....	44
Figure 20. After the application of a $90^\circ$ pulse, the proton population dephases, and a free induction decay (FID) signal can be detected (COATES <i>et al.</i> , 1999).....	44
Figure 21. To generate a spin-echo train, the CPMG pulse sequence is used, which consists of a $90^\circ B_1$ pulse followed by a sequence of $180^\circ B_1$ pulses. Spin echoes of decreasing amplitude follow the $180^\circ B_1$ pulses (COATES <i>et al.</i> , 1999).....	45
Figure 22. The amplitudes of the decaying spin echoes yield an exponentially decaying curve with time constant $T_2$ (COATES <i>et al.</i> , 1999).....	45
Figure 23. Through echo fitting, the echo train (echo amplitude as a function of time) is mapped to a $T_2$ distribution (porosity as a function of $T_2$ ) (COATES <i>et al.</i> , 1999).....	46
Figure 24. 100% water-saturated pore (upper left) has a single $T_2$ value (upper center) that depends on pore size, and thus its spin-echo train exhibits a single-exponential decay (upper right) that also depends on pore size. Multiple pores at 100% water saturation (bottom left) have multiple $T_2$ values (bottom center) that depend on the pore sizes, and thus their composite spin-echo train exhibits multi-exponential decay (bottom right) that also depends on the pore sizes (COATES <i>et al.</i> , 1999).....	47
Figure 25. Schematic representation of the geometry of a conventional powder diffractometer (POPPE <i>et al.</i> , 2001).....	48
Figure 26. Evolution of onshore and offshore production - Pre-salt x Post-salt x Onshore...50	50
Figure 27. Distribution of oil production by basin. Source: March 2022 ANP's Oil and Natural Gas Production Bulletin.....	50
Figure 28. Distribution of natural gas production by basin. Source: March 2022 ANP's Oil and Natural Gas Production Bulletin.....	50
Figure 29. Tectonic reconstruction of sedimentary basins in the pre-drift configuration (124 million years ago) (MOHRIAK, 2003). .....	51
Figure 30. Generalized tectonostratigraphic evolution chart for the Campos and Santos basins.	

(Modified from BEGLINGER <i>et al.</i> , 2012).....	51
Figure 31. CO <sub>2</sub> concentration map on the east margin, with structural framework (D'ALMEIDA <i>et al.</i> , 2018).....	53
Figure 32. Location and geological setting. (A) Purbeck Limestone Group (red) exposures in UK and France; (B) Structural map of the Channel and Wessex Basins and sub-basins. The thick lines identify Mesozoic extensional faults inverted during the Alpine orogeny; (C) Simplified geological map of south Dorset with inverted faults (bold black lines) and associated anticlines (Modified from GALLOIS <i>et al.</i> , 2018). .....	54
Figure 33. Purbeck Limestone Group formations, members and beds and idealized log for the Mupe Member in the Isle of Portland (UK), according to GALLOIS (2016). .....	55
Figure 34. Size comparison between the Wessex Basin (A) and South Atlantic basins (B) (redrawn after CHABOUREAU <i>et al.</i> , 2013 <i>apud</i> GALLOIS, 2016). .....	56
Figure 35. Comparison of basin evolutions between Brazilian margin basins (modified after MOREIRA <i>et al.</i> , 2007), the Wessex Basin of southern England (modified after Underhill, 1998) and West African margin basins (modified after BEGLINGER <i>et al.</i> , 2012). The red areas highlight intervals of GALLOIS (2016) study and their counterparts in the South Atlantic. Modified from GALLOIS (2016). .....	57
Figure 36. Effective pore throat diameter and the corresponding mercury capillary pressure as functions of cumulative pore space inferred from mercury injection tests on Purbeck undeformed samples. ....	60
Figure 37. Pore size distribution calculated with logarithmic derivative $dS/d(\ln P)$ , inferred from mercury injection measurements in Purbeck samples, showing bimodal distribution. .	60
Figure 38. T <sub>2</sub> relaxation time distribution, $f(T_2)$ (dashed black line), and the T <sub>2</sub> -weighted probability distribution function, T <sub>2</sub> $f(T_2)$ (solid red line), inferred from NMR measurements on undeformed Purbeck samples (WANG <i>et al.</i> , 2018).....	60
Figure 39. Samples analyzed by XRD; IS-1 (left) represents the vuggy facies and and IS-2 (right) represents the laminated/massive facies. ....	62
Figure 40. Photos of plugs taken from the selected five blocks.....	63
Figure 41. (a) drilling press diamond tool from Corelab Instruments; (b) trim saw from Corelab Instruments; (c) chapel with hot Soxhlet equipment.....	63
Figure 42. LRAP's porosimeter and permeameter. Source: LRAP. ....	64
Figure 43. Plugs with extremely low porosity (below 3%) and permeability (close to 0 mD). .....	65
Figure 44. Plugs with the possibility of grains loosening.....	65
Figure 45. Plugs that follow to the next steps of analysis.....	65

Figure 46. Blocks from which the plugs that proceeded in the analysis were removed. ....	66
Figure 47. LabPetrON's sample saturator.....	67
Figure 48. LAGEP's NMR equipment. ....	67
Figure 49. LRAP's NMR equipment.....	67
Figure 50. LRAP's micro-CT equipment. Source: Tescan. ....	67
Figure 51. Schematic sequence of Micro-CT image processing performed in Fiji software (ImageJ). ....	68
Figure 52. Schematic depiction of the apparatus used for DSW, CSW and DW injection, provided by LRAP team. ....	69
Figure 53. Schematic drawing of the CSW preparation, provided by LRAP team. ....	69
Figure 54. Scan of the IS-ON-1 thin section generated manually by pasting photos in mosaic style. The photos were obtained in a petrographic microscope under polarized light, with a 2.5x magnification. ....	74
Figure 55. Scan of the IS-ON-2 thin section generated manually by pasting photos in mosaic style. The photos were obtained in a petrographic microscope under polarized light, with a 2.5x magnification. ....	75
Figure 56. Brownish nodular crystals under natural light (left) and radial extinction cross under polarized light (right) in thin section IS-ON-1, with a 10x magnification. GALLOIS (2016) interpreted these crystals as chalcedony spherules, the result of the recrystallization of the micritic matrix. ....	76
Figure 57. Detail of the IS-ON-1 scan image, highlighting the parts rich in micritic matrix with sparse chalcedony spherules and the porous regions with sparry calcite with well-formed calcite crystals on the walls of the vugular pores, in addition to the presence of moldic pores generated by the dissolution of fossil shell (likely bivalve). ....	76
Figure 58. Detail of the IS-ON-2 scan image, highlighting the branched columnar thrombolytic structure with poorly marked laminations. ....	77
Figure 59. Correlation between helium porosity and NMR porosity (before and after CWI). ....	80
Figure 60. NMR T <sub>2</sub> distribution before CWI.....	80
Figure 61. NMR T <sub>2</sub> distribution after CWI.....	80
Figure 62. Sample 1X incremental and cumulative porosity before CWI. ....	81
Figure 63. Sample 3Y incremental and cumulative porosity before CWI. ....	81
Figure 64. Sample 3Z incremental and cumulative porosity before CWI. ....	81
Figure 65. Sample 6X incremental and cumulative porosity before CWI. ....	81
Figure 66. Sample 6Y incremental and cumulative porosity before CWI. ....	81

Figure 67. Sample 6Z incremental and cumulative porosity before CWI. ....	81
Figure 68. Sample 1X incremental and cumulative porosity after CWI. ....	82
Figure 69. Sample 3Y incremental and cumulative porosity after CWI. ....	82
Figure 70. Sample 3Z incremental and cumulative porosity after CWI.....	82
Figure 71. Sample 6X incremental and cumulative porosity after CWI. ....	82
Figure 72. Sample 6Y incremental and cumulative porosity after CWI. ....	82
Figure 73. Sample 6Z incremental and cumulative porosity after CWI.....	82
Figure 74. Sample 1X pre and post-CWI incremental porosity.....	83
Figure 75. Sample 3Y pre and post-CWI incremental porosity.....	83
Figure 76. Sample 3Z pre and post-CWI incremental porosity. ....	83
Figure 77. Sample 6X pre and post-CWI incremental porosity.....	83
Figure 78. Sample 6Y pre and post-CWI incremental porosity.....	83
Figure 79. Sample 6Z pre and post-CWI incremental porosity. ....	83
Figure 80. Sample 1X pre and post-CWI cumulative porosity.....	84
Figure 81. Sample 3Y pre and post-CWI .....	84
Figure 82. Sample 3Z pre and post-CWI.....	84
Figure 83. Sample 6X pre and post-CWI .....	84
Figure 84. Sample 6Y pre and post-CWI .....	84
Figure 85. Sample 6Z pre and post-CWI.....	84
Figure 86. Schematic drawing of the images obtained by Micro-CT in relation to plugs. ....	85
Figure 87. Sample 1X micro-CT images.....	86
Figure 88. Sample 3Y micro-CT images.....	87
Figure 89. Sample 3Z micro-CT images. ....	88
Figure 90. Sample 6X micro-CT images.....	89
Figure 91. Sample 6Y micro-CT images.....	90
Figure 92. Sample 6Z micro-CT images. ....	91
Figure 93. 1X micro-CT porosity variation along the sample's length.....	92
Figure 94. 3Y micro-CT porosity variation along the sample's length.....	93
Figure 95. 3Z micro-CT porosity variation along the sample's length. ....	93
Figure 96. 6X micro-CT porosity variation along the sample's length.....	94
Figure 97. 6Y micro-CT porosity variation along the sample's length.....	94
Figure 98. 6Z micro-CT porosity variation along the sample's length. ....	95
Figure 99. Images from plug 1X's base, closer to the inlet face. Top left: pre-CWI; Top right: post-CWI; Bottom left: the post-CWI image above and pre-CWI image below in red (material lost), highlighting porosity increase; Bottom right: the pre-CWI image above and post-CWI	

image below in yellow (material gained), highlighting porosity decrease. ....	96
Figure 100. 3D image of pores from plug 1X's 15 cm from its base, including 60 slices (16 below the slice in Fig. 8 and 43 slices above it). The magenta arrows indicate the main areas where dissolution occurs due to pore narrowing and the yellow arrows indicate precipitation areas due to an increase in pore size, which causes flow deceleration. ....	97
Figure 101. Thread seal tape pellets placed in the vuggs of sample 3Y. ....	98
Figure 102. Differential pressure variation through injection time in sample 6Y. ....	100
Figure 103. Permeability variation through injection time in sample 6Y. ....	100
Figure 104. Differential pressure variation through injection time in sample 6X. ....	101
Figure 105. Permeability variation through injection time in sample 6X. ....	101
Figure 106. Differential pressure variation through injection time in sample 6Z. ....	102
Figure 107. Permeability variation through injection time in sample 6Z. ....	102
Figure 108. Differential pressure variation through injection time in sample 3Z. ....	103
Figure 109. Permeability variation through injection time in sample 3Z. ....	103
Figure 110. Differential pressure variation through injection time in sample 1X. ....	104
Figure 111. Permeability variation through injection time in sample 1X. ....	104
Figure 112. Differential pressure variation through injection time in sample 3Y. ....	105
Figure 113. Permeability variation through injection time in sample 3Y. ....	105
Figure 114. Cations and anions concentration, in ppm, from 6Y and 6X samples effluents. Dotted lines indicate the concentrations of each element in the injected DSW for comparison. ....	108
Figure 115. Cations and anions concentration, in ppm, from 6Z and 3Y samples effluents. Dotted lines indicate the concentrations of each element in the injected DSW for comparison. ....	109
Figure 116. Cations and anions concentration, in ppm, from 1X and 3Y samples effluents. Dotted lines indicate the concentrations of each element in the injected DSW for comparison. ....	110
Figure 117. Difference between the amount (in ppm) of Ca and Mg that outflowed from the sample and the amount that was injected. Positive values indicate dissolution of calcium minerals (especially calcite) and magnesium minerals (possibly dolomite) and negative values indicate precipitation of these minerals. ....	111
Figure 118. Difference between the amount (in ppm) of Cl, Na, K, and SO <sub>4</sub> that outflowed from the sample and the amount that was injected. Positive values indicate dissolution and negative values indicate salt precipitation. ....	112
Figure 119. Solubility of CO <sub>2</sub> in water (PERKINGS, 2003). Red curve and red dashed lines	

indicate CO <sub>2</sub> solubility under temperature and pressure conditions used in this research (3.45 MPa and 20°C); blue dotted lines indicate solubility under Brazilian pre-salt reservoir conditions (60 MPa and 80 to 100°C). .....	115
Figure 120. CO <sub>2</sub> solubility in brine relative to that in pure water, showing experimental points reported by ENICK and KLARA (1990) and correlation developed by METZ <i>et al.</i> (2005) (TDS stands for total dissolved solids). Red dashed lines indicate the CO <sub>2</sub> solubility under salinity conditions used in this research (30,500 mg/L or 3.05%); blue dotted lines indicate solubility under Brazilian pre-salt reservoir conditions (226,694 mg/L or 22.7%, according to FAÇANHA <i>et al.</i> , 2016).....	115

## List of Tables

Table 1. Petrophysical data from Purbeck limestone samples (GLOVER <i>et al.</i> , 2006). .....	58
Table 2. Petrophysical data from Purbeck limestone samples (NORTH <i>et al.</i> , 2013).....	58
Table 3. Petrophysical data from Purbeck limestone samples (CARVALHO <i>et al.</i> , 2019)...	58
Table 4. Purbeck sample composition by X-ray fluorescence (CARVALHO <i>et al.</i> , 2019)...	59
Table 5. Purbeck sample composition by X-ray fluorescence, with fractions of CaO and MgO converted to CaCO <sub>3</sub> and MgCO <sub>3</sub> , respectively (BLAMEY <i>et al.</i> , 2010).....	59
Table 6. Ionic composition (ppm), total dissolved solids TDS, pH, and density ( $\rho$ ) for the Desulphated Sea Water (DSW) used in this work, developed in LRAP. ....	70
Table 7. Activities performed, equipment/techniques and laboratories. ....	71
Table 8. Result of XRD analysis of IS-1 and IS-2 samples.....	73
Table 9. Purbeck plugs routine petrophysical data pre and post-CWI, obtained at LRAP. ...	78
Table 10. Difference in porosity and permeability before and after CWI. ....	79
Table 11. Results obtained from NMR measurements.....	79
Table 12. Average samples' micro-CT porosity before and after CWI. ....	95
Table 13. Gas and DSW permeability and pore volume for each sample before CWI and pore volumes of CW injected in each sample.....	98
Table 14. Pressure and permeability values in the beginning and of CW injection and permeability increase for each sample.....	99
Table 15. Ion chromatography results. ....	106
Table 16. Gas porosity variation, gas permeability pre-CWI, gas permeability variation, total volume of carbonated water (CW) injected and calcium output for each sample. ....	113

# Summary

## Chapter 1

<b>Introduction</b> .....	<b>18</b>
1.1. Research justification .....	20
1.2. Objectives of this research.....	20

## Chapter 2

<b>Literature review</b> .....	<b>22</b>
<b>2.1. Fundamentals</b> .....	<b>22</b>
2.1.1. Petrophysical properties .....	22
2.1.1.1. Porosity.....	22
2.1.1.2. Permeability .....	23
2.1.1.3. Saturation.....	24
2.1.2. Carbonate rocks.....	25
2.1.2.1. Porosity classification.....	28
2.1.3. CO <sub>2</sub> chemical properties .....	29
2.1.3.1. Carbonate Rocks Dissolution.....	30
2.1.4. Carbon Capture and Storage (CCS) .....	31
2.1.5. Enhanced Oil Recovery .....	34
2.1.5.1. CO <sub>2</sub> EOR .....	35
2.1.6. Carbonated Water Injection (CWI).....	36
2.1.7. Formation damage.....	38
<b>2.2. Equipment</b> .....	<b>39</b>
2.2.1. Core analysis .....	39
2.1.1.1. Routine Core Analysis (RCAL).....	40
2.1.1.1.1. Grain density and porosity measurements.....	40
2.1.1.1.2. Permeability measurement .....	40
2.1.1.1.3. X-Ray Computed Microtomography (micro-CT or $\mu$ -CT) .....	42
2.1.1.2. Special Core Analysis (SCAL) .....	43
2.1.1.2.1. Nuclear Magnetic Resonance (NMR) .....	43
2.1.1.2.2. X-ray Powder Diffraction (XRD) .....	47
<b>2.2. Geological Setting</b> .....	<b>49</b>
2.2.1. Brazilian pre-salt .....	49

2.2.1.1.	CO <sub>2</sub> occurrence and concentrations in pre-salt fields .....	52
2.2.2.	Purbeck limestones.....	53
	The Purbeck Limestone Group: an analogue to the Brazilian pre-salt .....	55
2.2.2.1.	Petrophysical studies in Purbeck limestones .....	57
<b>Chapter 3</b>		
<b>Materials and Methods.....</b>		<b>61</b>
3.1.	Chemical and mineralogical characterization.....	61
3.1.1.	X-ray diffraction (XRD).....	61
3.1.1.	Petrographic thin sections.....	62
3.2.	Plugs preparation .....	62
3.2.1.	Coring and cleaning.....	62
3.3.	Pre-injection analysis .....	64
3.3.1.	Routine petrophysics .....	64
3.3.2.	Nuclear Magnetic Resonance (NMR) .....	66
3.3.3.	X-Ray Computed Microtomography (micro-CT or $\mu$ -CT) .....	67
3.4.	Carbonated water injection.....	68
3.4.1.	Ion chromatography (IC).....	71
3.5.	Post-injection analysis.....	71
<b>Chapter 4</b>		
<b>Results and discussion .....</b>		<b>73</b>
4.1.	X-ray diffraction (XRD).....	73
4.2.	Thin sections.....	73
4.3.	Routine petrophysics .....	77
4.4.	NMR results.....	79
4.5.	Micro-CT results.....	85
4.6.	Carbonated Water Injection results.....	98
4.7.	Ion chromatography results .....	105
4.8.	Results correlation.....	112
4.9.	Brazilian Pre-salt applications .....	114
<b>Chapter 5</b>		
<b>Summary of results and Conclusions.....</b>		<b>116</b>
<b>References.....</b>		<b>119</b>



# Chapter 1

## Introduction

Petroleum is a non-renewable substance and source of energy of great importance, being the raw material for several important derivatives and being responsible for 58% of the world's and 46% of Brazil's energy generation (RITCHIE and ROSER, 2018; MME, 2019). Up to 60% of the world's conventional petroleum is found in carbonate rocks (BAGRINTSEVA, 2015), distributed in important fields such as the ones in the Middle East and the Brazilian pre-salt fields. The Brazilian pre-salt reservoirs are responsible for over 70% of the petroleum national production (ANP, 2022), generating billions in Brazilian currency in signature bonuses and royalties for the union and producer states.

Carbonate rocks are defined as rocks that contain more than 50% carbonate minerals (such as calcite and dolomite) formed by chemical precipitation from water or by the build-up of shells, bones, and teeth of organisms (OJOVAN and LEE, 2005). Unlike siliciclastic rocks (such as sandstones), which have most of their pore spaces originated during the sediments' deposition (primary porosity), the pore space formation and evolution in carbonate rocks are closely associated with dissolution and leaching processes (secondary porosity) due to higher solubility of calcareous minerals, forming a complex pore structure in these rocks (BAGRINTSEVA, 2015; TIAB E DONALDSON, 2015).

On average, only 30% of the oil present in a field is extracted using simpler techniques, such as depending on the original pressure of the reservoir or injecting water, and more when using enhanced oil recovery (EOR) techniques, such as injecting miscible gases or chemicals in the reservoir. However, due to the high reactivity of carbonate rocks, the application of EOR techniques can either increase oil recovery or cause damage to the reservoir rock (known as formation damage). To avoid formation damage, it is necessary to understand how the technique used affects the rock porous structure, and laboratory tests on rock samples are an important step in this study, as it allows, from the result of these, to construct realistic models to represent the petroleum field behavior (CIVAN, 2015; TIAB and DONALDSON, 2015).

Despite the importance of petroleum derivatives in the world energy matrix, it is recognized that its burning in large quantities is directly related to global warming (along with coal burning). According to the Paris Agreement signed in 2015, it was decided that greenhouse gas emissions (carbon dioxide being the main one) should be zeroed by 2050 (UNFCCC, 2018). Studies carried out by the International Energy Agency (IEA) show that it will not be possible to achieve this objective in this timespan only focusing on the transition to a fully renewable energy matrix, requiring the use of carbon capture and storage (CCS) in geological formations at the subsurface, which would allow for a smoother energy transition as it enables for the continued burning of oil without CO<sub>2</sub> emissions (IEA, 2020). As CCS is a financially costly process, it becomes more viable if injected into reservoirs to be used as an EOR method (known as CCUS or carbon capture, utilization, and storage).

Besides that, high concentrations of CO<sub>2</sub> were found in various Brazilian pre-salt fields and since it cannot be ventilated in the atmosphere or sold without having a part of the CO<sub>2</sub> removed – commercial specifications require a maximum CO<sub>2</sub> content of 3% in volume (ANP, 2008) –, the most viable option is to re-inject it into the reservoir. An example is Tupi shared reservoir, in the Santos Basin, whose CO<sub>2</sub> content in the gas produced varies from 8% to 25% (MME *et al.*, 2020) and since 2011 injected about 1Mt/yr (recently increasing to 4.6 Mt/ year), having reached by December 2017 the milestone of 7Mt of CO<sub>2</sub> injected into the oil fields Sapinhoá, Lapa and Tupi, Brazil's first supergiant oil field (GLOBAL CCS INSTITUTE, 2019, 2020).

In both cases (EOR and/or CCS), it is extremely important to understand how the gas reacts with the formation when injected into its pore space. However, due to the high costs of taking wholecore samples in wells, especially in Brazilian pre-salt carbonate deepwater wells, the usage of analogous reservoir rocks is common in the oil and gas industry. The Mupe Member, composed of Upper Jurassic lacustrine microbialites and associated facies formed in a semi-arid climate setting in an extensional basin, can be considered as a partial analogue for some aspects of the Brazilian pre-salt carbonate reservoirs “*as the deposits are approximately the same age, have a similar tectonic setting and basin evolution (both are pre-salt) and both have porous microbial mound facies*” (GALLOIS and BOSENCE, 2017).

This research studied the effects of brine and CO<sub>2</sub> injection in Mupe Member limestones, Purbeck Group. Some of the topics covered in this introduction are more detailed in Chapter 2 (Literature review), and the Methodology, Results and Discussions, and Conclusions are presented in Chapters 3, 4, and 5, respectively.

## 1.1. Research justification

Brazilian pre-salt, the most important oil reservoir in the country, presents large amounts of CO<sub>2</sub>, which is reinjected into the reservoir for being the most viable option, but also the most ecologically correct, considering that the emission of fossil fuels is directly related to climate change.

Since these reservoirs are composed of carbonate rocks, known for their structural complexity and high reactivity to carbonic acid (generated by the reaction between CO<sub>2</sub> and water), it is essential to understand how this acid changes the porous space of these rocks, where the extracted oil and gas are stored.

Due to the high cost of obtaining rock cores in Brazilian pre-salt carbonate deepwater wells, the usage of analogous reservoir rocks is common, and the UK's Mupe Member limestones, partial analogues of pre-salt rocks, present themselves as excellent objects of study to achieve this understanding. Furthermore, these rocks have extreme permeability values - very low and very high values -, characteristics that have been little studied in relation to the effects caused by the injection of carbonated water.

In addition, studies on the effects of carbonated water injection on the pore space of these rocks have not yet been published. Therefore, this research aimed to help fill this gap and improve understanding of the effects of carbonated water coreflood on these rocks, allowing to assess the risks of formation damage when applying this procedure.

## 1.2. Objectives of this research

The main objective of the research was to analyze the alterations generated by carbonated water coreflooding in permo-porous properties of Mupe Member's limestones samples.

To achieve the main objective, specific objectives are:

- **To characterize the samples' porous space** through (1) volume of grains, total porosity, and permeability to gas quantifications via routine petrophysical tests, (2) pore size distribution analysis with the use of nuclear magnetic resonance (NMR), and (3) pore space detailed 3D imaging through X-ray computed microtomography (micro-CT);
- **To characterize the mineralogy of the samples** through (1) powder X-ray diffraction (DRX), which identifies all the mineral phases present in the samples on the macro level, (2) description of the petrographic thin sections, which allows the interpreter to

## CHAPTER 1: INTRODUCTION

analyze in detail the mineralogy of the rock (and also characterize the type of porosity, with the aim of assist in the identification of the porous space by micro-CT imaging);

- **To perform carbonated water injection** in the selected samples and **assess the rock degree of reactivity** during injection through ion chromatography analysis in the effluent fluid;
- **To characterize qualitatively and quantitatively the petrophysical and mineralogical changes generated by carbonated water injection** in the samples via the repetition of routine petrophysical, NMR, and micro-CT analysis and comparison of the results obtained.

# Chapter 2

## Literature review

### 2.1. Fundamentals

---

#### 2.1.1. Petrophysical properties

The rock's void space measuring is defined as the porosity, and the rock's measured ability to transmit fluids is called permeability (TIAB and DONALDSON, 2015). These two rock properties dictate the mobile fluids quantities trapped within the rock and the ability of these fluids to flow through it. Other important reservoir properties include texture, the rock and its contained fluids resistivity to electrical current, water content as a function of capillary pressure, and the tortuous nature of the interstices or pore channels (TIAB and DONALDSON, 2015).

##### 2.1.1.1. Porosity

The void space between grains, called pore space or interstice, can be expressed in mathematical form as

$$\phi = \frac{V_b - V_{gr}}{V_b} = \frac{V_p}{V_b} \quad (1)$$

where

$\phi$  = porosity, fraction

$V_b$  = rock bulk volume

$V_{gr}$  = grain volume

$V_p$  = pore volume.

The porosities of petroleum reservoirs range from 5% to 30%, but most frequently are between 10% and 20% (TIAB and DONALDSON, 2015). Qualitatively, reservoir porosity values can be graded in the following manner (TIAB and DONALDSON, 2015):

Qualitative Description	Porosity Range
Negligible	< 5%
Poor	5 - 10%
Fair	10 - 15%
Good	15 - 20%
Very good	> 20%

**Absolute porosity** is the ratio of the total void space in the sample to the bulk volume of that sample, regardless of whether or not those void spaces are interconnected, while **effective porosity** only takes into consideration pores that are connected and, therefore, allows the flow of fluids in the pores. That way, a rock may have considerable absolute porosity and yet have no fluid conductivity for lack of pore interconnections (TIAB and DONALDSON, 2015).

### 2.1.1.2. Permeability

In addition to being porous, a reservoir rock must have the ability to allow hydrocarbon fluids to flow through its interconnected pores. This ability to conduct fluids is called **absolute permeability**, which is dependent on the rock's effective porosity and independent of the fluid present in the pore space (in single-phase flows, or with a single type of fluid).

Darcy's law is used to calculate the permeability of a porous medium and its generalized form is given as

$$v = \frac{Q}{A_c} = -\frac{k}{\mu} \frac{dp}{dl} \quad (2)$$

where

$v$  = fluid velocity, cm/s

$Q$  = flow rate, cm<sup>3</sup>/s

$A_c$  = cross-sectional area of the core sample, cm<sup>2</sup>

$k$  = permeability of the porous rock, Darcy (0.986923 μm<sup>2</sup>)

$\mu$  = viscosity of the fluid, centipoises (cP)

$l$  = length of the core sample, cm

$dp/dl$  = pressure gradient in the direction of the flow, atm/cm.

The equation (2) can also be expressed as

$$Q = \frac{k A_c}{\mu} \frac{dp}{dl} \quad (3).$$

Separating the variable and integrating between 0 and L and inlet pressure  $P_1$  and outlet

pressure  $P_2$ , and solving for  $k$  gives

$$k = \frac{Q\mu L}{(p_1 - p_2)A_c} \quad (4)$$

where  $k$  is measured by causing a fluid to flow through a clean and dry core sample (plug) of measured dimensions ( $A_c$  and  $L$ ), as represented in Figure 1 (TIAB and DONALDSON, 2015).

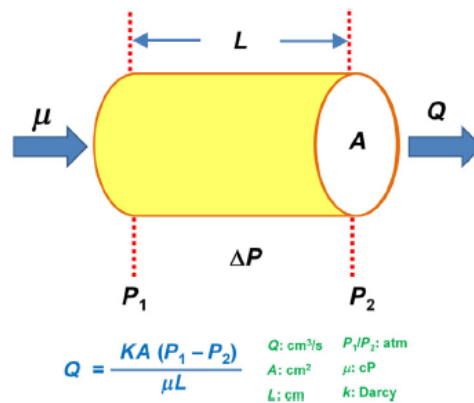


Figure 1. Diagram explaining parameters in the Darcy equation for incompressible liquid (MCPHEE *et al.*, 2015).

Qualitatively, reservoir absolute permeability values can be graded in the following manner (NORTH, 1985 *apud* AHR, 2011):

Qualitative Description	Absolute permeability (mD)
Poor to fair	< 1.0 – 15
Moderate	15 – 50
Good	50 – 250
Very good	250 – 1000
Excellent	> 1000

### 2.1.1.3. Saturation

Saturation ( $S$ ) is defined as the ratio of the pore volume occupied by a fluid, normally water ( $V_w$ ), oil ( $V_o$ ), or gas ( $V_g$ ), to the total pore volume of the reservoir rock ( $V_p$ ) such that (AHR, 2011)

$$S_w = \frac{V_w}{V_p}, \quad S_o = \frac{V_o}{V_p}, \quad S_g = \frac{V_g}{V_p} \quad \text{and} \quad S_w + S_o + S_g = 100 \quad (5).$$

In conventional literature, water in reservoir rocks is described as *connate water*, or *interstitial water* remaining from the time of deposition. For oil or gas to enter the reservoir,

it must displace the interstitial water. If the pore volume is sufficiently large, the oil will displace water and reside in the pore centers (Figure 2), but it cannot displace water from small pores or from coatings on grain surfaces. That unmovable water is the *wetting fluid* (AHR, 2011).

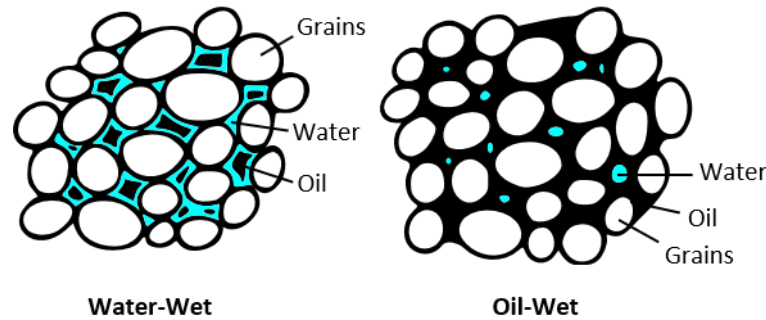


Figure 2. Idealized representation of water-wet and oil-wet reservoirs with depositional, interparticle porosity. All rocks had to be water-wet originally, but some became oil-wet after hydrocarbon migration, and surface chemical reactions between the hydrocarbons and the pore walls caused the rock to become oil-wet. This is especially true of carbonate reservoirs with oils containing polar organic compounds that react with carbonates (AHR, 2011).

### 2.1.2. Carbonate rocks

Carbonate rocks are those that contain more than 50% carbonate minerals. If the carbonate mineral is calcite ( $\text{CaCO}_3$ ) or aragonite (polymorph of calcite), the rock is called limestone; if it is dolomite ( $\text{CaMg}_2\text{CO}_3$ ), then it is called dolostone (BELL, 2005).

The composition of carbonate rocks usually refers to constituent grain type rather than mineral content, for being a better indicator of depositional environment. Carbonate grains are classified as skeletal and nonskeletal. Skeletal constituents include whole and fragmented remains of calcareous plants and animals such as mollusks, corals, calcified algae, brachiopods, arthropods, and echinoderms, among many others. Nonskeletal grains include ooids, pisoids, peloids, and clasts (AHR, 2011).

There are many classification schemes for carbonate rocks, including the popular, modern classifications for detrital carbonates developed by Folk (1959, 1962) (Figure 3) and Dunham (1962) (Figure 4); classifications for reef rocks developed by Embry and Klovan (1971) (Figure 5) and Riding (2002) (Figure 6); a scheme to include depositional, diagenetic, and biological aspects of carbonates in one classification system proposed by Wright (1992), and a more recent microbialite classification by Riding (2011) based on Aitken (1967) (AHR,



2011; GALLOIS, 2016).

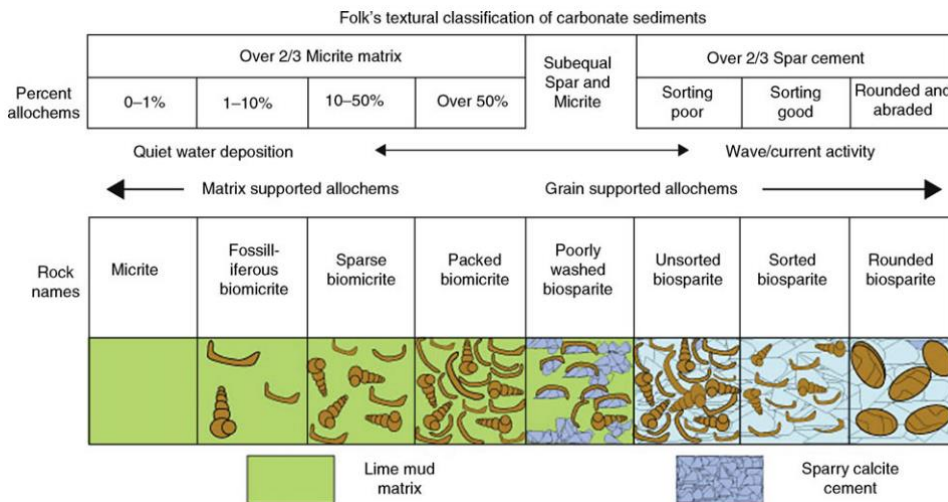


Figure 3. Folk's (1962) textural spectrum for carbonate sediments records 8 phases of sorting and rounding with the intent of capturing the deposition settings from low energy (left) to high energy (right). In very low-energy settings, micrites or mud-sized carbonate accumulate; in intermediate-energy settings, micrites with greater concentrations of allochemical particles, winnowed grain, and mud accumulations result; in high-energy settings, sorting and rounding of grains winnow most of the micrite matrix away. Textural inversions are the result of storm events that mix sediments from different settings or introduce short-lived conditions into a normally low-energy setting (KENDALL *et al.*, 2011).

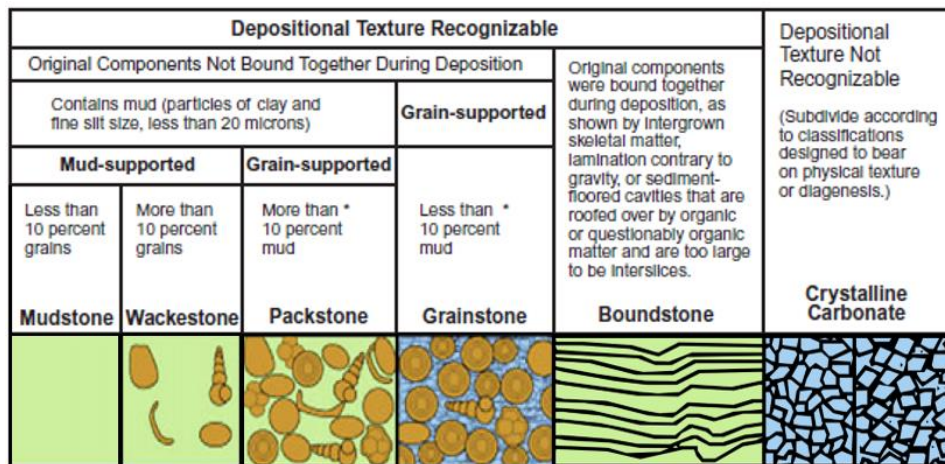


Figure 4. R. J. Dunham's 1962 classification of carbonate rocks is intended to convey information related to their depositional setting. Carbonates that are supported by matrix (mud) or framework (grains) form the basis of this classification. The end members include noncrystalline limestones often characterized by referencing the major component grains (DUNHAM, 1962 *apud* AHR, 2011; KENDALL *et al.*, 2011).

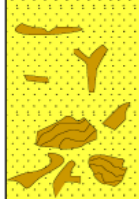

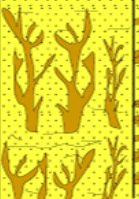
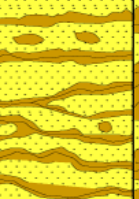

Allochthonous		Autochthonous		
Original components not bound organically at deposition		Original components bound organically at deposition		
>10% grains >2mm				
Matrix supported	Supported by >2mm component	By organisms that act as baffles	By organisms that encrust and bind	By organisms that build a rigid framework
Floatstone	Rudstone	Bafflestone	Bindstone	Framestone
				

Figure 5. Embry and Klovan (1971) modification of the Dunham’s (1962) biologic classification of organically bound rocks. “Floatstone” replaces Dunham’s “packstone”; the term “rudstone” replaces grain-supported biogenic limestones, and other organically bound rock are termed “bafflestone,” “bindstone,” or “framestone,” depending on the character of the organic structures. These latter terms are often used to describe the fabric of reefs, bioherms, and other biogenic carbonates (KENDALL *et al.*, 2011).

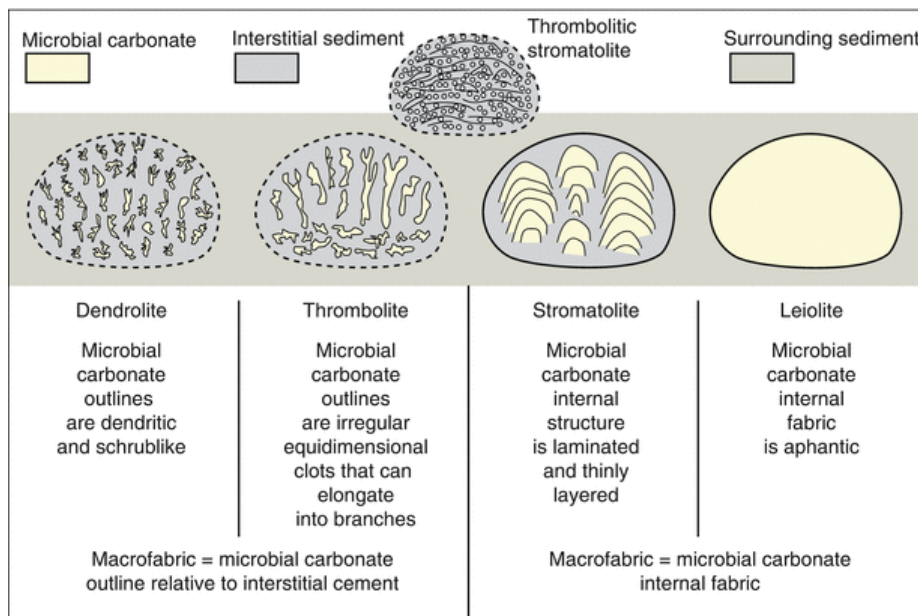
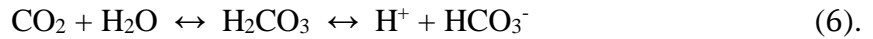


Figure 6. Microbial carbonates defined by macrofabric: leiolite (aphanitic), stromatolite (laminated), thrombolite (clotted), dendrolite (dendritic). Examples show domes and associated sediment. Not to scale. All categories are integrational. In addition to domes/mounds, overall shape can include columns, layers, and irregular masses. A complication is that leiolite and stromatolite macrofabrics are defined by features within



### 2.1.3. CO<sub>2</sub> chemical properties

When CO<sub>2</sub> dissolves in water, it forms carbonic acid (H<sub>2</sub>CO<sub>3</sub>) and decomposes into a hydrogen ion (H<sup>+</sup>) and bicarbonate ion (HCO<sub>3</sub><sup>-</sup>) following the equation:



Its solubility increases with increasing pressure, decreases with temperature, and diminishes as the salinity increases (IPCC, 2005), as seen in Figure 8. The following empirical relation (ENICK and KLARA, 1990) can be used to estimate CO<sub>2</sub> solubility in brackish water and brine:

$$w_{\text{CO}_2, b} = w_{\text{CO}_2, w} \cdot (1.0 - 4.893414 \cdot 10^{-2} \cdot S + 0.1302838 \cdot 10^{-2} \cdot S^2 - 0.1871199 \cdot 10^{-4} \cdot S^3) \quad (7).$$

where  $w_{\text{CO}_2}$  is CO<sub>2</sub> solubility,  $S$  is water salinity (expressed as total dissolved solids in % by weight) and the subscripts  $w$  and  $b$  stand for pure water and brine, respectively.

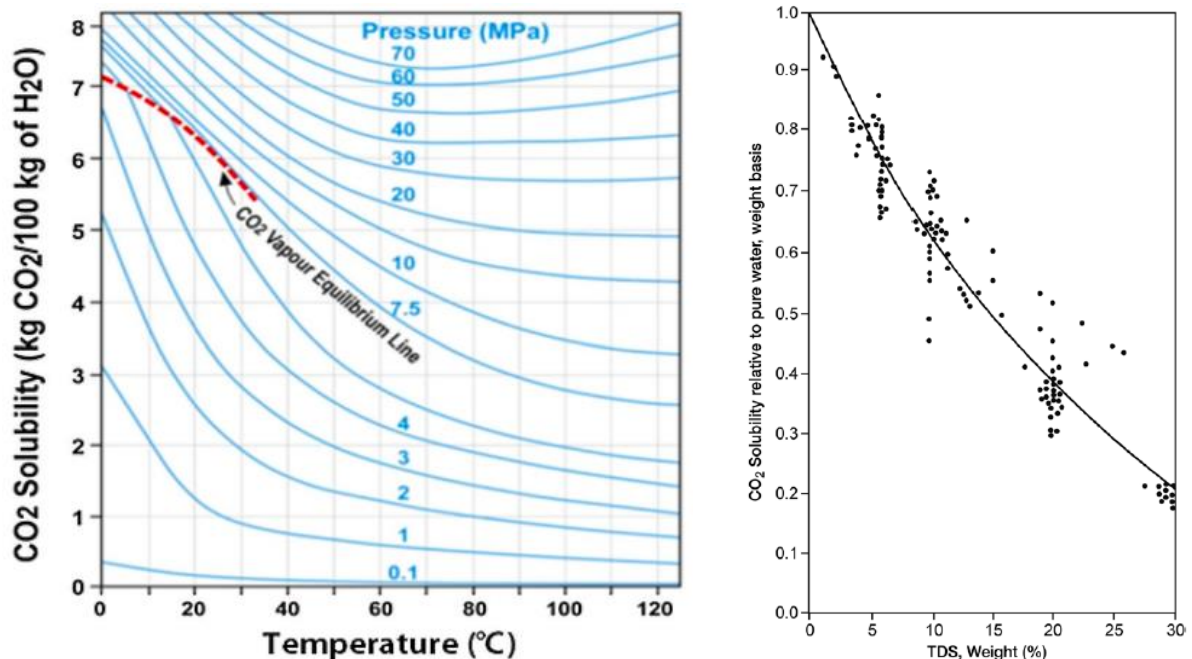


Figure 8. Left: CO<sub>2</sub> solubility in water (PERKINS, 2003); Right: CO<sub>2</sub> solubility in brine relative to that in pure water, showing experimental points reported by ENICK and KLARA (1990) and correlation developed by IPCC (2005) (TDS stands for total dissolved solids).

Under normal atmospheric conditions, CO<sub>2</sub> is a thermodynamically stable gas, about 1.5 times denser than air. However, at temperatures greater than 31,1°C (or 87,7°F) and pressures

greater than 73,8 bar (or 1070,4 psi) – the critical point -, CO<sub>2</sub> is in the supercritical phase (Figure 9), where it behaves as a condensed gas having low viscosity and high density (BACHU, 2000).

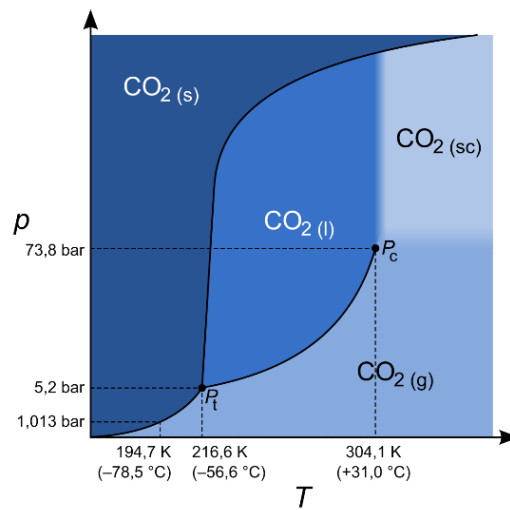


Figure 9. Carbon dioxide phase diagram ([Wikipedia](#)).

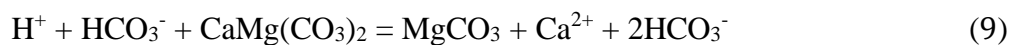
### 2.1.3.1. Carbonate Rocks Dissolution

The main factors influencing the interaction between solid and liquid are temperature, pressure, pH, fluid/solid ratio, mineral surface structure, and reaction surface area, among other factors (He *et al.*, 2017).

In the presence of water, CO<sub>2</sub> reacts according to equation (9). In carbonates, H<sup>+</sup> and HCO<sub>3</sub><sup>-</sup> react with calcite (CaCO<sub>3</sub>) according to



and with dolomite (CaMg(CO<sub>3</sub>)<sub>2</sub> or MgCO<sub>3</sub>) according to (Zhang *et al.*, 2007)



It is worth reminding that calcite dissolution and precipitation in the presence of CO<sub>2</sub> change with temperature, pressure, and pH conditions, and its solubility depends on the incubation period of contact (BAHAR and LIU, 2008). How some of these conditions affect calcite and dolomite dissolution is indicated in Figure 10 graphs.

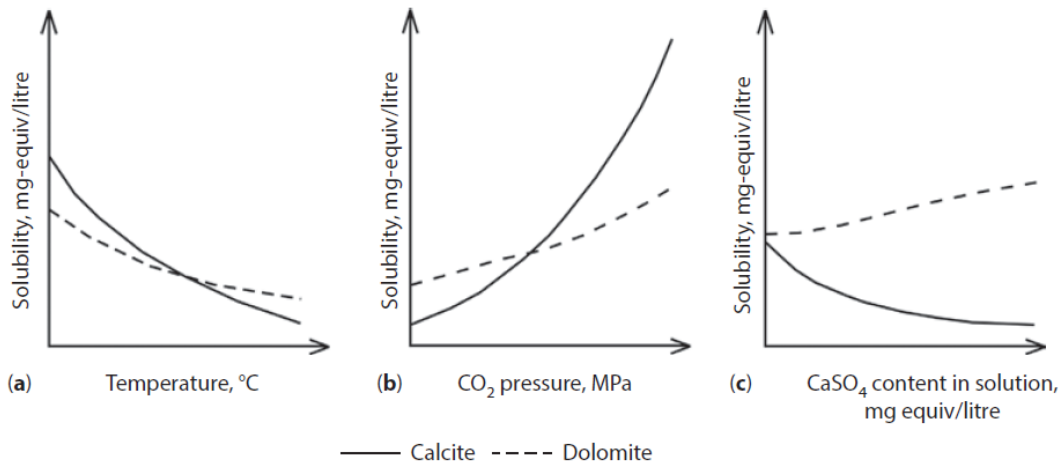


Figure 10. Conceptual scheme of calcite and dolomite solubility changes as affected by various factors. (a) Temperature effect, °C (at CO<sub>2</sub> pressure of 0.1 MPa), (b) CO<sub>2</sub> content effect (at temperature 25°C), and (c) Effect of CaSO<sub>4</sub> content in solution, at CO<sub>2</sub> pressure of 0.00012 MPa and temperature 25°C (after SOKOLOV, 1965 *apud* BAGRINTSEVA, 2015).

Various investigations have examined the effects of different factors, such as temperature, pressure, and salinity level, on CO<sub>2</sub> solubility reactions (Sun *et al.*, 2016). These experimental and modeling results show that CO<sub>2</sub> solubility increases with elevated pressure and decreases with increasing temperature and salinity, which allows for a direct link between the observations in the laboratory and the physics of the multiphase displacement process (DE SILVA *et al.*, 2015 *apud* SUN *et al.*, 2016).

#### 2.1.4. Carbon Capture and Storage (CCS)

To be effective in fighting climate change, we need to keep the CO<sub>2</sub> out of the atmosphere for thousands of years or more; the most promising option today is injecting the CO<sub>2</sub> deep into the Earth in porous geologic formations (HERZOG, 2018).

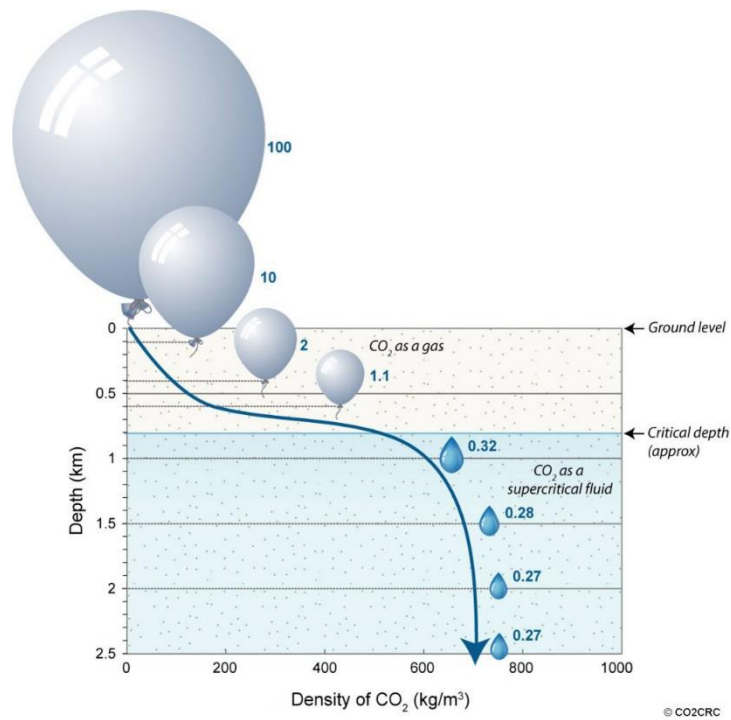


Figure 11. Graphic depiction of CO<sub>2</sub> density changes with depth.

Source: [CO<sub>2</sub> CRC](#).

To do that, CO<sub>2</sub> needs to be captured before or after being launched into the atmosphere and transported to the injection site, where it will be injected into the storage formation. A good geologic storage formation for CO<sub>2</sub> must be porous with good permeability, must be below 800 m depth to ensure that the CO<sub>2</sub> remains in a supercritical phase (Figure 11), must have an impermeable caprock to prevent gas leakage and it is desirable to be thick and continuous over large areas to be able to store large volumes of CO<sub>2</sub> (HERZOG, 2018). The geological formations that meet the above criteria are oil and gas reservoirs, or deep saline formations (Figure 12).

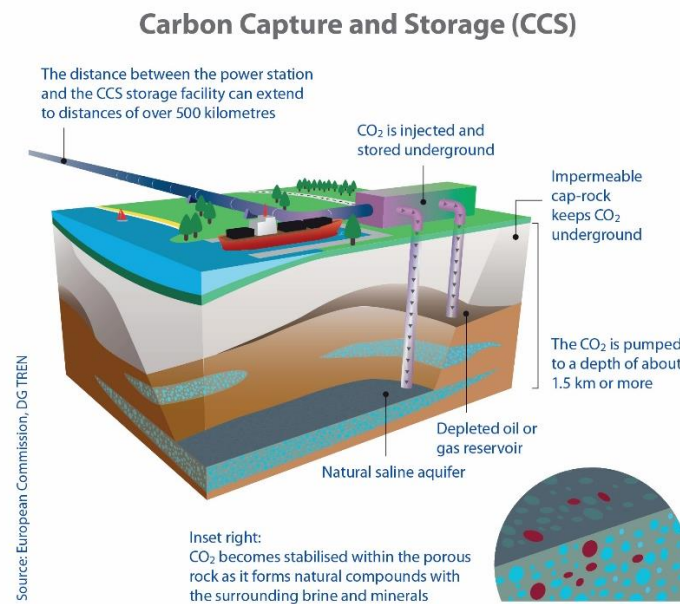


Figure 12. Summary of the carbon capture and storage process (<https://ec.europa.eu/jrc/en/research-topic/carbon-capture-utilisation-and-storage>).

Once the CO<sub>2</sub> enters the formation, several factors determine its behavior. The better we can characterize a formation in terms of its structure, dimensions, and physical properties, the better we can model how the CO<sub>2</sub> will move through the formation and what will happen to the plume over time (HERZOG, 2018).

Four main mechanisms, working together, trap the CO<sub>2</sub> in the formation: structural trapping, capillary trapping, solubility trapping, and mineral trapping: Structural trapping refers to the CO<sub>2</sub> being beneath the formation's impermeable caprock as the gas plume rises; Capillary trapping refers to the CO<sub>2</sub> being immobilized in the pore space as the plume moves through the formation; Solubility trapping refers to the dissolution of CO<sub>2</sub> into the formation water; and Mineral trapping refers to the reaction of formation minerals with dissolved CO<sub>2</sub> to incorporate the CO<sub>2</sub> into new minerals, most commonly calcite (HERZOG, 2018) (Figure 13). The trapping mechanisms create storage security.



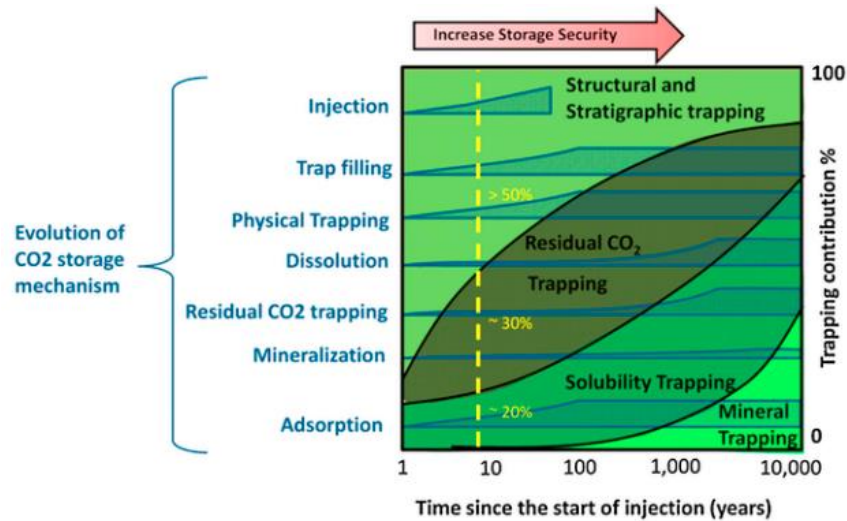


Figure 13. Evolution of CO<sub>2</sub> storage mechanisms through time. The horizontal axis shows the time since the start of injection; the right vertical axis shows the trapping contribution percentage of the four main storage mechanisms; the left vertical axis shows the qualitative evolution of CO<sub>2</sub> storage mechanisms. The dashed line represents the simulation time of this study and percentage contribution of the CO<sub>2</sub> storage mechanisms. Modified from IPCC (2005) (Veloso *et al.*, 2016).

### 2.1.5. Enhanced Oil Recovery

Oil recovery operations traditionally have been subdivided into three stages: primary, secondary, and tertiary. *Primary production* resulted from the displacement energy naturally existing in a reservoir such as solution gas drive, gas-cap drive, natural waterdrive, fluid and rock expansion, and gravity drainage. *Secondary recovery* usually was implemented after primary production declined, including processes as waterflooding (most used nowadays) and gas injection for gas-cap expansion, pressure maintenance or into oil-column wells to displace oil immiscibly. *Tertiary recovery* (also known as **enhanced oil recovery** or **EOR**) uses miscible gases (as carbon dioxide, nitrogen, and flue gases), chemicals (as polymers, surfactants, and hydrocarbon solvents), and/or thermal energy (use of steam, hot water, or oil combustion in the reservoir rock) to displace additional oil after the secondary recovery process became uneconomical (GREEN and WILLHITE, 2018).

Using EOR, 30% to 60% or more of the original oil-in-place (OOIP) from the reservoir can be extracted, compared to 20% to 40% using primary and secondary recovery ([U.S. Department of Energy](#)).

### 2.1.5.1. CO<sub>2</sub> EOR

EOR processes can be classified into five categories: mobility-control, chemical, miscible, thermal, and other processes, such as microbial EOR (GREEN and WILLHITE, 2018). Injection of CO<sub>2</sub> is a type of miscible process, in which the objective is to inject fluids that are directly miscible with the oil or that generate miscibility in the reservoir through composition alteration (GREEN and WILLHITE, 2018).

The CO<sub>2</sub> miscible process is illustrated in Figure 14. A volume of relatively pure CO<sub>2</sub> is injected to mobilize and displace residual oil. Through multiple contacts between the CO<sub>2</sub> and oil phase, intermediate- and higher-molecular-weight hydrocarbons are extracted into the CO<sub>2</sub>-rich phase. Under proper conditions, this CO<sub>2</sub>-rich phase will reach a composition that is miscible with the original reservoir oil. From that point, miscible or near-miscible conditions exist at the displacing front interface. CO<sub>2</sub> volumes injected during a process are typically approximately 25% PV (pore volume) (GREEN and WILLHITE, 2018).

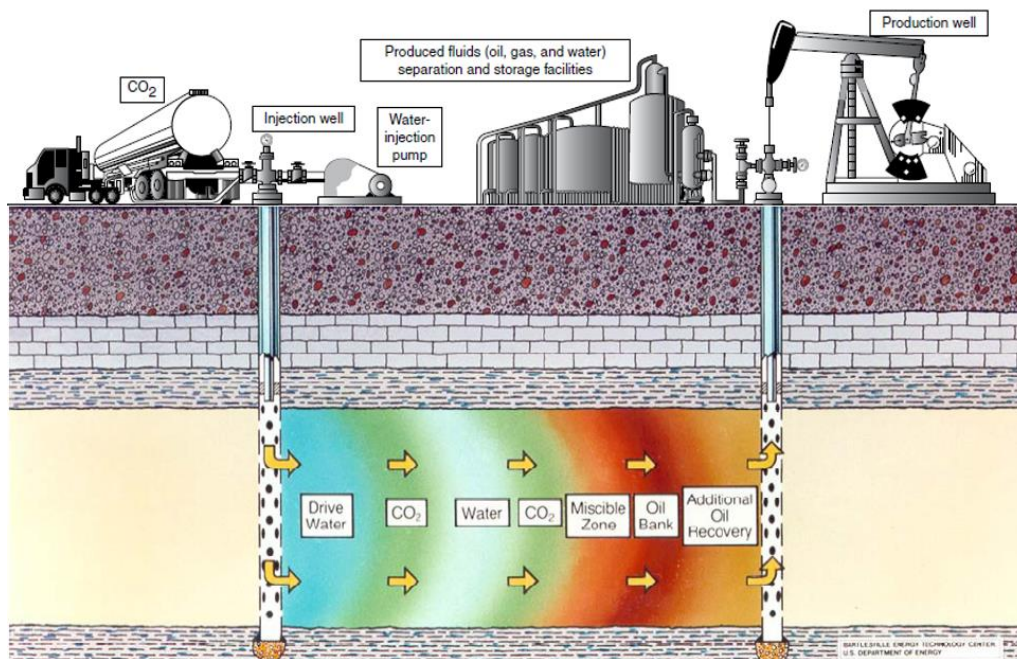


Figure 14. CO<sub>2</sub> miscible process (GREEN and WILLHITE, 2018; DOE/NTL, 2010 *apud* PIZARRO and BRANCO, 2012).

In the supercritical phase, CO<sub>2</sub> displaces oil and water under unfavorable-mobility-ratio conditions in most cases, which leads to fingering of the CO<sub>2</sub> through the oil phase (Figure 15) and to poor macroscopic displacement efficiency (GREEN and WILLHITE, 2018).



Figure 15. Snapshot of the concentration field during the unstable displacement of a more viscous fluid (dark) by a fully-miscible, less viscous fluid (light) (<http://news.mit.edu/2011/fluid-mixing-0519>).

To overcome this difficulty can be used the water-alternating-gas (WAG) method (Figure 14). The water injection alternated with gas injection reduces the oil's relative permeability to CO<sub>2</sub> and thereby reduces the gas mobility. Another advantage of the WAG process is that it spreads the demand for CO<sub>2</sub> over time. Other methods of mobility control are being tested, which include the use of foams and polymers in conjunction with CO<sub>2</sub> injection (GREEN and WILLHITE, 2018).

### 2.1.6. Carbonated Water Injection (CWI)

Conventional CO<sub>2</sub> flooding normally requires large quantities of CO<sub>2</sub>, increasing the cost of capture and storage of gas close to the oil fields (SOHRABI *et al.*, 2012), and injecting CO<sub>2</sub> alone is found to cause early breakthrough of CO<sub>2</sub> (FIGUERA *et al.*, 2014).

An alternative injection strategy that requires much less CO<sub>2</sub> is carbonated water injection (CWI), being particularly attractive for offshore reservoirs or reservoirs far away from inexpensive natural CO<sub>2</sub> resources. In CWI, CO<sub>2</sub> and water coexist in the same phase, causing a more evenly gas distribution within the reservoir, thus retarding CO<sub>2</sub> breakthrough and improving sweep efficiency (BISWESWAR *et al.*, 2020).

For CO<sub>2</sub> storage, CWI eliminates the risk of buoyancy-driven leakage as in the case of bulk phase injection (BURTON and BRYANT, 2007 *apud* SOHRABI *et al.*, 2012) since carbonated water is denser than the native brine (HEBACH *et al.* 2004 *apud* SOHRABI *et al.*, 2012), thus securing storage and reducing the cost of monitoring the stored CO<sub>2</sub>, being a safer and better method of CCS compared to direct injection of CO<sub>2</sub> (ANCHLIYA *et al.* 2012 *apud* BISWESWAR *et al.*, 2020).

An examination of CO<sub>2</sub> injection in carbonate aquifers demonstrated that either a permeability improvement or reduction can be obtained since the trend of change in rock properties is case-dependent because it is related to the distribution of pores, brine composition, and thermodynamic interactions (IZGEC *et al.*, 2006 *apud* MOHAMED *et al.*, 2010). The precipitation process of dissolved material can significantly impact the permeability of the formations, while only a small change in primary porosity is observed (GRIGG and SVEC, 2003 *apud* MOHAMED *et al.*, 2010). Permeability and porosity alteration showed similar trends at different temperatures (IZGEC *et al.*, 2006 *apud* MOHAMED *et al.*, 2010). High flow rates give longer wormholes into the porous media, while low flow rates lead to compact/localized dissolution (EGERMANN *et al.*, 2005 *apud* MOHAMED *et al.*, 2010). In addition, during CWI, the region closest to the injection has higher pressure and it decreases the further away from the injection point, leading to calcite precipitation, possibly causing impacts on the rock's hydraulic properties (SEYYEDI *et al.*, 2020).

In general, increasing pressure increases CO<sub>2</sub> solubility and reduces pH, resulting in higher rock dissolution potential and increases the permeability improvement while increasing salinity; increasing the temperature decreases CO<sub>2</sub> solubility and elevates pH resulting in reduced rock dissolution potential and lowering permeability improvement potential (KARAEI *et al.*, 2019; METZ *et al.*, 2005).

In the present dissertation, the authors undertook experiments on carbonates with very low and very high permeabilities, including an examination of vuggy carbonates. To the best of the authors' knowledge, very few studies have been conducted on CCS in carbonate reservoirs with very low and very high permeabilities. Some of those are summarized as follows.

SMITH *et al.* (2013) conducted experiments injecting CO<sub>2</sub>/brine mixtures into carbonates from the Weyburn–Midale field (Canada) with permeabilities below 2 mD at reservoir conditions (60°C and 24.8 MPa). More homogeneous samples sustained steady-state carbonate mass transfer, resulting in uniformly advancing dissolution fronts and little variation in overall permeabilities, while more heterogeneous samples presented variable fluid velocities, causing more variable mass transfer rates – preferential calcite dissolution in high permeability streaks –, the formation of unstable dissolution fronts and “dramatic permeability increases of several orders of magnitude”.

KOVACS *et al.* (2015) studied CO<sub>2</sub> sequestration on low permeability carbonates at Hontomín (Spain) through laboratory experiments and numerical reservoir simulation. In the

two extreme cases (infinitely fast transport or kinetics), dissolution was homogeneous. However, for a broad range of conditions, dissolution tends to form wormholes.

KARAEI *et al.* (2019) injected CO<sub>2</sub>/brine mixtures into carbonates from the Gadvan reservoir, (Iran) with permeabilities of approximately 5 mD; this was done under varying conditions: temperatures range (27-100°C), injection pressure range (1-7 MPa), confining pressure range (5-15 MPa) and injected brine compositions (formation brine, seawater, and freshwater). Rock dissolution increased with pressure and decreased with temperature and salinity as expected. Permeability was increased with increasing CO<sub>2</sub> pressure regardless of the types of brine used and was reduced by increasing confining pressure (due to relative stress compression of pore throats) and by increasing temperature (reducing the solubility of calcium carbonate), especially for freshwater (which has a lower initial buffering capacity).

In the case of vuggy carbonates, KHAN *et al.* (2019) performed fluid injection and simulations in synthetic homogeneous and vuggy plugs and identified, in the vuggy ones, a greater deposition of particles in the matrix around the vug, interpreting that the permeability variation generated by the vug would induce increased turbulence in the fluid streamlines, causing the precipitated and suspended scale particles – that have a different momentum than the fluid – to deposit, locally reducing the rock primary porosity and permeability, inducing hydraulic impairment.

### 2.1.7. Formation damage

According to CIVAN (2015), formation damage is “a generic terminology referring to the impairment of petroleum-bearing formations permeability by various adverse processes” that “may be caused by many factors, including physicochemical, chemical, biological, hydrodynamic, and thermal interactions of porous formation, particles, and fluids, and the mechanical deformation of formation under stress and fluid shear”.

Commonly, the mineral matter and fine particles loosely attached to the pore surface are at equilibrium with the pore fluids; however, when this equilibrium condition is disturbed during reservoir production by primary and enhanced recovery processes, mineral matter can dissolve and generate many different ions in the aqueous phase and fine particles are released from the pore surface into the fluid phases (CIVAN, 2015). Once these ions and particles are introduced into the fluid phases, they become mobile, and may interact freely with each other in many intricate ways to create severe reservoir formation damage problems, which are often not reversible, and include permeability impairment, skin damage, and decreased well

performance (CIVAN, 2015).

To avoid this, properly designed experimental and analytical techniques, and the modeling and simulation approaches can be used to help us understand diagnosis, evaluation, prevention, remediation, and controlling of formation damage in oil and gas reservoirs (CIVAN, 2015). The laboratory experiments are important steps in reaching this understanding of the formation damage phenomena physical mechanisms because, from this experimental basis, realistic models which allow extrapolation outside the scalable range may be constructed (ENERGY HIGHLIGHTS, 1990 *apud* CIVAN, 2015). These efforts are needed to develop and verify accurate mathematical models and computer simulators that can be used to predict and determine strategies to prevent and/or mitigate formation damage in oil reservoirs (CIVAN, 1994 *apud* CIVAN, 2015).

## 2.2. Equipment

### 2.2.1. Core analysis

The laboratory core analysis can be distinguished between Routine Core Analysis (RCAL) and Special Core Analysis (SCAL), according to Figure 16. RCAL aims to measure basic core properties such as porosity, permeability, grain density, fluid saturation, and heterogeneity (with computed tomography - CT), as well as keep a visual recording of the cores and obtain data to correlate cores with logs in depth (ANDERSEN *et al.*, 2013 *apud* SCHÖN, 2015).

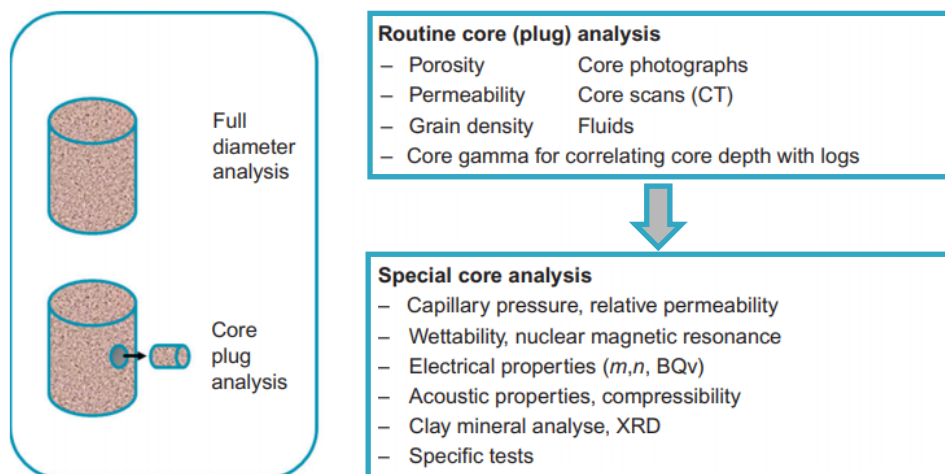


Figure 16. Overview of core analysis directed on reservoir properties (SCHÖN, 2015).

SCAL aims to obtain a detailed understanding of a reservoir by additional measurements

such as (ANDERSEN *et al.*, 2013 *apud* SCHÖN, 2015):

- electrical measurements to obtain Archie exponents for calibrating electrical logging measurements of porosity and saturation,
- nuclear magnetic resonance (NMR) core measurements determine a formation-specific cutoff value for the relaxation time from an NMR log,
- capillary pressure measurements by mercury injection, centrifuge, or porous plate methods indicate distributions of pore throats and are used to evaluate saturation distribution as a function of height in a formation,
- relative permeability determines the multiphase flow character of the formation, and can be performed at ambient or elevated conditions of pressure and temperature,
- wettability is determined by Amott-Harvey or United States Bureau of Mines (USBM) methods.

#### 2.1.1.1. Routine Core Analysis (RCAL)

Below, the routine core analyses relevant to this research will be briefly explained: grain density, porosity, and permeability measurements, and analysis by X-Ray Computed Microtomography (micro-CT or  $\mu$ -CT).

##### 2.1.1.1.1. Grain density and porosity measurements

Core samples provide an accurate and repeatable measurement of porosity (CANNON, 2015). After cleaning, the core sample is weighed and measured to calculate the bulk volume and grain density and then inserted into a helium (or nitrogen) porosimeter. According to Boyle's law (which states that for an ideal gas assuming constant temperature, the product of pressure and volume in a closed system remains constant, or  $P_1V_1 = P_2V_2$ ), the porosimeter measures the connected porosity of the sample – or, at least, as much of the pore space that the expanding helium gas can occupy (CANNON, 2015; MCPHEE *et al.*, 2015). Provided care is taken and the method is accurate and reproducible (CANNON, 2015; MCPHEE *et al.*, 2015).

##### 2.1.1.1.2. Permeability measurement

A schematic of the principle involved in permeability measurements is shown in Figure 17.

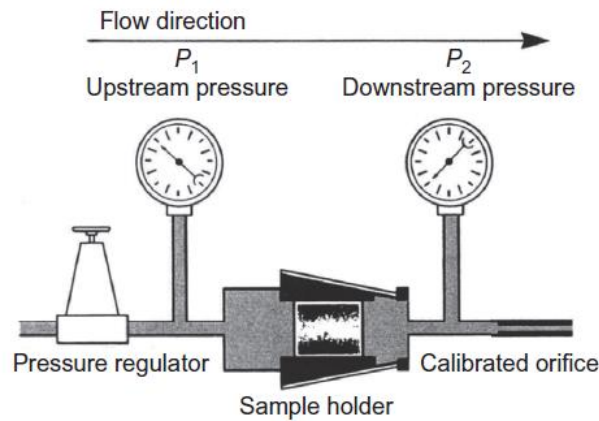


Figure 17. Schematic flow diagram of permeameter (TIAB E DONALDSON, 2015).

A clean dry plug is placed in a holder. Upstream and downstream pressures are measured to determine the differential pressure across the core. Flow rate, in  $\text{cm}^3/\text{s}$ , is measured at atmospheric pressure. This steady-state method is acceptable for high permeability rocks, as in low permeability samples this method may take several hours, being preferable to use unsteady-state methods in these cases, as they allow determination of  $k$  to be made in minutes.

Dry gas has been selected as the standard fluid for use in permeability determination because it minimizes fluid-rock reaction and is easy to use. Equation (5) is valid for non-compressible or slightly compressible fluids (liquid). For compressible fluids (gas)  $k$  is obtained from

$$k = \frac{2 q \mu_g L}{(P_1^2 - P_2^2) A} \quad (11)$$

where  $\mu_g$  is the gas viscosity in cP.

Air permeability measured in a routine core analysis laboratory on a (nonfractured) core sample will give higher values than the actual reservoir permeability, especially with a liquid as the flowing fluid. The difference is due to the gas slippage (or Klinkenberg) effect and overburden pressure effects.

The Klinkenberg-corrected gas permeability can be obtained through the equation

$$K_a = K_\infty \left( 1 + \frac{b_k}{\bar{p}} \right) \quad (12).$$

where

$K_a$  = apparent gas permeability observed at the mean pressure,

$K_\infty$  = Klinkenberg permeability,

$b_k$  = slip factor,

$\bar{p}$  = average pressure at the inlet and outlet of the plug.



2.1.1.1.3. X-Ray Computed Microtomography (micro-CT or  $\mu$ -CT)

X-ray computed microtomography is a nondestructive technique that allows visualization of the internal structure of objects, determined mainly by variations in density and atomic composition (MEES *et al.*, 2003). Micro-CT can create cross-sectional images from different angles of an object by making use of X-rays which, after being processed by the software, generates a three-dimensional model of the scanned object (ORHAN, 2020).

In this technique, the sample to be imaged is positioned between an X-ray source and a detector and rotated while X-ray beams from the source cross the object and cast an X-ray shadow onto the radiographic image detector (Figure 18a), namely, a negative image of the object (Figure 18b). The beams are variously absorbed and attenuated in the different parts of the object depending on its density – in general, denser parts will absorb more energy – generating an image with full-scale signal where there is no attenuation (= void), while it is zero where the attenuation is complete (no X-rays passing through) (LEIDERMAN *et al.*, 2017; ORHAN, 2020).

The collection of the acquired radiograms produces a stack of 2D raw gray-scale horizontal image slices (Figure 18c) from which the 3D digital object can be reconstructed (Figure 18d). In  $\mu$ -CT, the dimensions of the reconstructed voxels (i.e. a volumetric pixel element) are in general in the micrometer range (LEIDERMAN *et al.*, 2017; ORHAN, 2020).

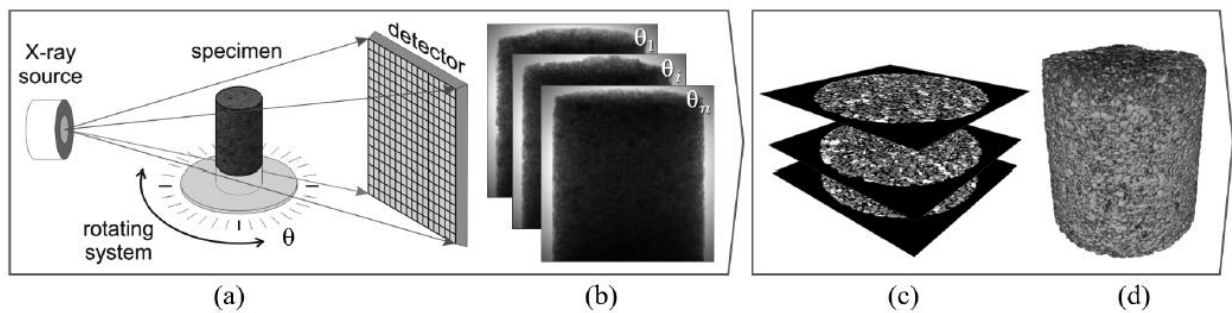


Figure 18. Illustrative scheme of CT acquisition workflow: (a) setup of  $\mu$ -CT scanner for image acquisition, (b) set of single radiographic projections, (c) stack of 2D raw gray-scale horizontal image slices, and (d) volume reconstructed (LEIDERMAN *et al.*, 2017; ORHAN, 2020).

After acquiring  $\mu$ CT images it is important to process them using one or more filters (e.g., anisotropic diffusion and/or non-local means filters) to correct and enhance the quality of the images (GODOY *et al.*, 2019). Subsequently to image treatment, a segmentation step is needed to isolate the pore system from the rock matrix, thus allowing their digital reconstruction. This segmentation can be done using different algorithms (automated methods) or by direct analysis using optical microscopy – thin sections impregnated with blue

epoxy resin help to identify pore spaces more accurately – or SEM (manual procedures), thus allowing one to separate between the pore spaces and the solid rock matrix (AL-RAOUSH and WILLSON, 2005; WILDENSCHILD *et al.*, 2002 *apud* GODOY *et al.*, 2019). The use of SEM as an auxiliary tool also guarantees the possibility of visualizing, with high resolution, regions that may become indistinct in  $\mu$ CT images generated with larger pixel sizes (BLUNT *et al.*, 2013; BULTREYS *et al.*, 2016 *apud* GODOY *et al.*, 2019).

### 2.1.1.2. Special Core Analysis (SCAL)

Below, the special core analyzes relevant to this research will be briefly explained: Nuclear Magnetic Resonance (RMN), X-ray Powder Diffraction (XRD), and Scanning Electron Microscopy with Energy Dispersive Spectroscopy (SEM/EDS).

#### 2.1.1.2.1. Nuclear Magnetic Resonance (NMR)

Nuclear Magnetic Resonance (NMR) refers to the response of atomic nuclei to magnetic fields. In the presence of an external magnetic field, an atomic nucleus precesses around the direction of the external field, producing measurable signals (COATES *et al.*, 1999).

NMR measurements can be made on any nucleus that has an odd number of protons or neutrons or both, such as the nucleus of hydrogen ( $^1\text{H}$ ), carbon ( $^{13}\text{C}$ ), and sodium ( $^{23}\text{Na}$ ), being that hydrogen is abundant in both water and hydrocarbons, has a relatively large magnetic moment, and produces a strong signal, being the focus of the application of NMR in petrophysics (COATES *et al.*, 1999).

Petrophysical information, such as **porosity**, **pore-size distribution**, **bound water**, and **permeability**, can be extracted from NMR relaxation measurements (COATES *et al.*, 1999).

##### 2.1.1.2.1.1. NMR Physics

First, the magnetic nuclei (or protons) are aligned with a static magnetic field  $\mathbf{B}_0$ , polarizing them. The polarization grows with a time constant, the **longitudinal relaxation time**, referred to as  $\mathbf{T}_1$ . Different fluids, such as water, oil, and gas, have very different  $\mathbf{T}_1$  relaxation times (Figure 19) (COATES *et al.*, 1999).

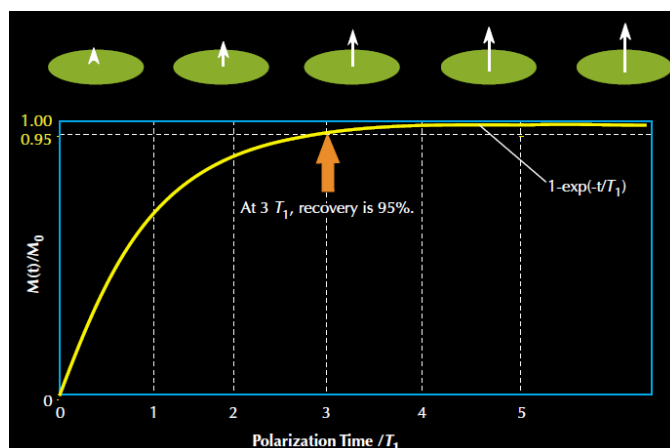


Figure 19.  $T_1$ -relaxation (polarization) curves indicate the degree of proton alignment, or magnetization, as a function of the time that a proton population is exposed to an external magnetic field.  $M(t)$  is the magnitude of magnetization at time  $t$  when the direction of  $B_0$  is taken along the  $z$ -axis and  $M_0$  = the final and maximum magnetization in a given magnetic field (COATES *et al.*, 1999).

After, the magnetization is tipped from the longitudinal direction to a transverse plane by applying an oscillating magnetic field  $B_1$  perpendicular to  $B_0$ , causing low-energy state protons to absorb energy and jump to the high-energy state and the protons to precess in phase with one another. This change in energy state and in-phase precession caused by  $B_1$  is called **nuclear magnetic resonance** (COATES *et al.*, 1999).

When the  $B_1$  field is turned off, the proton population begins to dephase, or lose phase coherency (the precessions of the protons will no longer be in phase with one another) and a receiver coil that measures magnetization in the transverse direction will detect a decaying signal. This decay is usually exponential, very short (a few tens of microseconds), and is called free induction decay (FID) (Figure 20) (COATES *et al.*, 1999).

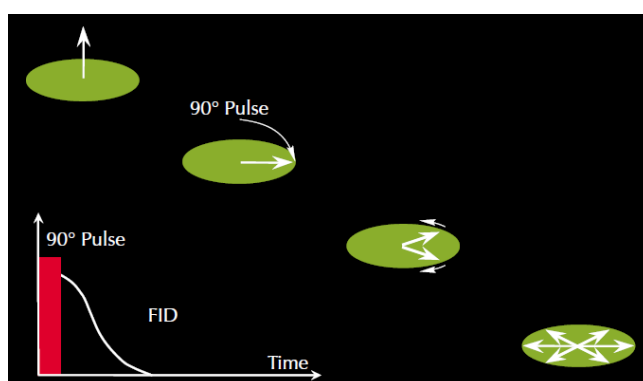


Figure 20. After the application of a  $90^\circ$  pulse, the proton population dephases, and a free induction decay (FID) signal can be detected (COATES *et al.*, 1999).

The dephasing can be reversed when a  $180^\circ$   $B_1$  pulse is applied, generating spin echos. Although a single spin echo decays very quickly,  $180^\circ$  pulses can be applied repeatedly to rephase the magnetization components and generate a series of spin echoes, that can be recorded. The entire pulse sequence – a  $90^\circ$  pulse followed by a long series of  $180^\circ$  pulses – is called a CPMG sequence (COATES *et al.*, 1999).

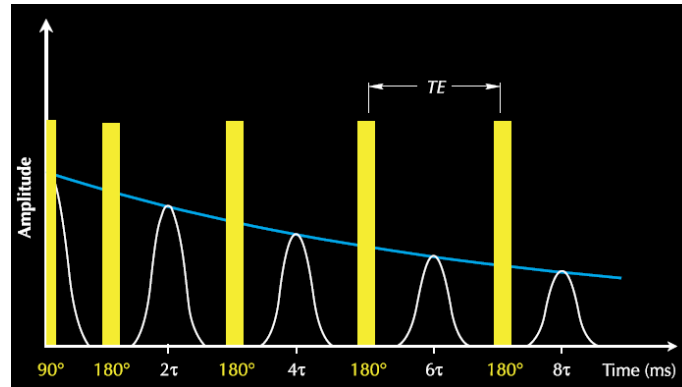


Figure 21. To generate a spin-echo train, the CPMG pulse sequence is used, which consists of a  $90^\circ$   $B_1$  pulse followed by a sequence of  $180^\circ$   $B_1$  pulses. Spin echoes of decreasing amplitude follow the  $180^\circ$   $B_1$  pulses (COATES *et al.*, 1999).

As shown in Figure 22, an NMR logging tool measures the amplitude of the spin echoes in the CPMG sequence to monitor the transverse magnetization decay and thus the irreversible dephasing. The time constant of the transverse magnetization decay is called the **transverse relaxation time**, referred as to  $T_2$ . The  $T_2$  decay from the formation contains most of the petrophysical information obtainable from NMR logging and therefore is the prime objective of NMR logging measurements (COATES *et al.*, 1999).

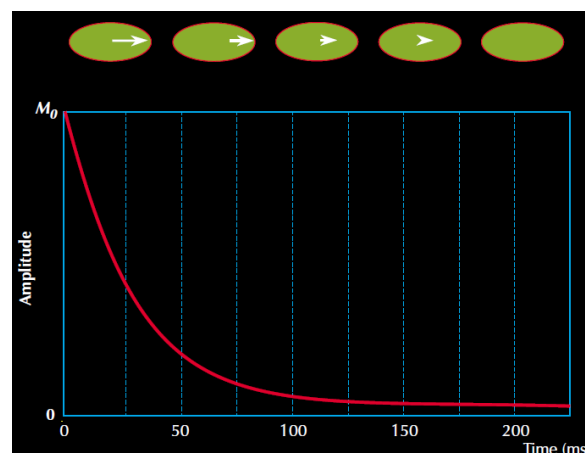


Figure 22. The amplitudes of the decaying spin echoes yield an exponentially decaying curve with time constant  $T_2$  (COATES *et al.*, 1999).

2.1.1.2.1.2. NMR in Petrophysics

To determine the  $T_2$  distribution that produces the observed magnetization is realized the **echo-fit** or **mapping**, a mathematical inversion process, using a multi-exponential model that assumes that the  $T_2$  distribution consists of  $m$  discrete relaxation times  $T_{2i}$  with corresponding porosity components  $\phi_i$  (Figure 23) (COATES *et al.*, 1999).

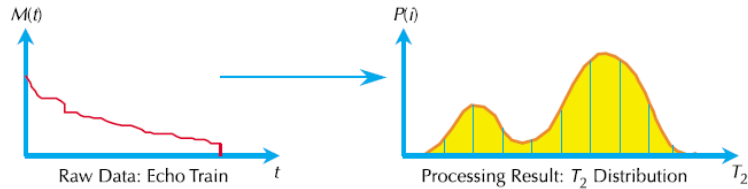


Figure 23. Through echo fitting, the echo train (echo amplitude as a function of time) is mapped to a  $T_2$  distribution (porosity as a function of  $T_2$ ) (COATES *et al.*, 1999).

For fluids in rock pores, three independent relaxation mechanisms are involved: (1) bulk fluid processes, which affect both  $T_1$  and  $T_2$  relaxation, (2) surface relaxation, which affects both  $T_1$  and  $T_2$  relaxation, and (3) diffusion in the presence of magnetic field gradients, which only affects  $T_2$  relaxation (COATES *et al.*, 1999).

The relative importance of the three relaxation mechanisms depends on the type of fluid in the pores (water, oil, or gas), the sizes of the pores, the strength of the surface relaxation, and the wettability of the rock surface. In general, for a water-wet rock, for **brine**,  $T_2$  is dominated by  $T_{2\text{surface}}$ ; for **heavy oil**,  $T_2$  has  $T_{2\text{bulk}}$  as its main contributor; for **intermediate-viscosity and light oil**,  $T_2$  is a combination of  $T_{2\text{bulk}}$  and  $T_{2\text{diffusion}}$  and is dependent on viscosity; for **gas**,  $T_2$  is dominated by  $T_{2\text{diffusion}}$  (COATES *et al.*, 1999).

Surface relaxation becomes dominant when a short inter-echo spacing is used and the formation is only brine-saturated. Under this condition,  $T_2$  is directly proportional to pore size (Figure 24) and the observed  $T_2$  distribution of all the pores in the rock represents the **pore-size distribution** of the rock (COATES *et al.*, 1999).

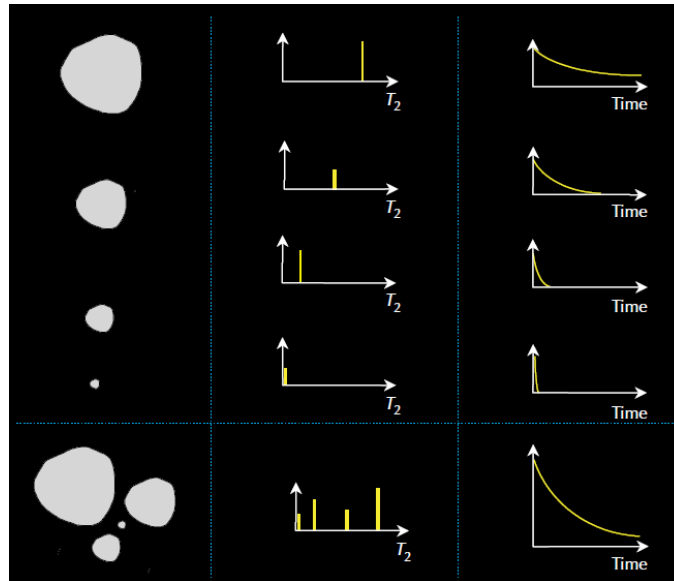


Figure 24. 100% water-saturated pore (upper left) has a single T<sub>2</sub> value (upper center) that depends on pore size, and thus its spin-echo train exhibits a single-exponential decay (upper right) that also depends on pore size. Multiple pores at 100% water saturation (bottom left) have multiple T<sub>2</sub> values (bottom center) that depend on the pore sizes, and thus their composite spin-echo train exhibits multi-exponential decay (bottom right) that also depends on the pore sizes (COATES *et al.*, 1999).

#### 2.1.1.2.2. X-ray Powder Diffraction (XRD)

X-ray powder diffraction is a non-destructive\* technique that provides a wide spectrum of tools for the study of solids, ranging from qualitative analysis to the study of internal defects in the atomic arrangement (GARCIA-GRANDA and MONTEJO-BERNARDO, 2013; LOUËR, 2017).

If an incident X-ray beam encounters a crystal lattice, general scattering occurs. Although most scattering interferes with itself and is eliminated (destructive interference), in a certain direction occurs diffraction maxima according to the Bragg relationship (POPPE *et al.*, 2001; GARCIA-GRANDA and MONTEJO-BERNARDO, 2013)

$$n\lambda = 2d \sin\theta \quad (13)$$

where:

$n = \text{integer}$ ,

$\lambda = \text{wavelength of the characteristics x-rays}$ ,

---

\* The term ‘non-destructive’, frequently applied to X-ray analysis, is not always appropriate here because crushing, grinding, or other manipulations are frequently required to prepare the sample for powder diffraction (GARCIA-GRANDA; MONTEJO-BERNARDO, 2013).

$d$  = lattice interplanar spacing of the crystal,  
 $\theta$  = X-ray incident angle (Bragg angle).

The basic geometry of an X-ray diffractometer involves a source of monochromatic radiation and an X-ray detector situated on the circumference of a graduated circle centered on the powder specimen (Figure 25). Divergent slits, located between the X-ray source and the specimen, and receiving slits, located between the specimen and the detector, limit scattered (non-diffracted) radiation, reduce background noise, and collimate the radiation. The detector and specimen holder are mechanically coupled with a goniometer so that a rotation of the detector through  $2x$  degrees occurs in conjunction with the rotation of the specimen through  $x$  degrees, a fixed 2:1 ratio (POPPE *et al.*, 2001).

A curved-crystal monochromator containing a graphite crystal is normally positioned in front of the detector to ensure that the detected radiation is monochromatic. The signals from the detector are filtered by pulse-height analysis, scaled to measurable proportions, and sent to a linear ratemeter for conversion into a continuous current. Common output devices include strip-chart recorders, printers, and computer monitors (POPPE *et al.*, 2001).

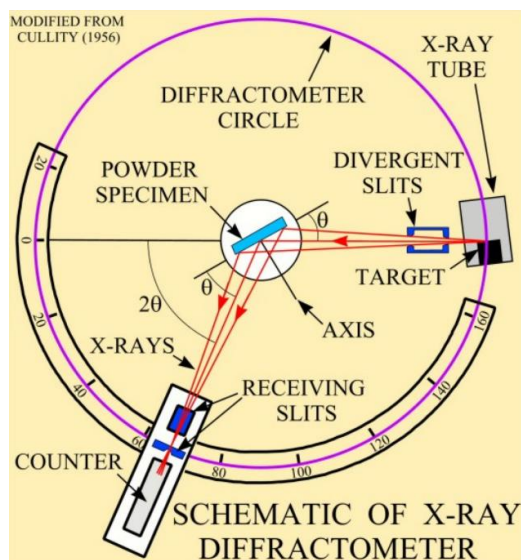


Figure 25. Schematic representation of the geometry of a conventional powder diffractometer (POPPE *et al.*, 2001).

The analysis is made in a randomly oriented powder mount to ensure that the incident X-rays have an equal chance of diffracting off any given crystal lattice face of the minerals in the sample. The mounts are typically X-rayed between the angles of 2 and 70 degrees two theta using copper K alpha radiation at a scanning rate of 2 degrees per minute (POPPE *et al.*, 2001).

Every crystalline powder produces a characteristic diffraction pattern. This is the basis of qualitative analysis by powder diffraction. Identification is usually accomplished by a systematic comparison of an unknown pattern with a catalog of standard data such as the Powder Diffraction File published by the International Centre for Diffraction Data (ICDD) (GARCIA-GRANDA and MONTEJO-BERNARDO, 2013).

Diffraction patterns of mixtures consist of the superimposed patterns of the individual components. Therefore, powder diffraction is useful in analyzing mixtures as well as pure materials. As the number of components increases, interpretation becomes more complicated because of the occurrence of peak superposition and success in interpretation depends on the amount of prior information available about the mixture (GARCIA-GRANDA and MONTEJO-BERNARDO, 2013).

As is true with all analytical procedures, X-ray powder diffraction is most powerful when used in conjunction with other techniques, such as emission spectroscopy, X-ray fluorescence spectroscopy, and chemical analysis. An important advantage of X-ray diffraction over these and other techniques is that the results obtained are in terms of the materials as they occur in the sample, not in terms of the elements or ions present. It is often the only satisfactory method of distinguishing among polymorphs or detecting a compound in the presence of others containing the same elements (GARCIA-GRANDA and MONTEJO-BERNARDO, 2013).

## 2.2. Geological Setting

---

### 2.2.1. Brazilian pre-salt

The production of oil and gas from the Brazilian pre-salt is expressive and of great importance, accounting for over 70% of the national production, as can be seen in the graph in Figure 26.



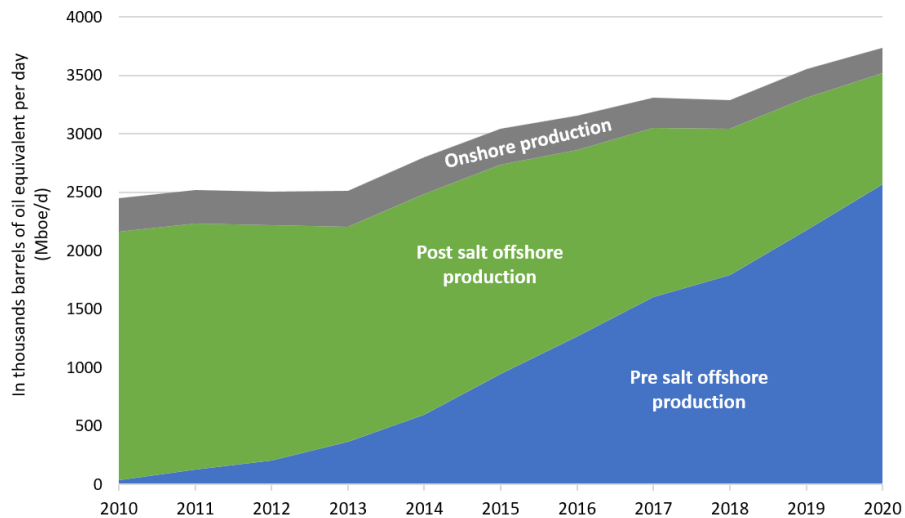


Figure 26. Evolution of onshore and offshore production - Pre-salt x Post-salt x Onshore in thousands of barrels of oil equivalent (Mboe/d).

Source: [ANP](#).

In the last 2019 bidding round alone, R\$ 73.2 billion was raised with signature bonuses (ANP, 2020), and collections of an additional R\$ 92.7 billion by 2028, considering only the Union's share in oil sales (O GLOBO, 2019).

The main producing basins are the Santos and Campos basins, accounting for 97% of oil production (Figure 27) and 83% of gas (Figure 28) production in the country.

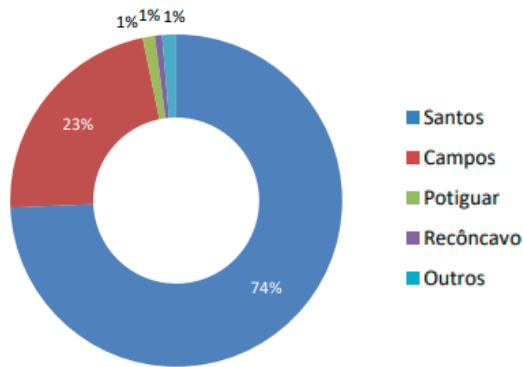


Figure 27. Distribution of oil production by basin. Source: March 2022 [ANP's Oil and Natural Gas Production Bulletin](#).

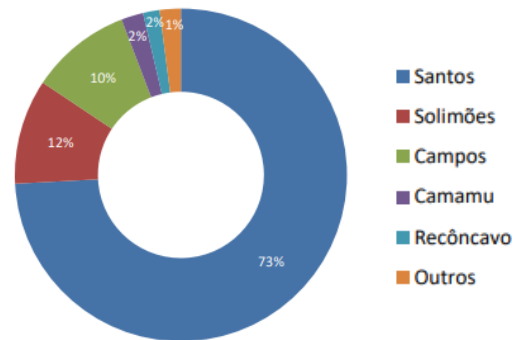


Figure 28. Distribution of natural gas production by basin. Source: March 2022 [ANP's Oil and Natural Gas Production Bulletin](#).

The southeastern Brazilian marginal basins originated from rifting of the Gondwana Continent during the Neocomian (lowermost Cretaceous), which eventually formed the South Atlantic Ocean through the separation of the American and African continents (LIMA and DE ROS, 2019). The Santos e Campos basins are aligned with the Kwanza, Benguela, and Namibe basins on the West African side (Figure 29).

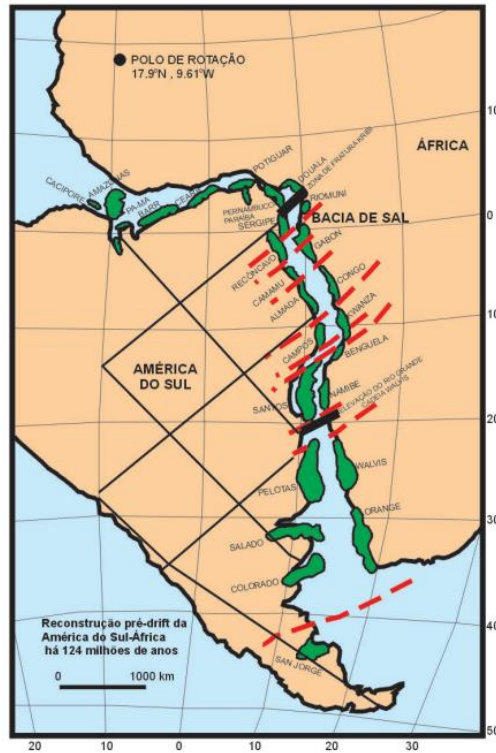


Figure 29. Tectonic reconstruction of sedimentary basins in the pre-drift configuration (124 million years ago) (MOHRIAK, 2003).

MILANI *et al.* (2007) divided the tectonostratigraphic evolution of the southeastern Brazilian marginal basins into the rift, post-rift, and drift supersequences (Figure 30).

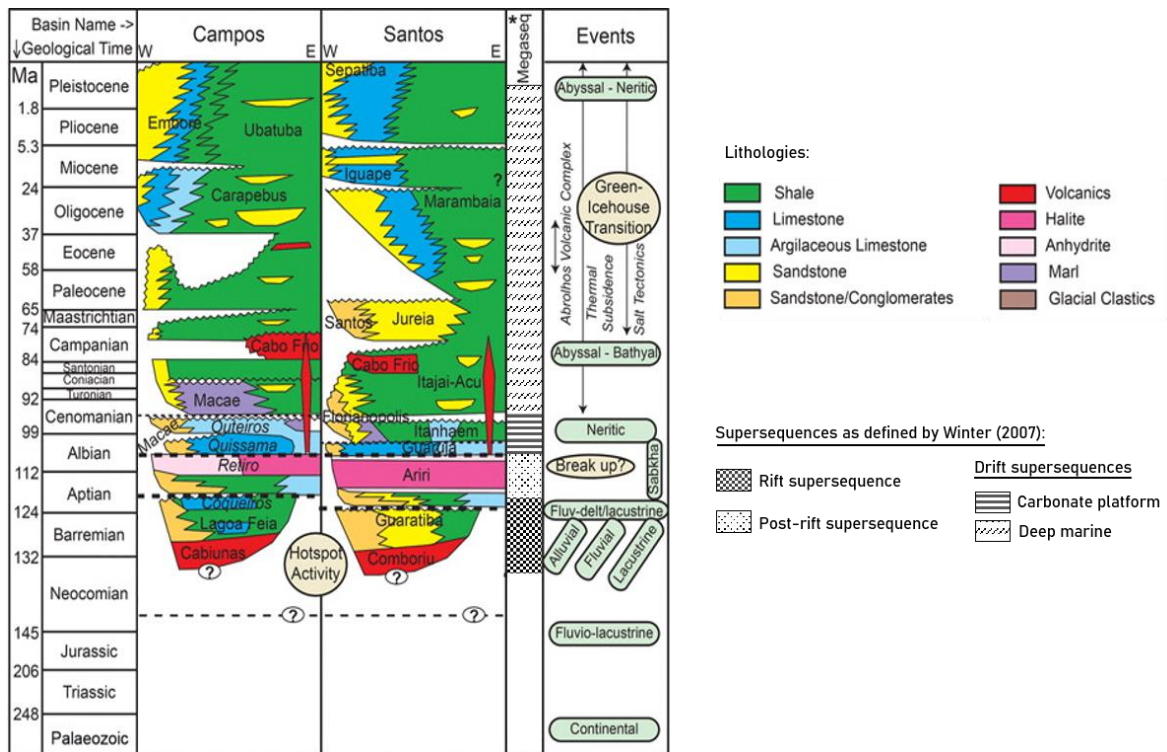


Figure 30. Generalized tectonostratigraphic evolution chart for the Campos and Santos basins. (Modified from BEGLINGER *et al.*, 2012).

The **rift supersequence** was generated during the initial evolution of the basin and is represented in Campos and Santos basins by both the volcanic Cabiúnas and Camboriu Formations and the basal interval of the Lagoa Feia and Guaratiba Groups, deposited from the Barremian to the Lower Aptian (LIMA and DE ROS, 2019). According to MCKENZIE (1978) and WHITE and MCKENZIE (1988), the rift phase of the basin was determined by the lithosphere extension and asthenospheric elevation, related to widespread intracratonic tholeiitic volcanism (TURNER *et al.*, 1994; MOHRIAK *et al.*, 2008; TORSVIK *et al.*, 2009 *apud* LIMA and DE ROS, 2019).

The **transitional megasequence** (CAINELLI and MOHRIAK, 1999) or **post-rift SAG supersequence** (MILANI *et al.*, 2007), the latest stage of the rifting, already without tectonic activities, contains the upper interval of the Lagoa Feia and Guaratiba Groups, deposited on the regional Pre-Alagoas unconformity during the Middle/Upper Aptian. The carbonate rocks of the post-rift SAG supersequence correspond to the **Macabu Formation** in the Campos Basin and the **Barra Velha Formation** in the Santos Basin.

The Macabu and Barra Velha Formations are predominantly constituted by shrubby and laminated limestones and dolostones, intraclastic grainstones and hybrid conglomerates and arenites, as well as spherulitic and dolomitic Mg-rich silicate claystones (PIETZSCH *et al.*, 2018), deposited in alkaline lacustrine environments under arid climate conditions, and which were originally interpreted as microbial stromatolites (DIAS, 2005; MUNIZ and BOSENCE, 2015 *apud* LIMA & DE ROS, 2019) and re-interpreted as chemical precipitates controlled by the geochemistry of lacustrine waters (TOSCA and WRIGHT, 2014; WRIGHT and BARNETT, 2014, 2015; WRIGHT and TOSCA, 2016 *apud* LIMA and DE ROS, 2019).

The upper portion of the supersequence is composed of a thick accumulation of evaporites (the salt layers) deposited during the advent of marine incursions under arid climate conditions, corresponding to the Retiro Formation in the Campos Basin and the Ariri Formation in the Santos Basin (LIMA and DE ROS, 2019).

#### 2.2.1.1. CO<sub>2</sub> occurrence and concentrations in pre-salt fields

D'ALMEIDA *et al.* (2018) analyzed the CO<sub>2</sub> concentrations in pre-salt fields in the Campos and Santos basins. Statistical analysis of the data showed that the Campos Basin has a predominance of CO<sub>2</sub> concentrations in the 0.5% range, however, concentrations of up to 20% occur in the region bordering the Santos Basin (Figure 31). According to D'ALMEIDA *et al.* (2018), in the Santos Basin, most of the wells analyzed have a low concentration of CO<sub>2</sub>, but the number of wells with concentrations above 5% is notable, reaching up to 80% of CO<sub>2</sub>

in some regions; higher concentrations of the gas were observed in the southeastern region of the Santos basin, in areas of ultra-deep waters in the region of the salt walls. In the Campos Basin, CO<sub>2</sub> concentrations are lower; however, there are some sectors in this basin where there are also high concentrations of the gas (D'ALMEIDA *et al.*, 2018).

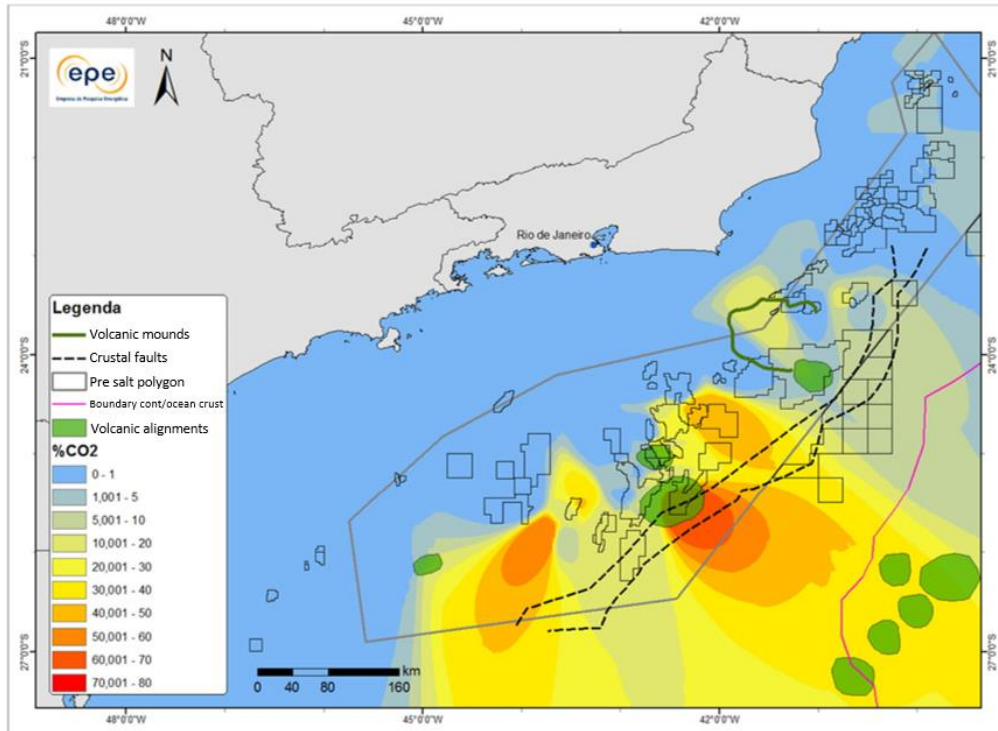


Figure 31. CO<sub>2</sub> concentration map on the east margin, with structural framework (D'ALMEIDA *et al.*, 2018).

### 2.2.2. Purbeck limestones

The Purbeck Limestone Group (Upper Jurassic-Lower Cretaceous) is part of the Wessex Basin, located in southern England and northern France (Figure 32). The basal part of the group is composed of the Mupe Member (Upper Tithonian), which includes the accumulation of in-situ build-ups of microbial mounds (with thickness from about 0.5 to 4m and high preserved primary porosity) within less-porous bedded inter-mound packstones-grainstones (GALLOIS and BOSENCE, 2017) from Cap beds (Skull Cap, Hard Cap, and Soft Cap) interspersed with carbonaceous mudstones from Dirt Beds (Basal Dirt Bed, Lower Dirt Bed and Great Dirt Bed), representing three shallowing-upward lacustrine sequences capped by emergent surfaces (paleosols), and overlapped by Broken Beds evaporites and Cypris Freestone bed carbonates (Figure 33).

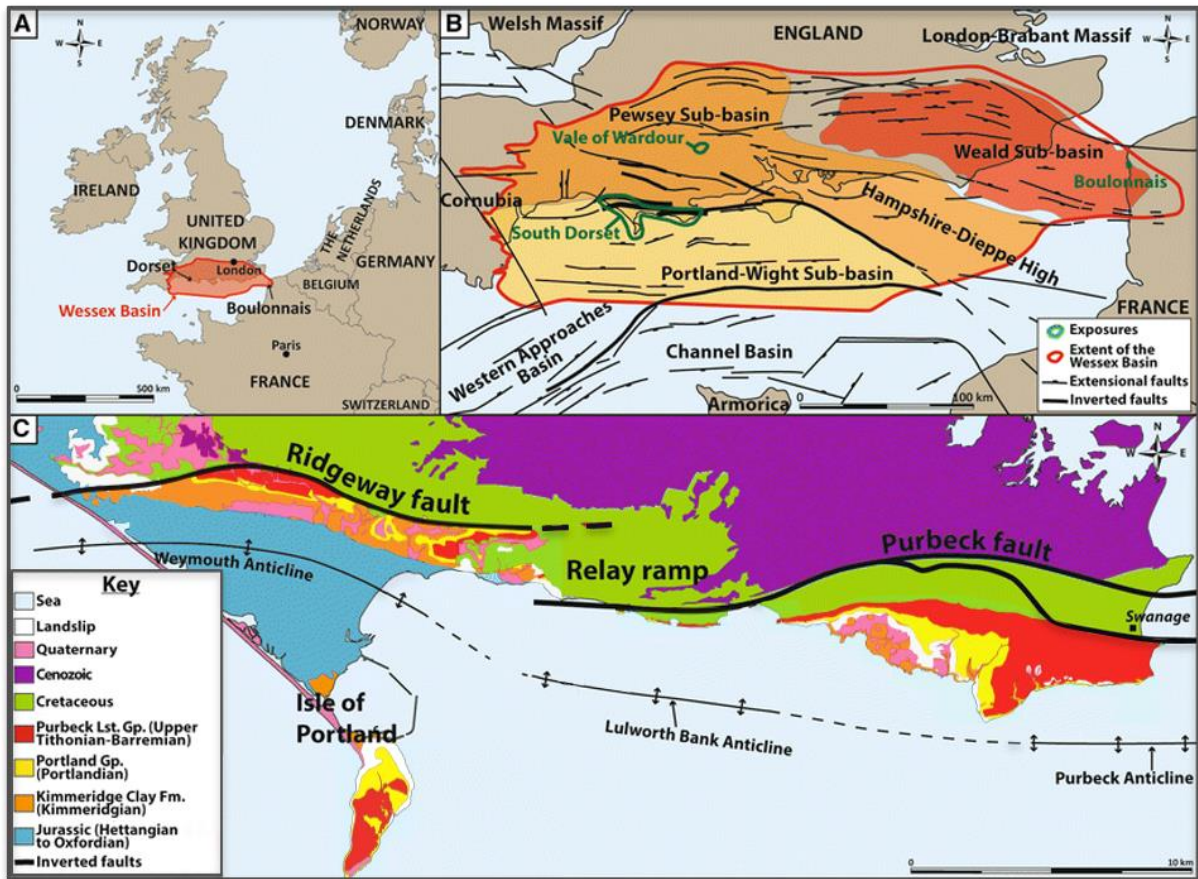


Figure 32. Location and geological setting. (A) Purbeck Limestone Group (red) exposures in UK and France; (B) Structural map of the Channel and Wessex Basins and sub-basins. The thick lines identify Mesozoic extensional faults inverted during the Alpine orogeny; (C) Simplified geological map of south Dorset with inverted faults (bold black lines) and associated anticlines (Modified from GALLOIS *et al.*, 2018).

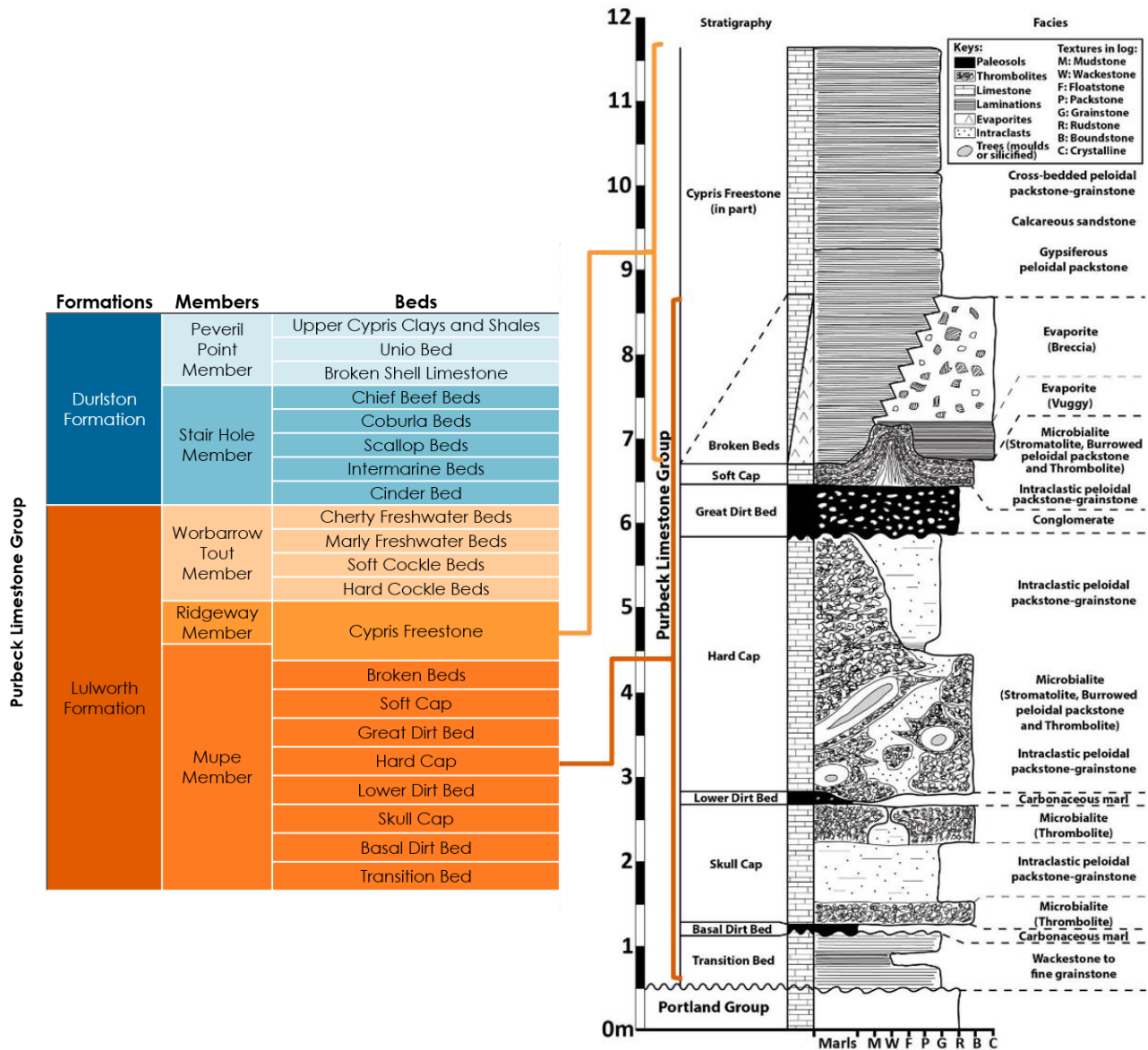


Figure 33. Purbeck Limestone Group formations, members and beds and idealized log for the Mupe Member in the Isle of Portland (UK), according to GALLOIS (2016).

### The Purbeck Limestone Group: an analogue to the Brazilian pre-salt

The Purbeck Limestone Group, deposited in the syn-rift phase of the Wessex Basin, is considered a partial analogue for the South Atlantic basins rift phase deposits, as they share a number of similarities.

The Atlantic margins are organized in several extensional basins that are elongated and about 200-300 km long; similarly, the Wessex Basin is about 400 km long, made of three extensional sub-basins (Figure 34) (GALLOIS, 2016).

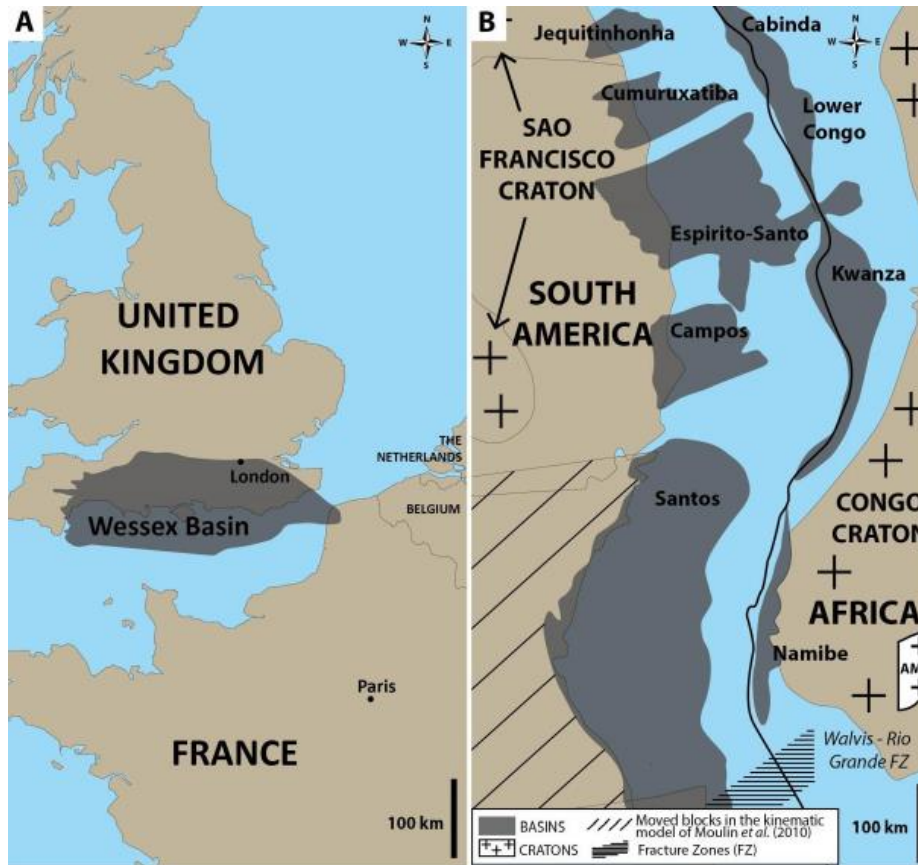


Figure 34. Size comparison between the Wessex Basin (A) and South Atlantic basins (B) (redrawn after CHABOUREAU *et al.*, 2013 *apud* GALLOIS, 2016).

The syn-rift phase is dated as Early Cretaceous for the Brazilian and West African margin basins (Mid-Hauterivian to Early Aptian, Figure 35) (BEGLINGER *et al.*, 2012 *apud* GALLOIS, 2016) and as Late Jurassic-Early Cretaceous for the Wessex Basin (Figure 35). Syn-rift deposits in both cases occurred in basins created on the hanging-wall blocks of extensional faults along the margins of these basins (NORVICK and SCHALLER, 1998; CALASSOU and MORETTI, 2003; DICKSON *et al.*, 2003; BEGLINGER *et al.*, 2012 *apud* GALLOIS, 2016).

Both developed under at least temporary lacustrine conditions, but the southeast Atlantic deposits seemingly evolved in progressively more saline lacustrine shallow water (from fresh to brackish to saline waters) with the development of microbial build-ups on fault blocks in a syn-rift setting (GALLOIS, 2016; KIRKHAM and TUCKER, 2018) while the lower Purbeck limestones are interpreted to be deposited in lakes with waters evolving from brackish to saline to freshwater, overlain by sulfate evaporites (gypsum and anhydrite) (GALLOIS, 2016).

Eras, Sub-eras, periods		Brazilian basins		Wessex Basin		West African basins	
		Main lithologies	Basin evolution	Main lithologies	Basin evolution	Main lithologies	Basin evolution
Cenozoic	Neogene	Marine clastic sedimentation Shallow to deep	Post-rift	NOT PRESENT		Marine clastic sedimentation Shallow to deep	Post-rift (drift-marginal sag)
	Paleogene			Marine (clastics and carbonates)	Alpine inversion		
	Eocene			GAP			
Mesozoic	Late Cretaceous	Shallow-marine (ramp carbonates)	Syn-rift	Deep-marine (carbonates)	Post-rift	Shallow-marine (ramp carbonates)	Fluv. Ma.    Restr. Mar.
	Albion			Continental (clastics)			
	Early Cretaceous	Lacustrine    Saline Brackish Fresh		Lacustrine    Fresh Saline Brackish	Syn-rift	Lacustrine    Saline Brackish Fresh	Syn-rift
	Val. Berr.	Basalt	Pre-rift	Shallow-marine (carbonates)		Lacustrine	
	Jurassic			Deep-marine		Fluvial	Pre-rift
						Alluvial	

Figure 35. Comparison of basin evolutions between Brazilian margin basins (modified after MOREIRA *et al.*, 2007), the Wessex Basin of southern England (modified after Underhill, 1998) and West African margin basins (modified after BEGLINGER *et al.*, 2012). The red areas highlight intervals of GALLOIS (2016) study and their counterparts in the South Atlantic. Modified from GALLOIS (2016).

The differences between the South Atlantic and the Wessex Basins are the hydrology evolution of the lakes and the mineralogies (dolomite, calcite, and silica in the south Atlantic and only calcite in the Wessex Basin) (GALLOIS 2016). However, both basins present similarities with the basin sizes about 300-400 km across; the basin evolution as the deposition occurred in lacustrine and syn-rift evolution of the basins; the occurrence of microbialites (thrombolites); and the facies distribution (coarse-grained in shallow areas and fine-grained in deeper areas) (GALLOIS 2016).

### 2.2.2.1. Petrophysical studies in Purbeck limestones

This section brings together the results of some petrophysical studies available in the literature performed on Purbeck limestone samples.

OGILVIE *et al.* (2002) and GLOVER *et al.* (2006) utilized Purbeck limestone samples to propose a new permeability prediction model (RGPZ model) considering the link between electrical conductivity and fluid permeability of porous rock. Petrophysical data from Purbeck limestone published in GLOVER *et al.* (2006) are gathered in Table 1.



Table 1. Petrophysical data from Purbeck limestone samples (GLOVER *et al.*, 2006).

Purbeck limestone samples	Perpendicular bedding	Isotropic bedding
Number of samples	2	4
Helium porosity (%)	0.13 – 0.14	0.04 – 0.13
Formation factor	45.80 – 65.30	35.80 – 399.70
Cementation exponent	1.87 – 2.12	1.75 – 1.87
Modal grain size (MICP) ( $\mu\text{m}$ )	14 – 30	20 – 40
Klinkenberg permeability ( $\text{m}_2 \times 10^{-15}$ )	0.036 – 0.090	0.0019 – 0.49

NORTH *et al.* (2013) utilized Purbeck limestone samples to propose a “*measurement system capable of determining the full resistivity tensor of core samples at elevated, geologically representative, pressures using a galvanic method*”. Petrophysical data published in the paper are gathered in Table 2.

Table 2. Petrophysical data from Purbeck limestone samples (NORTH *et al.*, 2013).

Purbeck limestone samples	Porosity (%)	Permeability (mD)
A	22	723
B	21.6	452
C	21.1	393

CARVALHO *et al.* (2019), which used Purbeck samples taken from the same location as the samples to be used in this research, developed acid microemulsions aiming to improve the stimulation process and reduce the problems caused by using acidic solutions in Purbeck samples. Petrophysical data published in the paper are gathered in Table 3 and the chemical composition of the samples is gathered in Table 4.

Table 3. Petrophysical data from Purbeck limestone samples (CARVALHO *et al.*, 2019).

Purbeck limestone samples	Volume of pores ( $\text{cm}^3$ )	Total volume ( $\text{cm}^3$ )	Helium porosity (%)	Permeability (mD)
R1	2.55	103.30	2.47	2.31 E – 03
R2	4.58	107.40	4.27	8.36 E – 03
R3	1.66	111.34	1.49	1.93 E – 03
R4	6.16	108.95	5.66	3.64 E – 03
R5	8.47	107.72	7.87	6.06 E – 03
R6	6.14	111.29	5.52	2.69 E – 03

Table 4. Purbeck sample composition by X-ray fluorescence (CARVALHO *et al.*, 2019).

Purbeck limestone sample	MgO (%)	Al <sub>2</sub> O <sub>3</sub> (%)	SiO <sub>2</sub> (%)	SO <sub>3</sub> (%)	CaO (%)	LBC (%)*
	0.42	0.14	3.80	0.22	54.70	40.40

\* Loss by calcinations.

BLAMEY *et al.* (2010) presented experiments seeking to establish how CaO sorbents for CO<sub>2</sub> capture perform after “reactivation” by hydration. The chemical composition of the Purbeck samples published in the paper is gathered in Table 5.

Table 5. Purbeck sample composition by X-ray fluorescence, with fractions of CaO and MgO converted to CaCO<sub>3</sub> and MgCO<sub>3</sub>, respectively (BLAMEY *et al.*, 2010).

Purbeck limestone sample	CaCO <sub>3</sub> (%)	MgCO <sub>3</sub> (%)	SiO <sub>2</sub> (%)	Fe <sub>2</sub> O <sub>3</sub> (%)	Al <sub>2</sub> O <sub>3</sub> (%)	P <sub>2</sub> O <sub>5</sub> (%)	K <sub>2</sub> O (%)	MnO (%)
	93.90	0.21	0.29	0.04	0.04	0.02	0.01	n/a

BRANTUT *et al.* (2014) performed triaxial deformation experiments on water-saturated porous Purbeck samples under constant strain rate and constant stress (creep) conditions at room temperature and low effective pressures, in the brittle regime, while BRANTUT *et al.* (2018) performed triaxial deformation experiments across the brittle-ductile transition, and both monitored the evolution of permeability and wave velocities as a function of strain.

WANG *et al.* (2018) and MENG *et al.* (2019) investigated the effective stress behavior of Purbeck samples, characterizing the effective stress coefficients for permeability and pore volume change, and bulk strain through high-pressure compression tests at room temperature on water-saturated samples. For this, WANG *et al.* (2018) characterized the pore space of these samples, identifying significant fractions of macropores and micropores, and determined that these limestones cannot be modeled as microscopically homogeneous. Effective pore throat diameter (Figure 36), pore size distribution (Figure 37), and T<sub>2</sub> relaxation time distribution (Figure 38) were also obtained by the researchers.

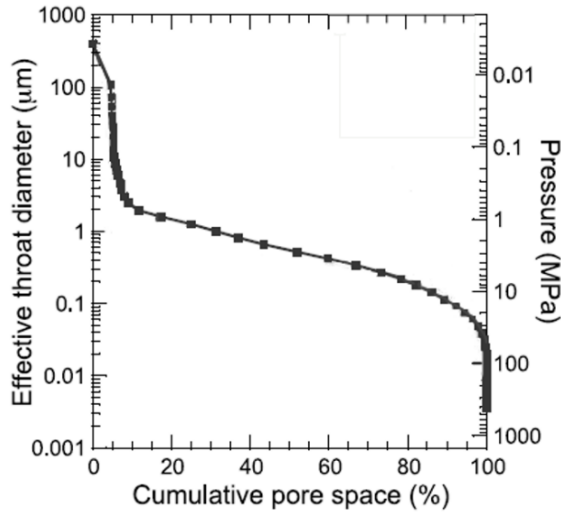


Figure 36. Effective pore throat diameter and the corresponding mercury capillary pressure as functions of cumulative pore space inferred from mercury injection tests on Purbeck undeformed samples. Modified from WANG *et al.* (2018).

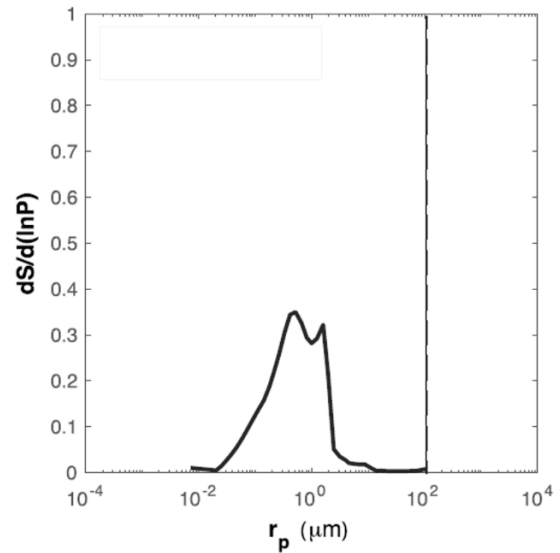


Figure 37. Pore size distribution calculated with logarithmic derivative  $dS/d(\ln P)$ , inferred from mercury injection measurements in Purbeck samples, showing bimodal distribution. Modified from WANG *et al.* (2018).

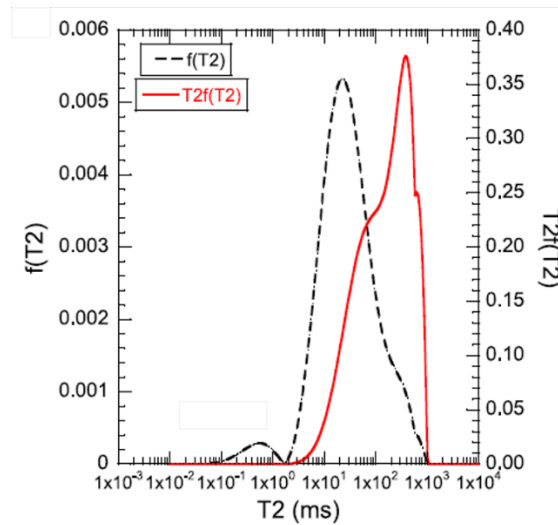


Figure 38.  $T_2$  relaxation time distribution,  $f(T_2)$  (dashed black line), and the  $T_2$ -weighted probability distribution function,  $T_2f(T_2)$  (solid red line), inferred from NMR measurements on undeformed Purbeck samples (WANG *et al.*, 2018).

# Chapter 3

## Materials and Methods

Eleven blocks of carbonates from the Purbeck Formation (southern UK) - which are considered by GALLOIS (2016) and GALLOIS and BOSENCE (2017) as a possible analogue to the Brazilian Pre-Salt – were donated by Baker Hughes to the National Observatory's Petrophysics Laboratory (LabPetrON). In these blocks, two sedimentary facies were visually identified: a vuggy/microbial one and a laminated to a massive one.

Five blocks were selected to core three plugs from each, which went through several experimental and analytical procedures (see section 3.2). Furthermore, four small pieces representative of the identified facies (two of each) were selected in order to chemically and mineralogically characterize the facies, as will be discussed as follows.

### 3.1. Chemical and mineralogical characterization

#### 3.1.1. X-ray diffraction (XRD)

Two samples provided from the cut blocks were selected for XRD analysis at the Mineral Technology Center (CETEM), by using the Rietveld Method to characterize the crystalline phases present. The sensitivity of the equipment is 0.3-0.5% in mass. Figure 39 shows the analyzed samples.

Our results indicated the chemical composition of the blocks from which the plugs were removed, which made it possible to obtain a general idea of the mineralogical composition of these rocks and estimate the changes generated by the carbonated water injection.



Figure 39. Samples analyzed by XRD; IS-1 (left) represents the vuggy facies and IS-2 (right) represents the laminated/massive facies.

### 3.1.1. Petrographic thin sections

Two other samples of vuggy/microbial and laminated/massive carbonate facies taken from the blocks were selected for petrographic thin sections confection at the Geological Sample Processing Laboratory (LGPA) at the State University of Rio de Janeiro (UERJ).

The thin sections (one of each sample) were described and photographed using a Zeiss Axio Lab A1 optical microscope with an attached camera, available at the Petrography Laboratory (LPETRO) of the Faculty of Geology at UERJ.

The analysis of the thin sections made it possible to analyze in more detail the mineralogical composition and the pore types of these rocks.

## 3.2. Plugs preparation

### 3.2.1. Coring and cleaning

In order to perform the following analysis, 15 plugs with 1.5 inches in diameter (about 3.8 cm) and between 1.6 and 2.8 inches (about 4 to 7 cm) in length were cored from five blocks. Three plugs of each were removed, two parallel to the sedimentary bedding ( $x$  and  $y$  directions) and one perpendicular to the bedding ( $z$ -direction) (Figure 40).

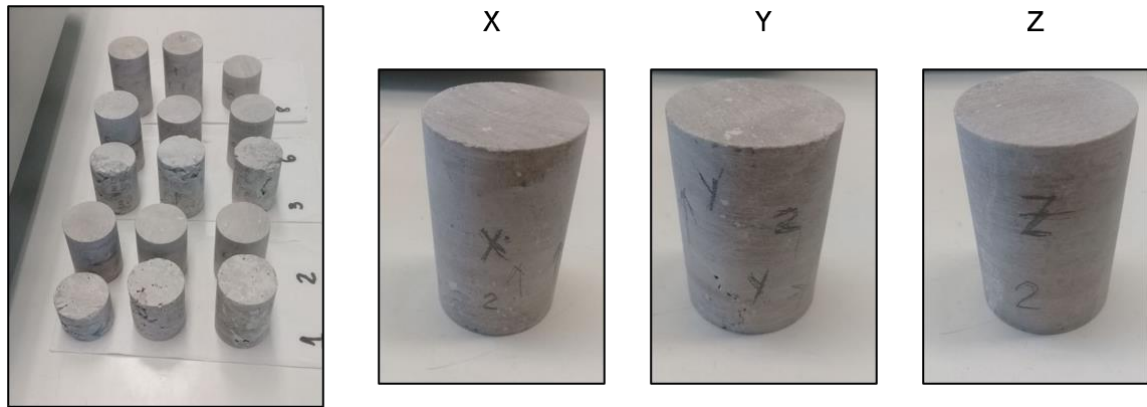


Figure 40. Photos of plugs taken from the selected five blocks.

The plugs were cored at LabPetrON by using a diamond-tipped, hollow cylindrical, rotary core bit mounted on a drill press and were subsequently trimmed and face grinded using a diamond tooled trim saw to adjust the top and base of the plugs, making them orthogonal to the axis so that they were as close to a perfect cylinder. Once prepared, the plugs were cleaned using the Hot Soxhlet extraction method with toluene and methanol circulation and dried in an oven.

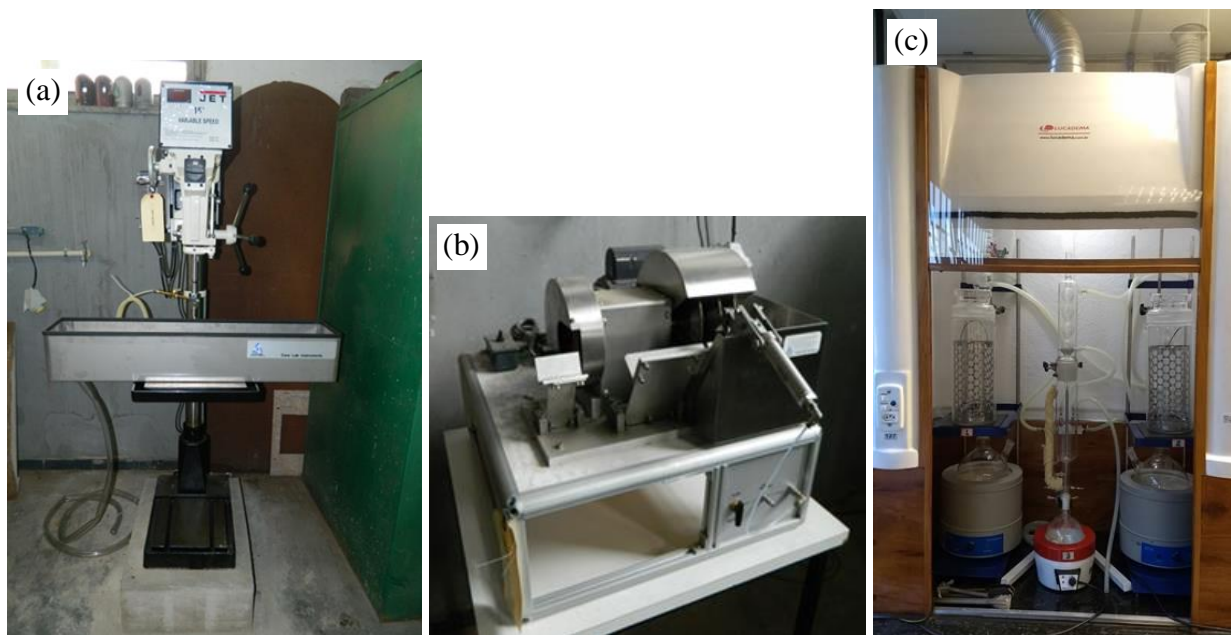


Figure 41. (a) drilling press diamond tool from Corelab Instruments; (b) trim saw from Corelab Instruments; (c) chapel with hot Soxhlet equipment.

Source: [LabPetrON](#)

### 3.3. Pre-injection analysis

The plugs underwent pre carbonated water injection analyzes to determine the petrophysical characteristics of the rock and collect information that will be compared with the results of the same analyzes after the coreflood.

#### 3.3.1. Routine petrophysics

The plugs underwent routine petrophysical characterization by using a gas porosimeter and permeameter to obtain effective porosity and absolute permeability values, available at the Enhanced Oil Recovery Laboratory (LRAP) at the Federal University of Rio de Janeiro (UFRJ). The equipment used has the following specifications: porosimeter and permeameter model DV-4000 (Weatherford Laboratories, USA), with matrix cup and core-holder for plugs with a standard diameter of 1.0 and 1.5 inches, both with variable length up to 10.0 cm, using helium for porosity and nitrogen for permeability measures at a pressure of 500 psi (Figure 42).



Figure 42. LRAP's porosimeter and permeameter. Source: [LRAP](#).

Six of the plugs (Figure 43) indicated too low porosity and permeability to be correctly measured and three plugs (Figure 44) were not analyzed due to the possibility of grains loosening and damaging the equipment.

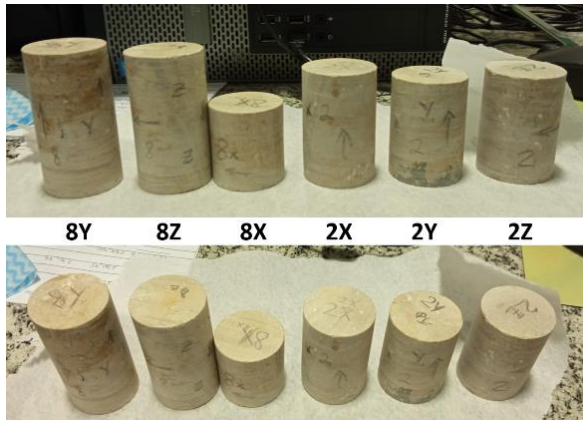


Figure 43. Plugs with extremely low porosity (below 3%) and permeability (close to 0 mD).

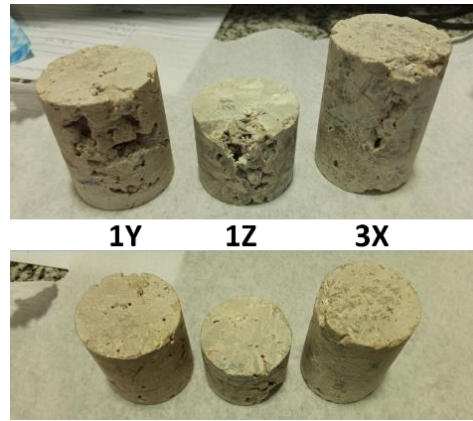


Figure 44. Plugs with the possibility of grains loosening.

Based on our routine petrophysical results, the six plugs that showed measurable porosity and permeability values (Figure 45) were selected to go through more pre-injection analysis to obtain a more detailed characterization.

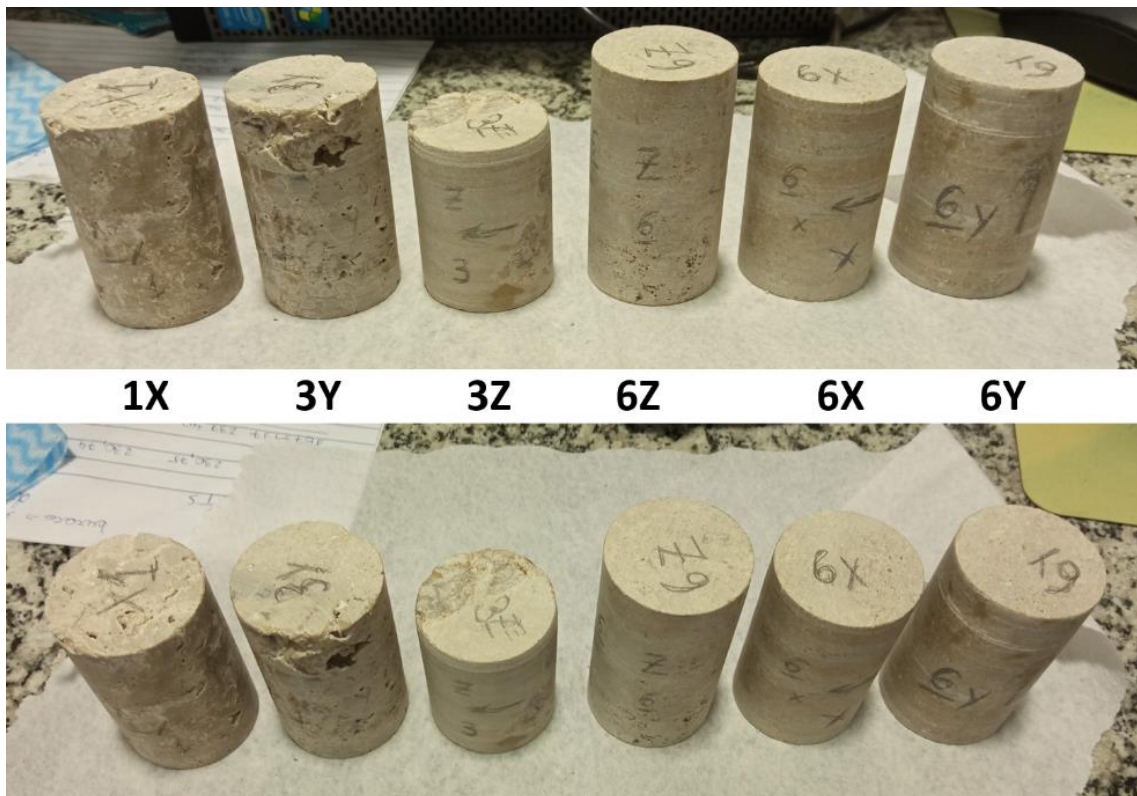


Figure 45. Plugs that follow to the next steps of analysis.

The plugs selected for further analysis were cored from blocks 1, 3, and 6, with plugs from blocks 1 and 3 being plugged from the vuggy/microbial facies and block 6 representing the laminated/massive facies (Figure 46).





Figure 46. Blocks from which the plugs that proceeded in the analysis were removed.  
From left to right, blocks 1, 3 and 6.

### 3.3.2. Nuclear Magnetic Resonance (NMR)

The six core samples were saturated with distilled water under 1000 psi by using a manual sample saturator (Vinci Technologies, France), available at LabPetrON (Figure 47). Saturated, the samples were stored in a closed container filled with the saturation fluid. Subsequently, they were transported to the Geophysics and Petrophysics Laboratory (LAGEP) at UFRJ to be analyzed in the nuclear magnetic resonance (NMR) equipment model Maran 12MHz (Oxford Instruments, UK) (Figure 48).

After injecting CWI into the samples, the NMR analyzes were repeated in another laboratory, using the equipment model SPECFIT 14 (Fine Instrument Technology, Brazil), available at LRAP (Figure 49).

From the  $T_2$  decay measurements, was possible to provide the pore volume (porosity), estimated permeability, and, especially, the pore size distribution of the plugs, which allowed us to identify the alterations generated by the percolation of carbonated water in the increase or decrease in the quantity of each pore size.

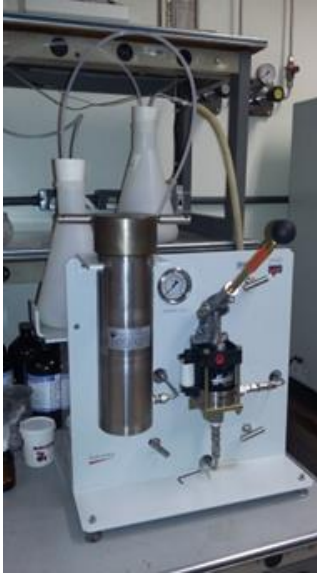


Figure 47. LabPetrON's sample saturator.  
Source: [LabPetrON](#).



Figure 48. LAGEP's NMR equipment.  
Source: [LAGEP](#).



Figure 49. LRAP's NMR equipment.  
Source: [LRAP](#).

### 3.3.3. X-Ray Computed Microtomography (micro-CT or $\mu$ -CT)

The plugs were imaged via the micro-CT model CoreTOM (TESCAN, USA) (Figure 50), available at LRAP, before the carbonated water injection step to make it possible to identify in detail the changes generated in the porous space of the samples by the injection, this through the comparison of images obtained before and after the injection.

The images were obtained with a 25  $\mu$ m resolution. Scanning parameters were set at 160 kV, 10  $\mu$ A for operating voltage and current, and the exposure time was 330 ms. A copper filter (1  $\mu$ m) was used to improve image quality. After the reconstruction, 16-bit images were generated.



Figure 50. LRAP's micro-CT equipment. Source: [Tescan](#).

Afterward, the images were processed to analyze the percentage of dark parts – the pores. The processing consisted of (Figure 51):

1. Removal of firsts and lasts scans (due to being prone to boundary effects);
2. Crop the images to a circular shape to remove parts of the image that are not part of the plug;
3. Image noise reduction using the *Median 3D filter* ( $x=1.5, y=1.5, z=1.5$ );
4. Thresholding using the *Otsu method* (OTSU, 1979);
5. Calculating the percentage of areas highlighted in the previous step using *Analyze Particles*, selecting the *Pixel units*’ option.

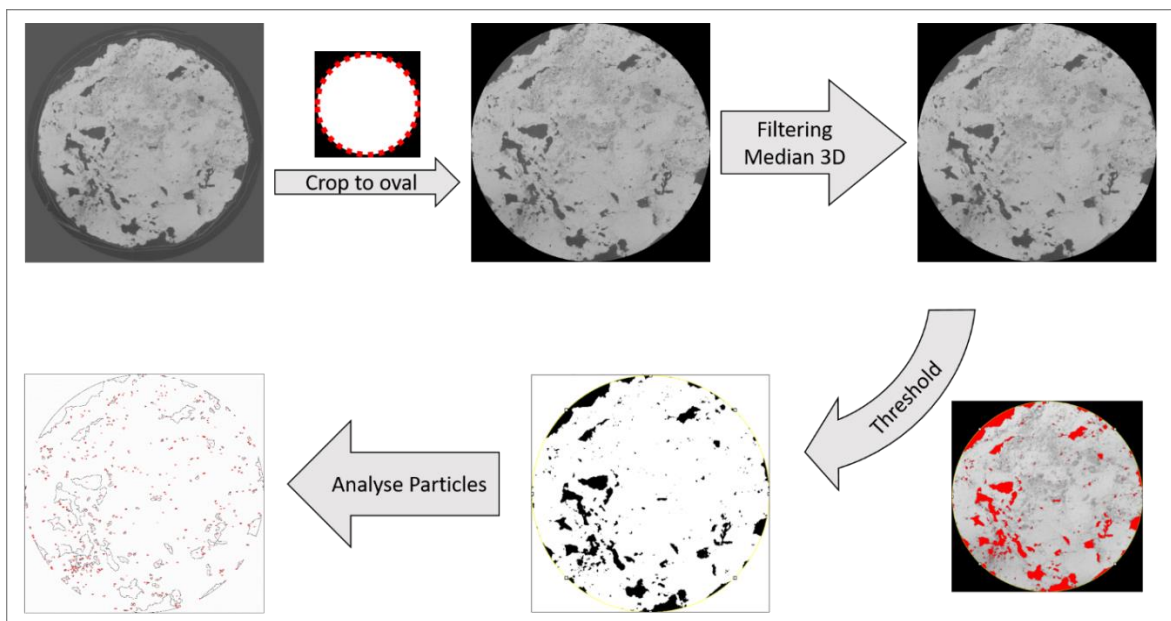


Figure 51. Schematic sequence of Micro-CT image processing performed in Fiji software (ImageJ).

### 3.4. Carbonated water injection

The coreflooding experiments were performed at LRAP in an apparatus whose scheme is shown in Figure 52. The entire procedure was performed at room temperature (20-21°C). Injection pressure control and generated data collection were performed using LabVIEW 2016 software, provided by National Instruments

The preparation of the CO<sub>2</sub> mixture with the DSW was carried out by connecting the container with pressurized CO<sub>2</sub> at 2050 psi and another container with DSW at 2000 psi and, with valve V<sub>1</sub> open, 6ml of water was removed to allow the entry of the same volume of CO<sub>2</sub> into the container (Figure 53).

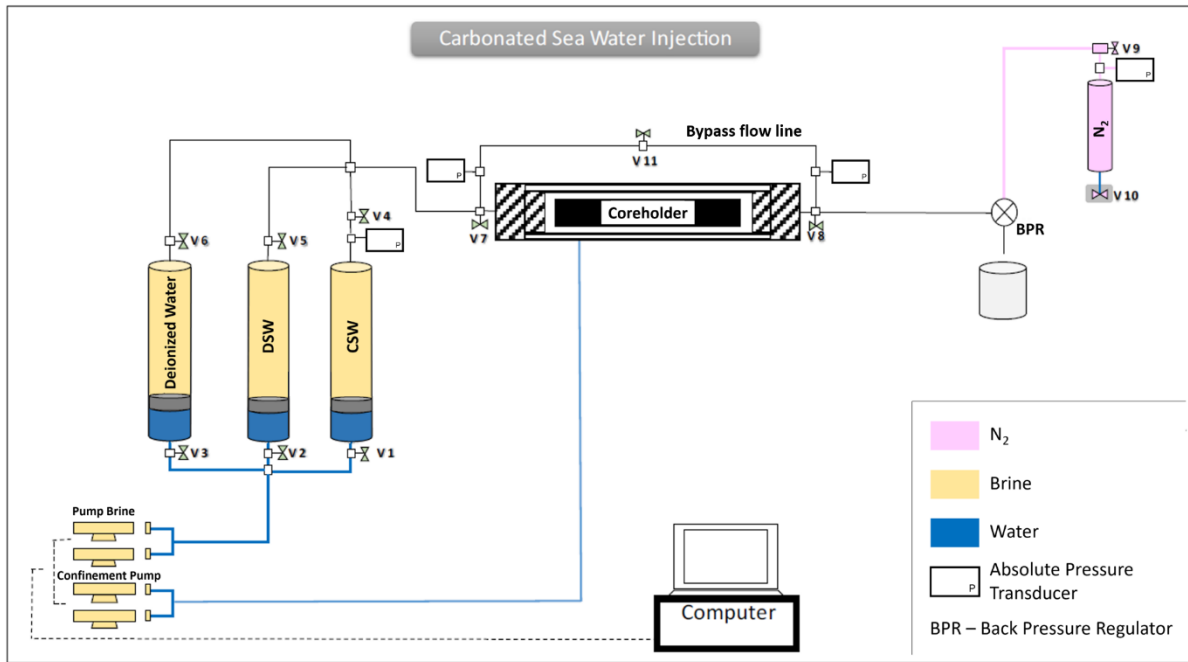


Figure 52. Schematic depiction of the apparatus used for DSW, CSW and DW injection, provided by LRAP team.

In each experiment, the core, previously saturated with desulphated sea water (DSW) – chemical data in Table 6 –, was placed in the coreholder after being covered with a white thread seal tape, aluminum paper, a thin layer of Vaseline and enveloped by a plastic sleeve to isolate the core from the rest of the coreholder – which avoids contact between injection and confinement fluid (deionized water or DW), preventing CO<sub>2</sub> leakage and sample contamination.

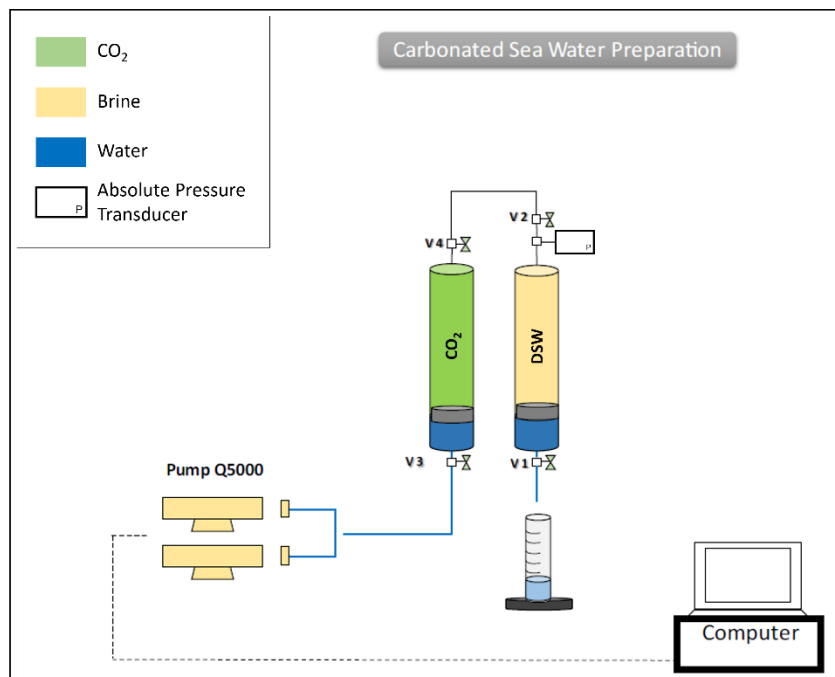


Figure 53. Schematic drawing of the CSW preparation, provided by LRAP team.

### CHAPTER 3. MATERIALS AND METHODS

The core was confined at 500 psi and DSW was injected into the sample at 1 cc/min. The system pressure was increased to 2000 psi (keeping the core's confinement pressure value) and the differential pressure ( $\Delta P$ ) started to be registered by the software NI LabVIEW 2016. After stabilization of the system pressure, the  $\Delta P$  registered was utilized to determine the permeability to DSW ( $k_w$ ) – which, when compared to the gas permeability results, is used to confirm the injection pressure stabilization.

After, the carbonated sea water (CSW), composed of 94% of DSW and 6% of liquid  $\text{CO}_2$ , was injected into the core also at 1 cc/min. The number of pore volumes (nPV) injected in each sample was decided previously by determining a different PV for each plug of a pair with similar permeability values (Table 13).

After finished the CWS injection, a few pore volumes of DW were injected into the core, the system was depressurized, and the sample was removed from the coreholder.

Effluent fluid samples were collected at the system outlet to be analyzed by Ion Chromatography and to determine the amount of rock dissolution generated by the CSW injection: one aliquot during the initial injection of DSW, one for each injected nPV of CSW, and two after the injection of 10 and 20 cc of DW at the end of the experiment.

Table 6. Ionic composition (ppm), total dissolved solids TDS, pH, and density ( $\rho$ ) for the Desulphated Sea Water (DSW) used in this work, developed in LRAP.

<b>Ion</b>	<b>DSW</b>
$\text{Na}^+$	9543
$\text{Ca}^{2+}$	350
$\text{Mg}^{2+}$	1150
$\text{K}^+$	357
$\text{Sr}^{2+}$	9
$\text{Cl}^-$	18990
$\text{HCO}_3^-$	101
TDS (ppm)	30500
pH*	7.0
$\rho$ (g/ml)*	1.03

\* At 25 °C and 14.7 psi.

### 3.4.1. Ion chromatography (IC)

The IC analysis was performed at LRAP using the equipment Metrohm Ion Chromatograph model 940 Professional IC Vario and the columns Metrosep A Supp 5 150/4.0 for anion separation and Metrosep C 6 150/4.0 for cation separation.

For the sample preparation, each sample was diluted, filtered, and injected directly into the chromatograph in a simultaneous analysis method.

### 3.5. Post-injection analysis

Lastly, the samples' post-coreflooding petrophysical analysis was carried out, performing some of the analyzes previously mentioned (routine petrophysical characterization, micro-CT, NMR) seeking to identify the petrophysical and mineralogical changes of these samples generated by the carbonated water injection.

Table 7. Activities performed, equipment/techniques and laboratories.

Activity		Equipment	Laboratory	
Preparation	Rock plugging	Drill press and trim saw	LabPetrON	
	Plug cleaning	Hot Soxhlet		
	Plug drying	Oven		
Pre-coreflooding	Mineral phases identification	X-ray diffractometer	CETEM-UFRJ	
	Petrographic thin sections	Confection	LGPA-UERJ	
		Description	Petrographic Microscope	LPETRO-UERJ
	Petrophysical measurements	Porosity measurement	Helium porosimeter	LRAP
		Permeability measurement	Nitrogen permeabilimeter	
		T <sub>2</sub> decay measurement	NMR equipment	LAGEP-UFRJ
Characterize the pore structure in three dimension detail		CT scanner	LRAP-UFRJ	
Core flooding	Carbonated water flow	LABCON	LRAP-UFRJ	
	Brine sample analysis	Ion chromatography		

<b>Post-coreflooding</b>	Petrophysical measurements	Porosity measurement	Helium porosimeter	LRAP-UFRJ
		Permeability measurement	Nitrogen permeabilimeter	
		T <sub>2</sub> decay measurement	NMR equipment	
	Characterize the pore structure in three dimension detail	CT scanner		

# Chapter 4

## Results and discussion

### 4.1. X-ray diffraction (XRD)

The results of the XRD analyzes realized in block samples are gathered in Table 8. They indicate that the samples are composed almost entirely of low magnesium calcite, with smaller quantities of quartz and barite.

Table 8. Result of XRD analysis of IS-1 and IS-2 samples.

Phase Name	Chemical formula	IS-01	IS-02
		Wt% Rietveld	Wt% Rietveld
Quartz	SiO <sub>2</sub>	3.5	0.6
Magnesian Calcite	(Ca <sub>0.998</sub> , Mg <sub>0.002</sub> ) CO <sub>3</sub>	96.5	98.4
Barite	BaSO <sub>4</sub>	0	1
Total		100	100
Mg (in calcite)		0.001	0

### 4.2. Thin sections

The thin sections were observed under the microscope, photographed, and interpreted. The interpretations were made by consulting GALLOIS (2016) thesis, which made a detailed and extensive petrographic analysis of the same rocks, as well as the literature related to carbonate rocks.

Thin section IS-ON-1 (Figure 54), corresponding to the laminated/massive facies, is rich in micritic matrix with sparse chalcedony spherules (Figure 56). In porous zones, sparry calcite crystallized, probably due to the passage of calcitic fluid during burial (Figure 57). The carbonate rock can be classified as a wackestone, according to DUNHAM (1962) classification. The main porosity types observed are vugular, intergranular, moldic, and microporosity.

Thin section IS-ON-2 (Figure 55), corresponding to the vuggy/microbial facies, presents a branched columnar thrombolytic structure made of peloids, chalcedony spherules, and micrite matrix vertically stacked with poorly marked laminations (Figure 58), occurring



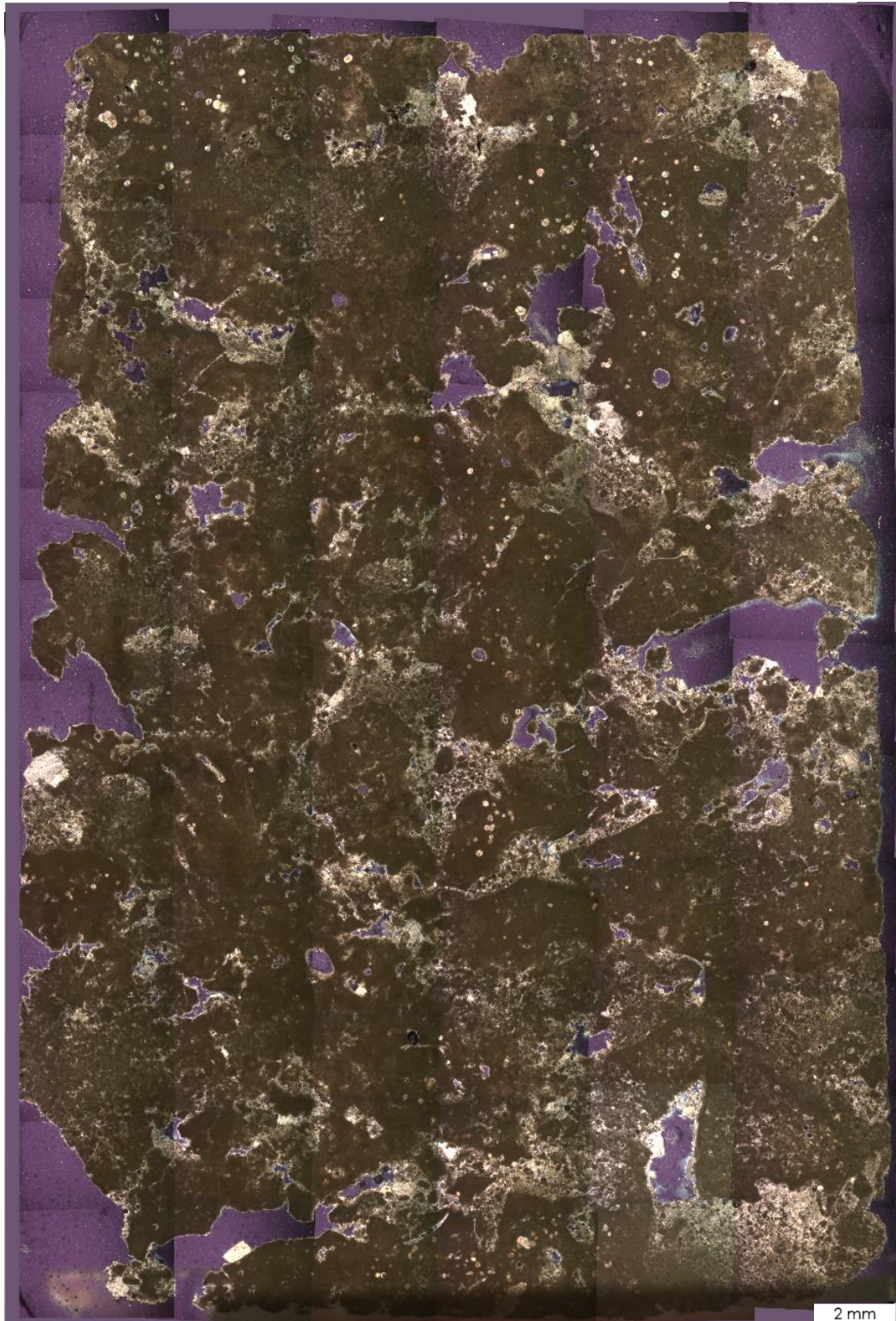


Figure 54. Scan of the IS-ON-1 thin section generated manually by pasting photos in mosaic style. The photos were obtained in a petrographic microscope under polarized light, with a 2.5x magnification.

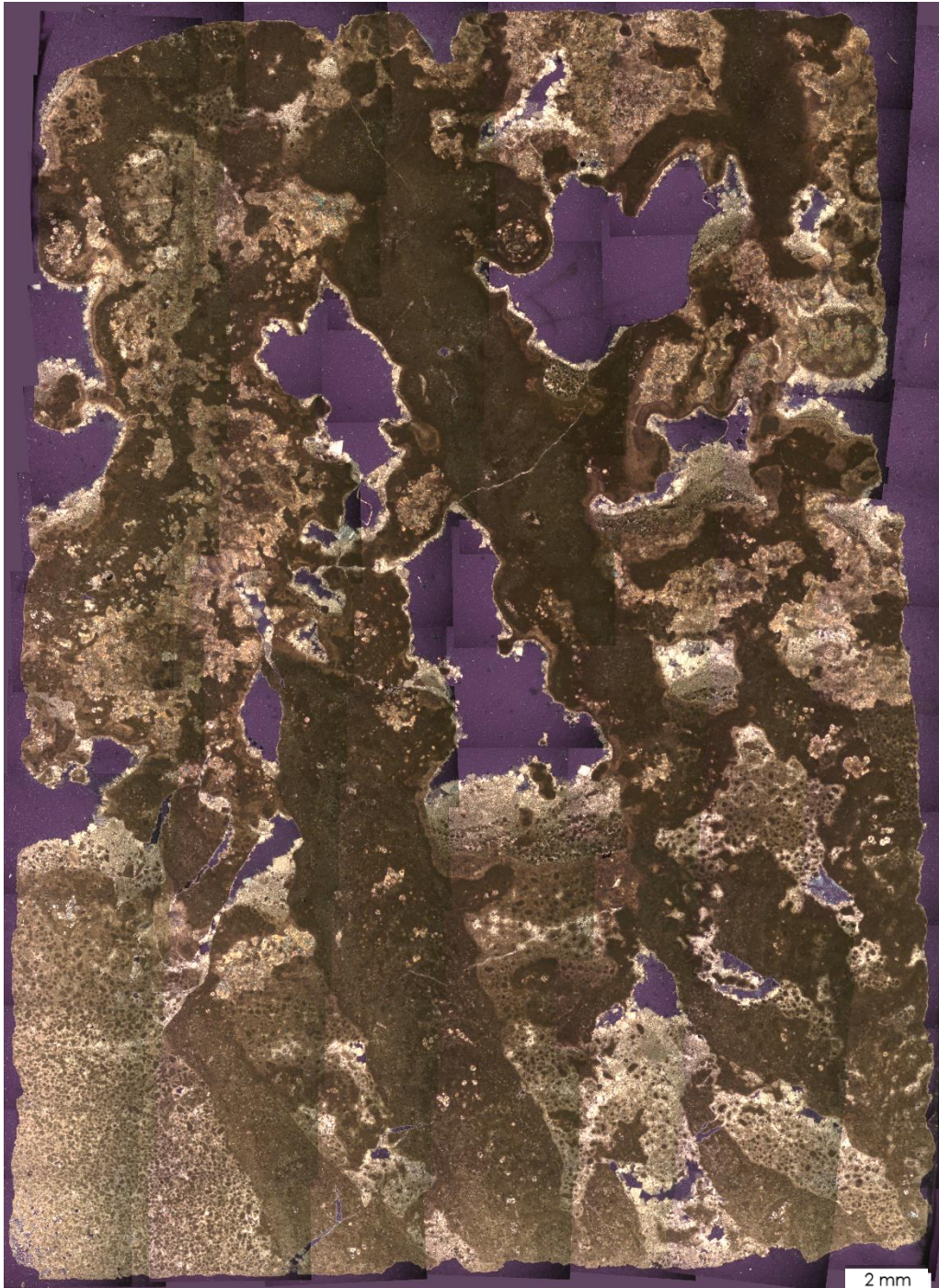


Figure 55. Scan of the IS-ON-2 thin section generated manually by pasting photos in mosaic style. The photos were obtained in a petrographic microscope under polarized light, with a 2.5x magnification.

laterally with zones rich in peloids and sparry calcite cement. The sample also presents sparry calcite crystallized in the pore's walls. The rock can be classified as a thrombolite according to AITKEN (1967) classification. The main porosity types observed are vugular, intergranular, growth-framework, and microporosity.

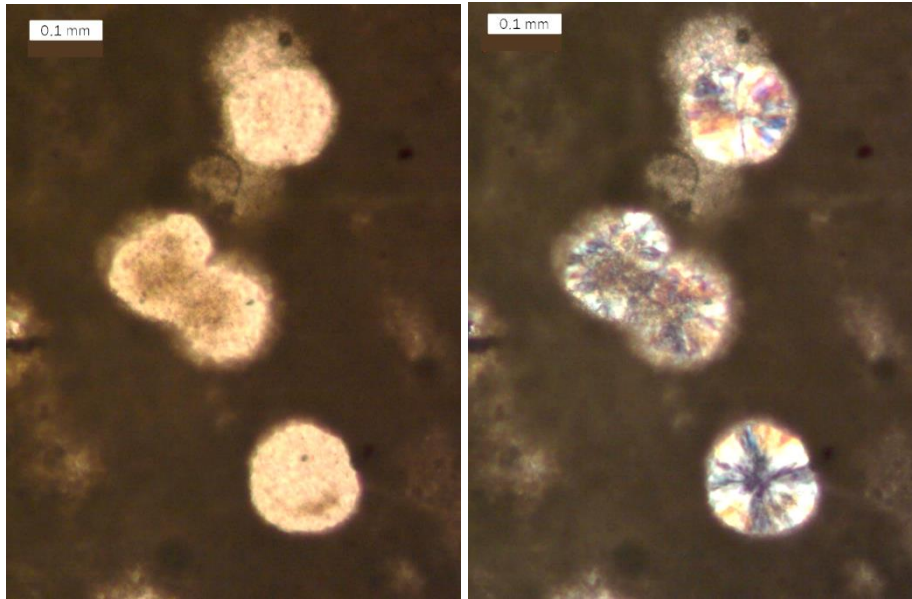


Figure 56. Brownish nodular crystals under natural light (left) and radial extinction cross under polarized light (right) in thin section IS-ON-1, with a 10x magnification. GALLOIS (2016) interpreted these crystals as chalcedony spherules, the result of the recrystallization of the micritic matrix.

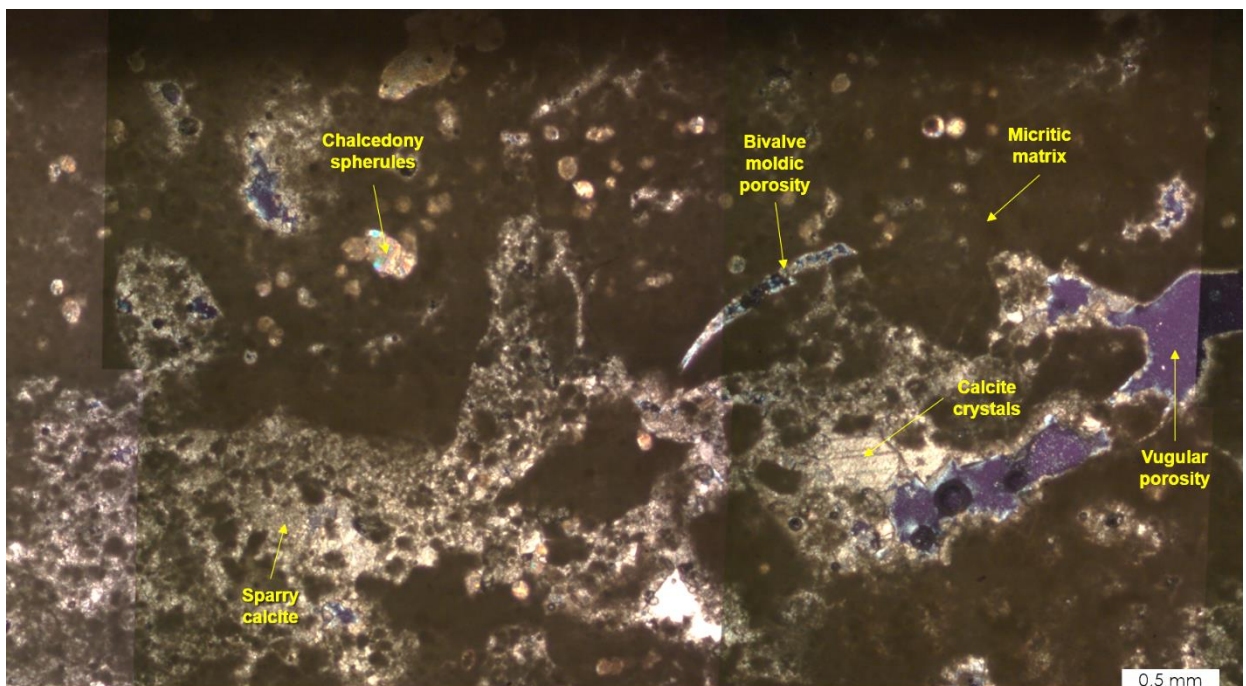


Figure 57. Detail of the IS-ON-1 scan image, highlighting the parts rich in micritic matrix with sparse chalcedony spherules and the porous regions with sparry calcite with well-formed calcite crystals on the walls of the vugular pores, in addition to the presence of moldic pores generated by the dissolution of fossil shell (likely bivalve).

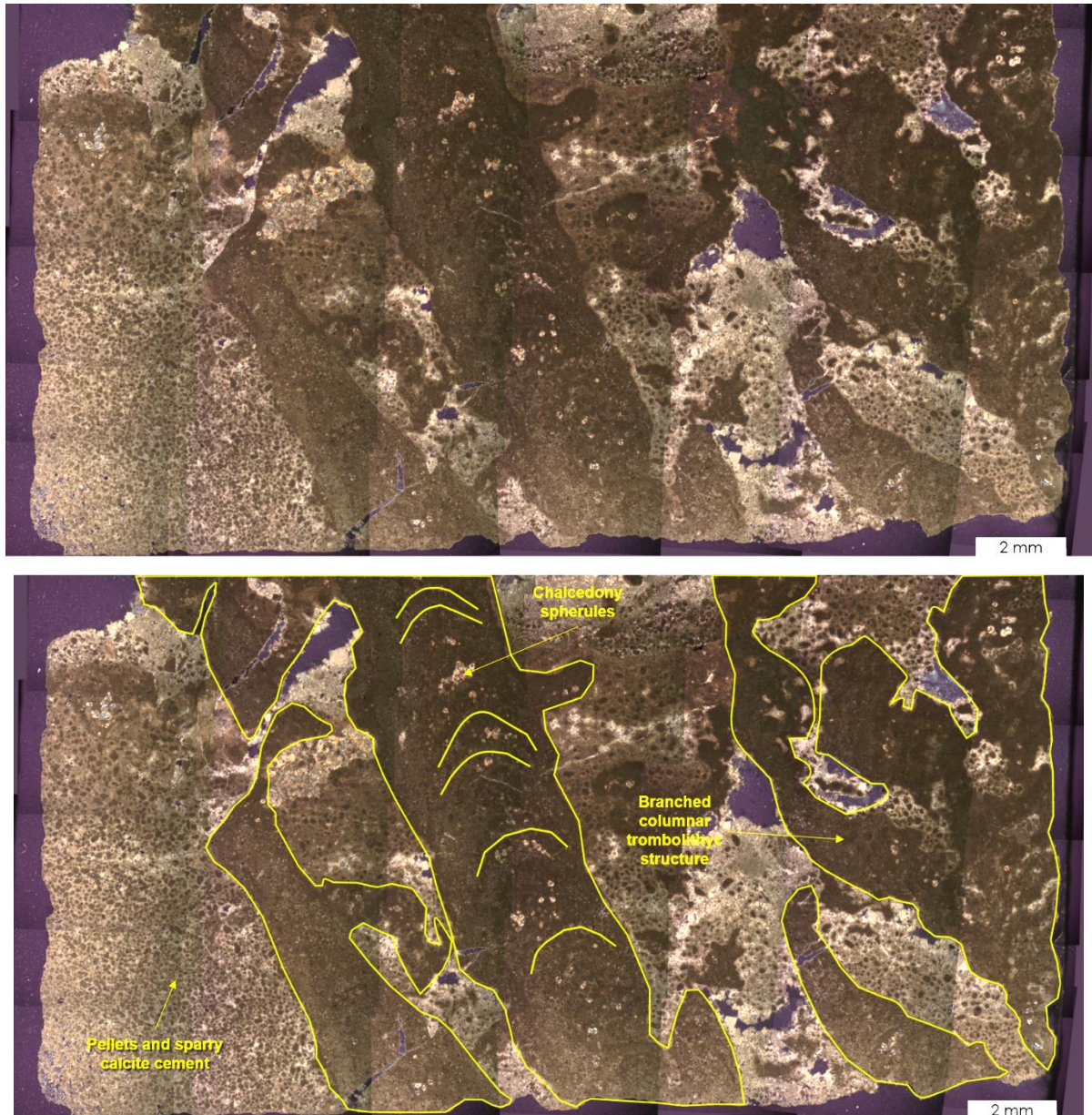


Figure 58. Detail of the IS-ON-2 scan image, highlighting the branched columnar thrombolitic structure with poorly marked laminations.

### 4.3. Routine petrophysics

The routine petrophysical characterization results obtained at LRAP are indicated in Table 9 and Table 10. The grain density values vary between 2.64 and 2.69 g/cc, consistent with the mineralogical composition of the samples analyzed by XRD (calcite has a grain density of 2.7 g/cc), indicating that the samples analyzed by XRD are representative of the plugs' composition.

The six plugs analyzed have very variable porosity and permeability values and can be separated into three categories considering permeability values: very low (< 3 mD), low (3 to 6 mD) and very high (> 1000 mD) permeability.

Table 9. Purbeck plugs routine petrophysical data pre and post-CWI, obtained at LRAP.

	1X		3Y		3Z		6X		6Y		6Z	
	Pre	Post	Pre	Post	Pre	Post	Pre	Post	Pre	Post	Pre	Post
<b>Length (cm)</b>	5.87	5.87	6.06	6.06	5.04	5.04	5.96	5.95	6.19	6.19	6.68	6.68
<b>Diameter (cm)</b>	3.80	3.80	3.76	3.76	3.75	3.75	3.74	3.74	3.77	3.76	3.74	3.74
<b>Total volume (cc)</b>	65.18	65.42	66.95	66.53	55.04	54.72	65.28	65.33	69.16	68.80	73.49	72.48
<b>Grain volume (cc)</b>	57.29	57.30	58.58	58.34	51.41	51.43	61.10	61.08	63.53	63.51	67.89	67.33
<b>Pore volume (cc)</b>	7.89	8.12	8.37	8.19	3.63	3.29	4.18	4.25	5.63	5.28	5.60	5.16
<b>Mass (g)</b>	153.64	153.20	156.60	155.78	136.47	136.17	164.05	163.69	170.56	170.25	181.97	181.58
<b>Grain density (g/cc)</b>	2.68	2.67	2.67	2.67	2.66	2.65	2.69	2.68	2.69	2.68	2.68	2.70
<b>Porosity (%)</b>	12.10	12.45	12.50	12.30	6.60	6.05	6.40	6.50	8.14	7.70	7.62	7.10
<b>Permeability (mD)</b>	1820.53	1719.81	1868.37	1672.11	4.28	73.39	0.26	12.98	0.83	8.78	2.13	6.83
<b>Klinkenberg correction (mD)</b>	1748.76	1650.39	1795.41	1603.78	3.31	64.27	0.19	10.51	0.63	6.99	1.53	5.44

Table 10. Difference in porosity and permeability before and after CWI.

<i>Sample</i>	<b>Porosity (%)</b>			<b>Permeability (mD)</b>		
	<i>Pre-CWI</i>	<i>Post-CWI</i>	$\Delta\Phi$	<i>Pre-CWI</i>	<i>Post-CWI</i>	$\Delta k$
<b>1X</b>	12.10	12.45	+2.9%	1748.76	1650.39	-5.6%
<b>3Y</b>	12.50	12.30	-1.6%	1795.41	1603.78	-10.7%
<b>3Z</b>	6.60	6.05	-8.3%	3.31	64.27	+1844.6%
<b>6X</b>	6.40	6.50	+1.6%	0.19	10.51	+5432.6%
<b>6Y</b>	8.14	7.70	-5.4%	0.63	6.99	+1005.6%
<b>6Z</b>	7.62	7.10	-6.9%	1.53	5.44	+256.2%

Porosity results indicated small porosity variation, with small decreases and small increases. The very low permeability samples (< 1mD) had the highest percentage increases in permeability (considering the injected pore volumes). For samples with low permeability (< 3mD), those in which more pore volumes were injected had a greater increase in permeability, as expected. However, in the high permeability samples (>1500 mD), there was a small decrease in the permeability of both samples.

#### 4.4. NMR results

The results of NMR measurements before and after CWI are gathered in Table 11.

Table 11. Results obtained from NMR measurements

<b>Sample</b>	<b>Pre-CWI</b>		<b>Post-CWI</b>		$\Delta\Phi$
	<i>Saturation index (%)</i>	<i>NMR porosity (%)</i>	<i>Saturation index (%)</i>	<i>NMR porosity (%)</i>	
1X	84.09	12.11	89.85	11.26	-7.0%
3Y	74.24	11.65	86.57	11.54	-1.0%
3Z	82.72	6.50	93.15	6.93	6.5%
6X	94.85	7.59	96.46	7.13	-6.1%
6Y	91.22	8.53	94.63	8.14	-4.6%
6Z	93.9	7.95	95.50	7.65	-3.8%

The saturation values were satisfactory for plugs 6X, 6Y, and 6Z and low for 1X, 3Y and 3Z. The low values of saturation are likely due to the large number of vugular pores, which

CHAPTER 4. RESULTS AND DISCUSSION

can decrease the effectiveness of the saturation process because they fail to retain the saturation fluid (DE LUNA *et al.*, 2016).

The porosity values obtained by helium porosimeter and those obtained by NMR are very similar, with high coefficients of determination (Figure 59).

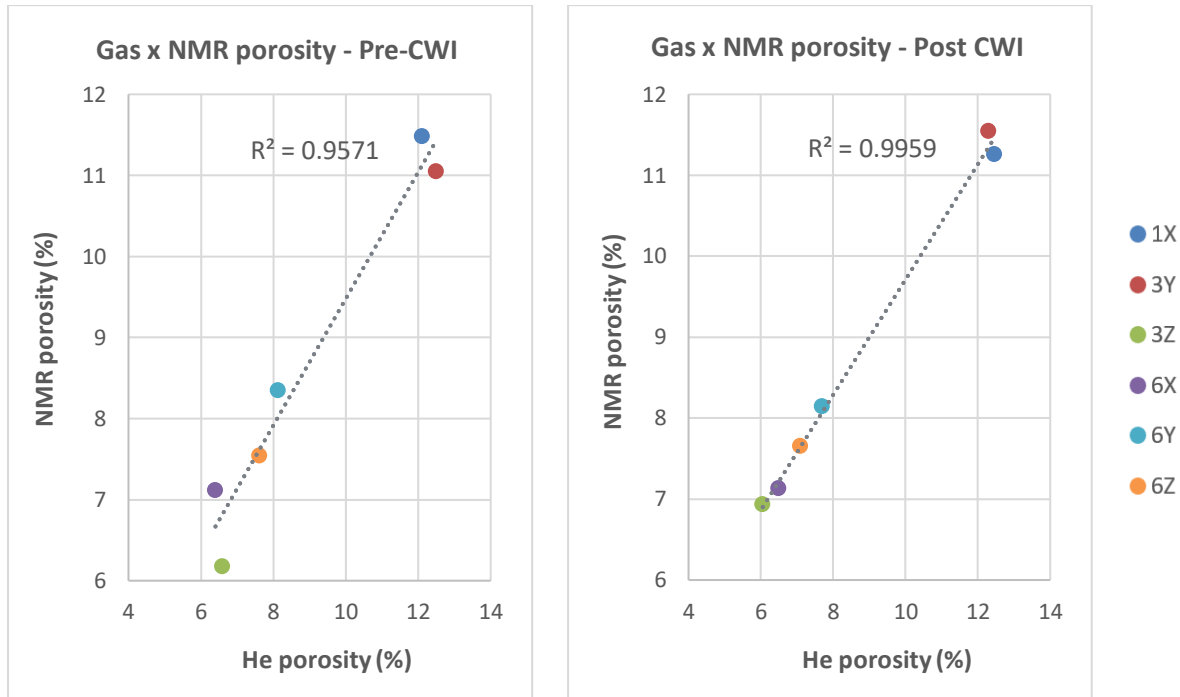


Figure 59. Correlation between helium porosity and NMR porosity (before and after CWI).

The  $T_2$  distribution results indicate that the plugs are very heterogeneous, having pore size distributions varying from bimodal to polymodal (Figure 60 and Figure 61). The figures below gather the  $T_2$  distribution of incremental porosity before and after carbonated water injection.

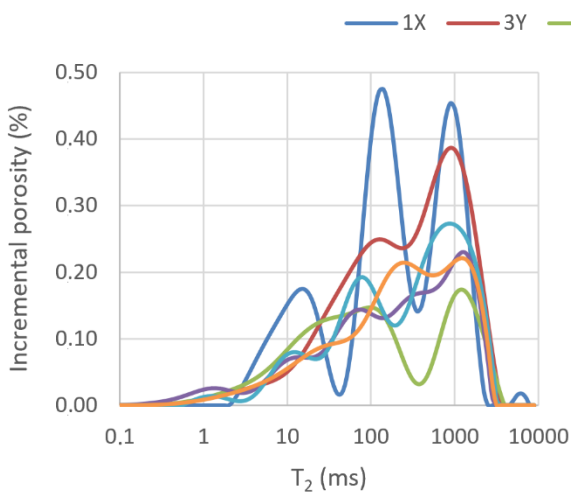


Figure 60. NMR  $T_2$  distribution before CWI.

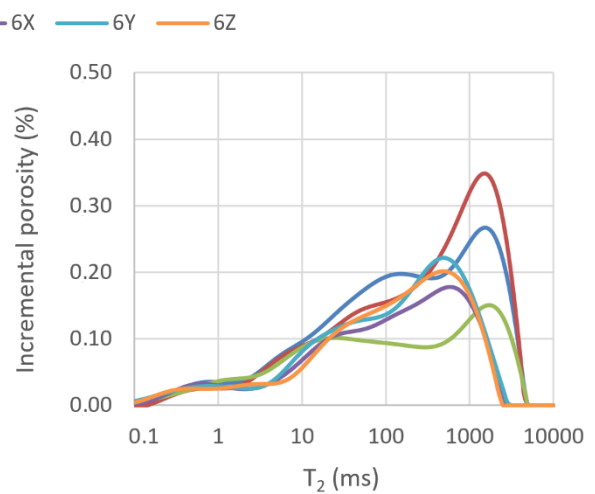


Figure 61. NMR  $T_2$  distribution after CWI.

CHAPTER 4. RESULTS AND DISCUSSION

The figures below gather graphs of incremental and accumulated porosity **before** CW injection for each sample.

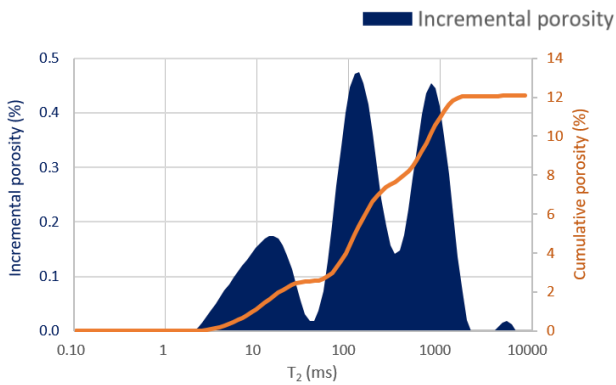


Figure 62. Sample 1X incremental and cumulative porosity before CWI.

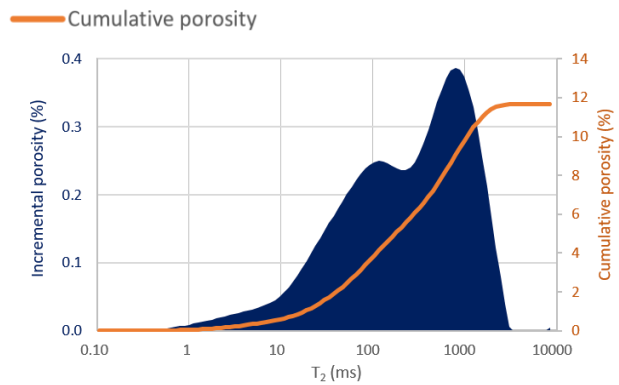


Figure 63. Sample 3Y incremental and cumulative porosity before CWI.

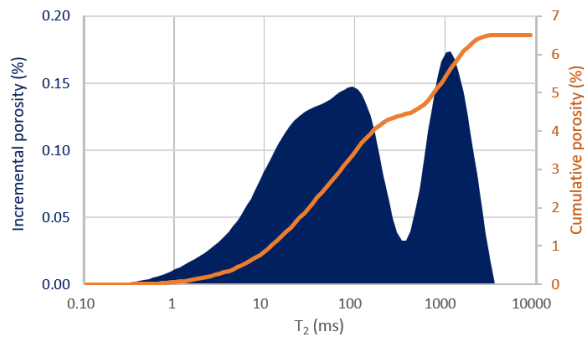


Figure 64. Sample 3Z incremental and cumulative porosity before CWI.

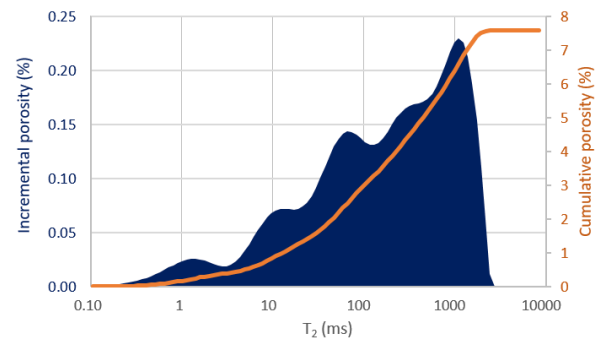


Figure 65. Sample 6X incremental and cumulative porosity before CWI.

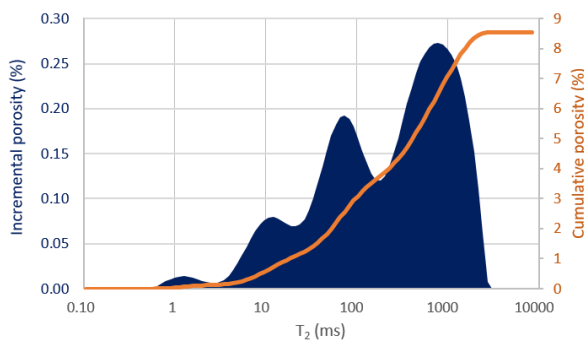


Figure 66. Sample 6Y incremental and cumulative porosity before CWI.

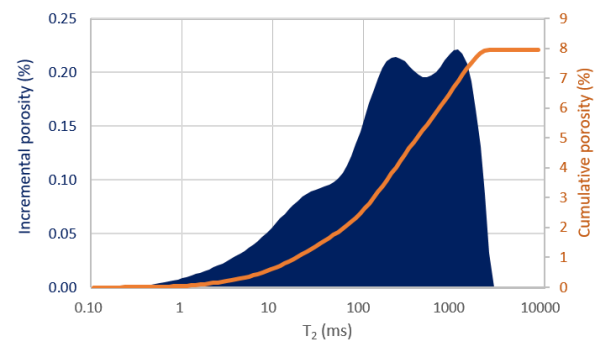


Figure 67. Sample 6Z incremental and cumulative porosity before CWI.



## CHAPTER 4. RESULTS AND DISCUSSION

The figures below gather graphs of incremental and accumulated porosity **after** CW injection for each sample.

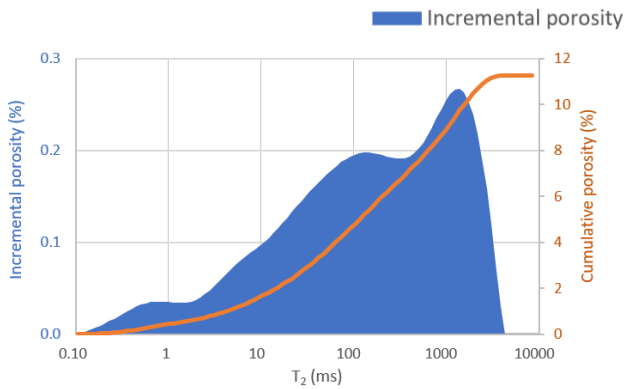


Figure 68. Sample 1X incremental and cumulative porosity after CWI.

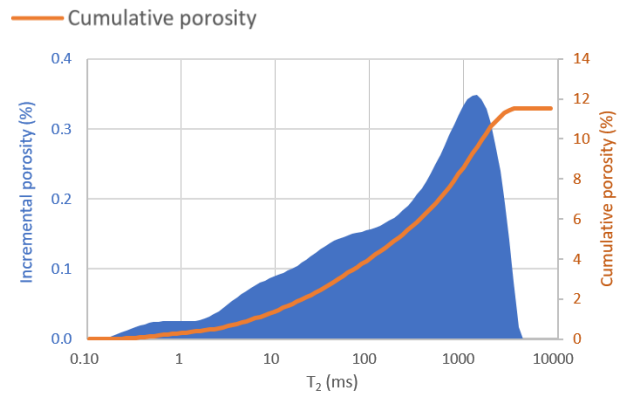


Figure 69. Sample 3Y incremental and cumulative porosity after CWI.

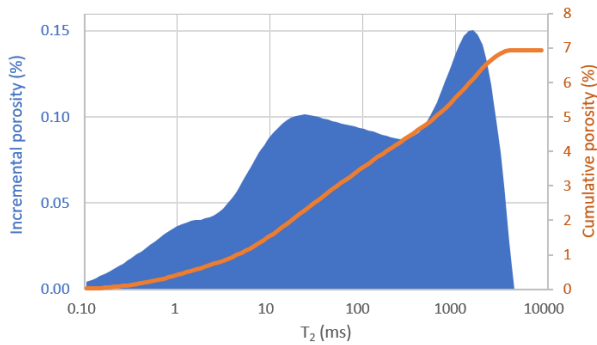


Figure 70. Sample 3Z incremental and cumulative porosity after CWI.

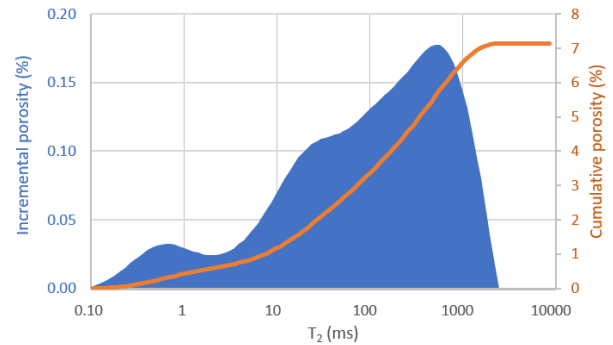


Figure 71. Sample 6X incremental and cumulative porosity after CWI.

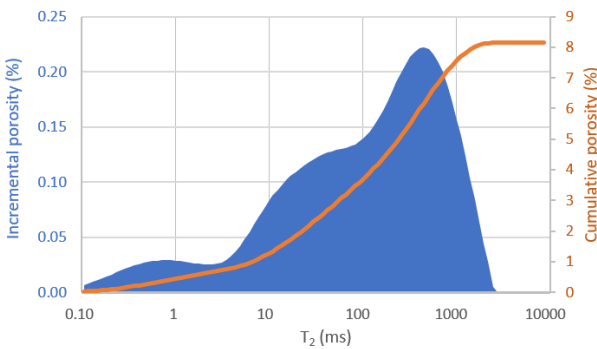


Figure 72. Sample 6Y incremental and cumulative porosity after CWI.

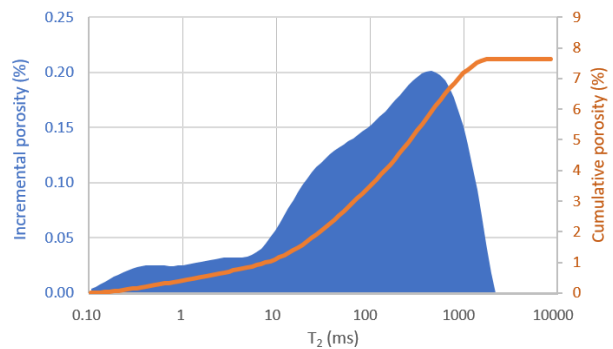


Figure 73. Sample 6Z incremental and cumulative porosity after CWI.

## CHAPTER 4. RESULTS AND DISCUSSION

The NMR incremental porosity graphs before and after CW injection were integrated using the cumulative porosity curves and were gathered in the images below.

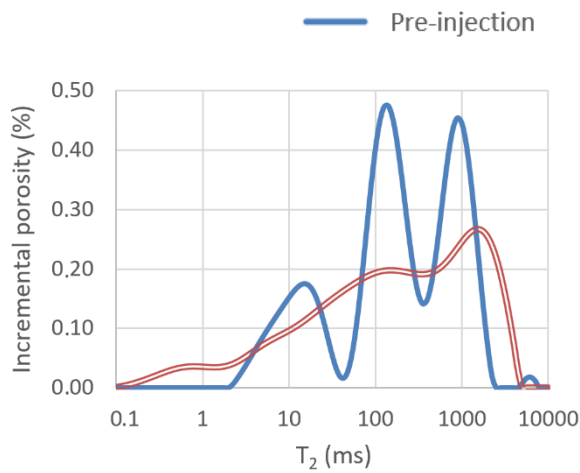


Figure 74. Sample 1X pre and post-CWI incremental porosity.

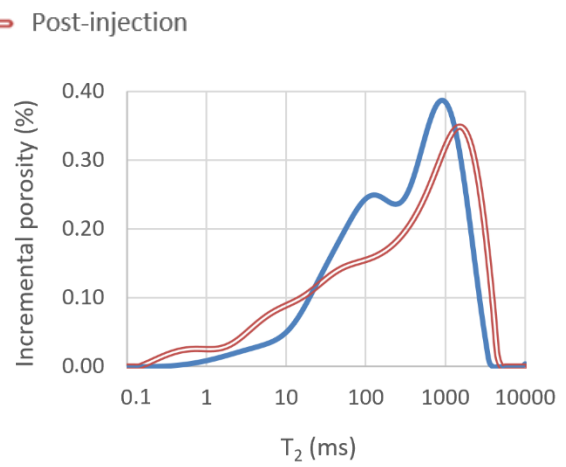


Figure 75. Sample 3Y pre and post-CWI incremental porosity.

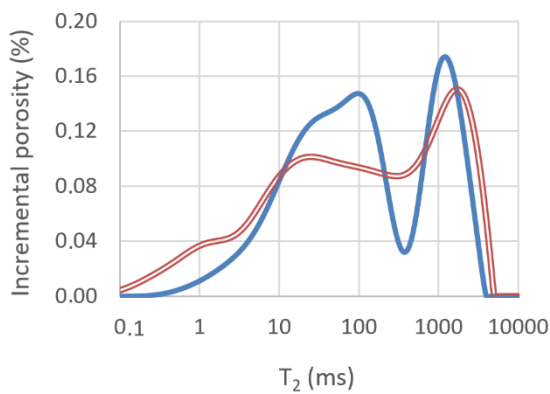


Figure 76. Sample 3Z pre and post-CWI incremental porosity.

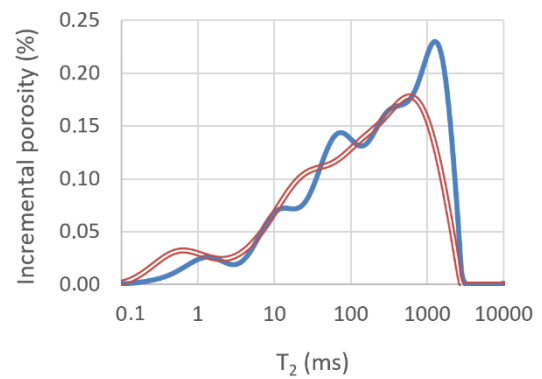


Figure 77. Sample 6X pre and post-CWI incremental porosity.

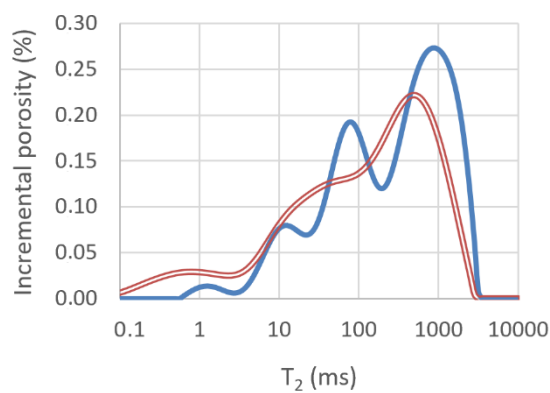


Figure 78. Sample 6Y pre and post-CWI incremental porosity.

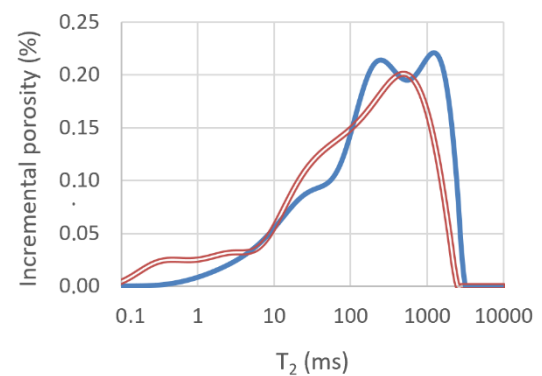


Figure 79. Sample 6Z pre and post-CWI incremental porosity.

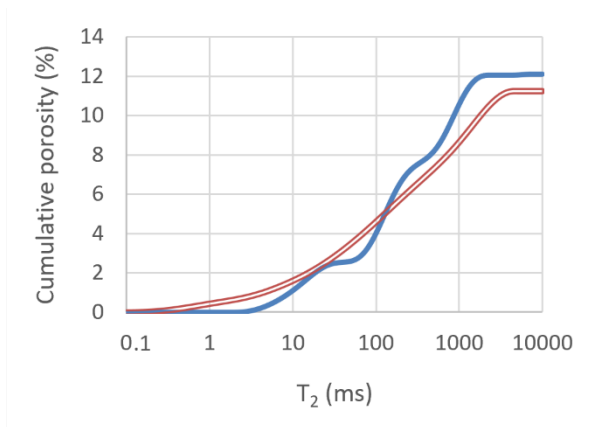


Figure 80. Sample 1X pre and post-CWI cumulative porosity.

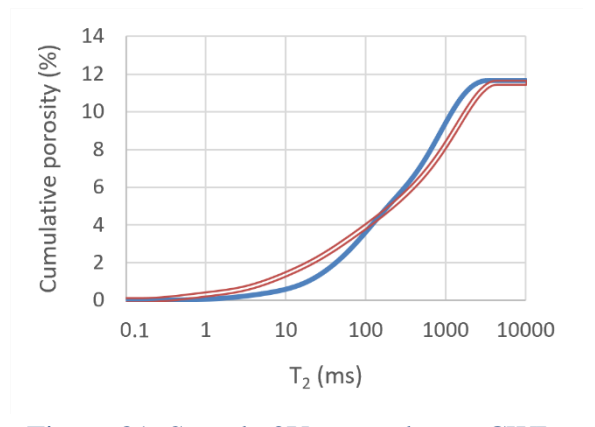


Figure 81. Sample 3Y pre and post-CWI cumulative porosity.

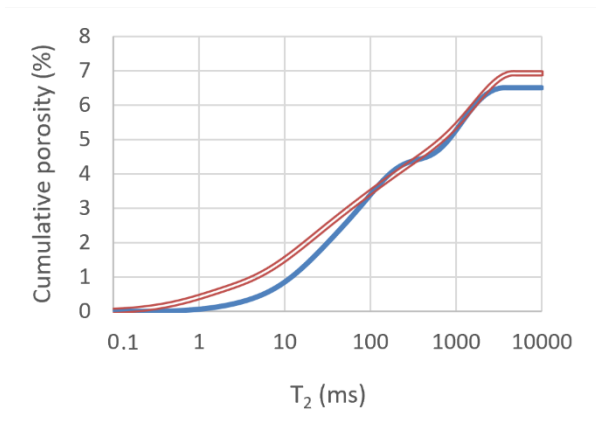


Figure 82. Sample 3Z pre and post-CWI cumulative porosity.

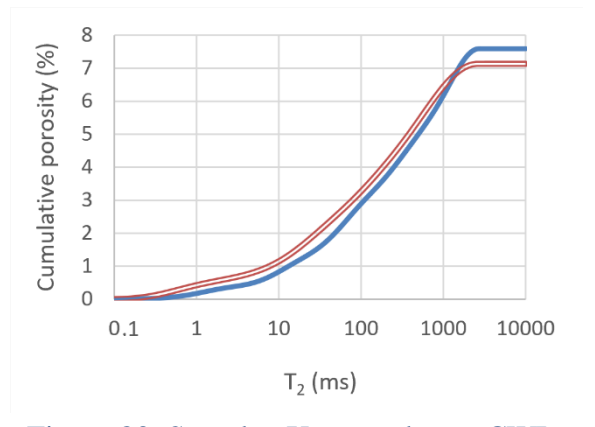


Figure 83. Sample 6X pre and post-CWI cumulative porosity.

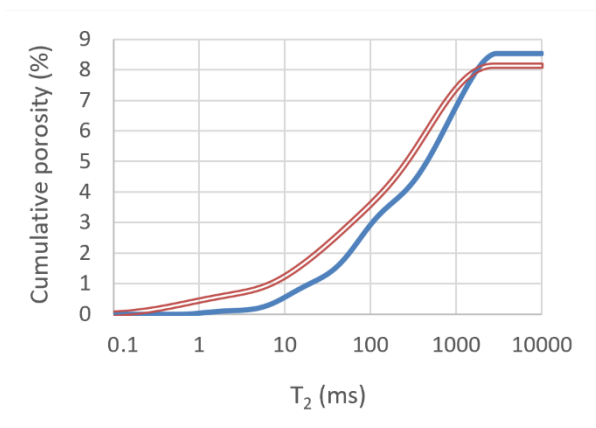


Figure 84. Sample 6Y pre and post-CWI cumulative porosity.

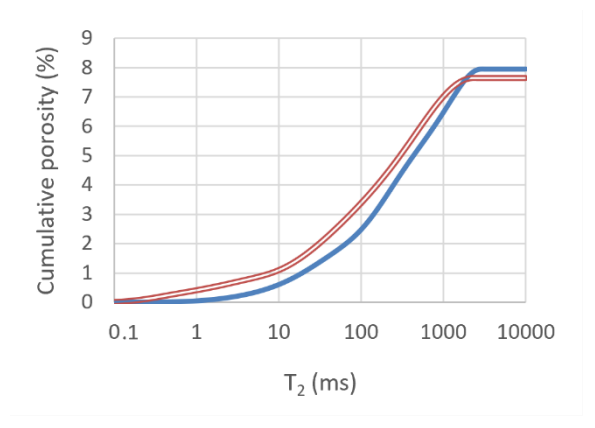


Figure 85. Sample 6Z pre and post-CWI cumulative porosity.

NMR analyzes before and after the injection had to be carried out in different laboratories using different equipment, which makes a direct comparison between the results difficult. For all samples, the differences observed in the incremental porosity curves

can be due to the differences in equipment, data processing (non-identical inversion/regulation method), and non-identical saturation and temperature condition. The following interpretations are made considering that the differences are, at least in part, a consequence of the CW injection.

All samples, especially 1X (Figure 74), 3Z (Figure 76), and 6Y (Figure 78) showed peak smoothing, reducing the marking of the limits between them, which may indicate a uniformity of pore sizes due to the CW injection. The largest post-injection peaks of 1X (Figure 74), 3Y (Figure 75), and 3Z samples show a slight shift to the right compared to pre-injection curves, which may indicate an increase in the largest pores size. In samples 6X (Figure 77), 6Y (Figure 78), and 6Z (Figure 79), on the other hand, there is a slight shift to the left, which may indicate a decrease in the size of the largest pores.

In all samples there seems to have been an increase in microporosity; in samples 1X, 3Y, and 3Z (the most heterogeneous ones) there seems to have been a decrease in mesoporosity, and in all samples except for 3Z there seems to have been a decrease in macroporosity.

#### 4.5. Micro-CT results

The images of the plugs obtained by micro-CT are gathered in the following images. For each plug, a top and bottom slice and a cross-section were put together. The fluids injection direction (from top to bottom) was also indicated.

The light parts of the images indicate the rock matrix, and the dark parts indicate the porous space.

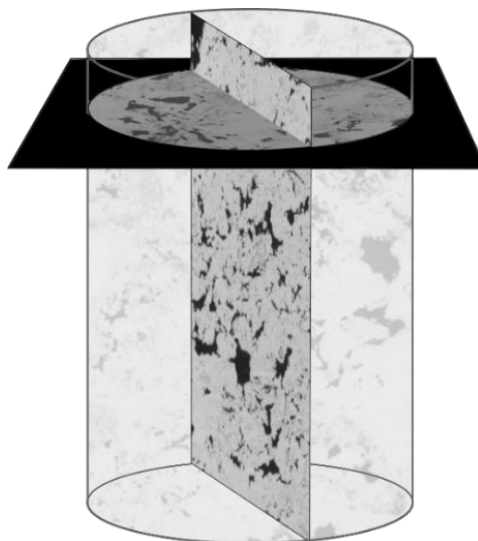


Figure 86. Schematic drawing of the images obtained by Micro-CT in relation to plugs.

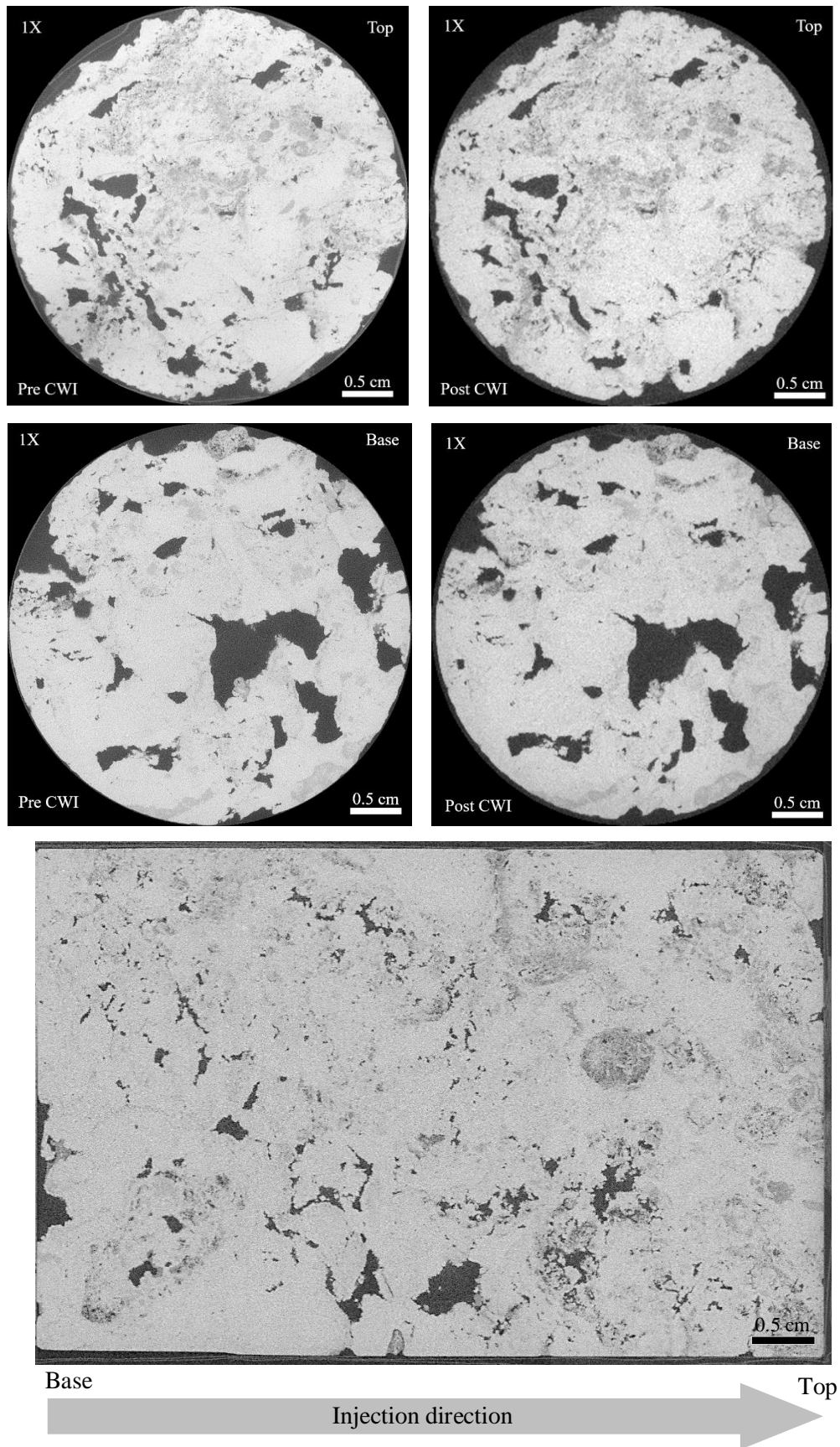


Figure 87. Sample 1X micro-CT images.  
Upper images: plug's top and bottom face, pre and post-CWI;  
Bottom image: plug's cross-section pre-CWI.

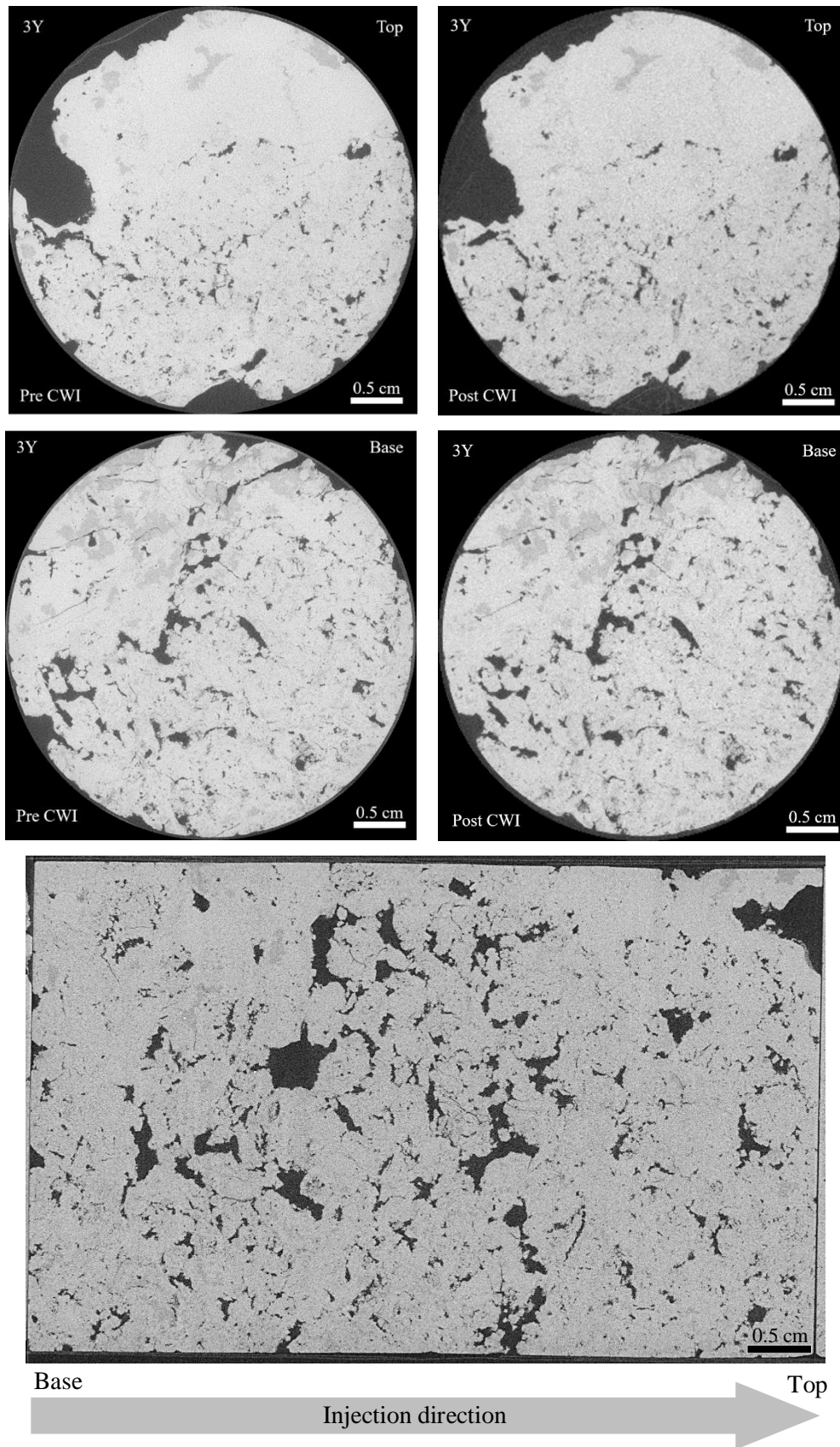


Figure 88. Sample 3Y micro-CT images.  
Upper images: plug's top and bottom face, pre and post-CWI;  
Bottom image: plug's cross-section pre-CWI.

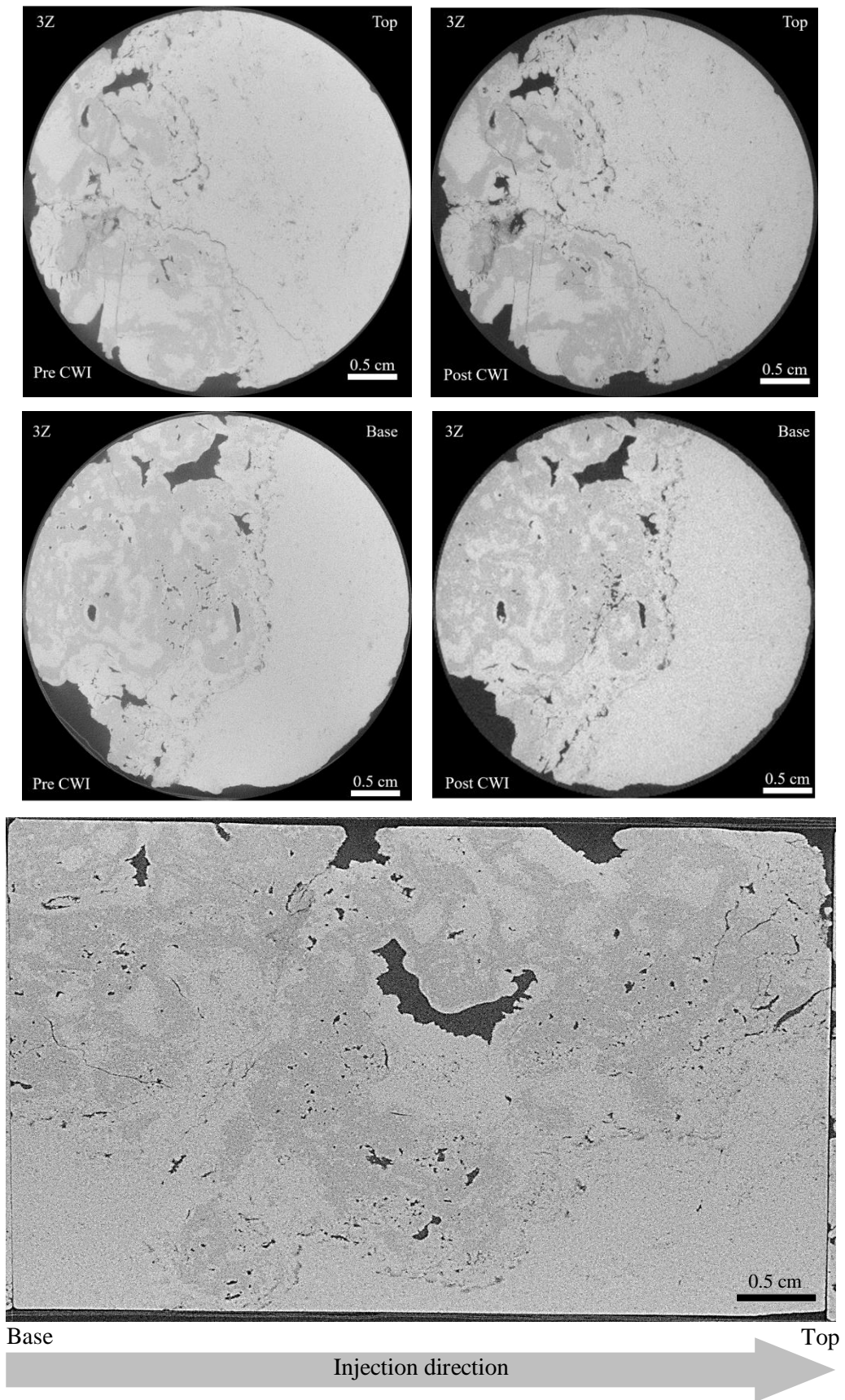


Figure 89. Sample 3Z micro-CT images.  
Upper images: plug's top and bottom face, pre and post-CWI;  
Bottom image: plug's cross-section pre-CWI.

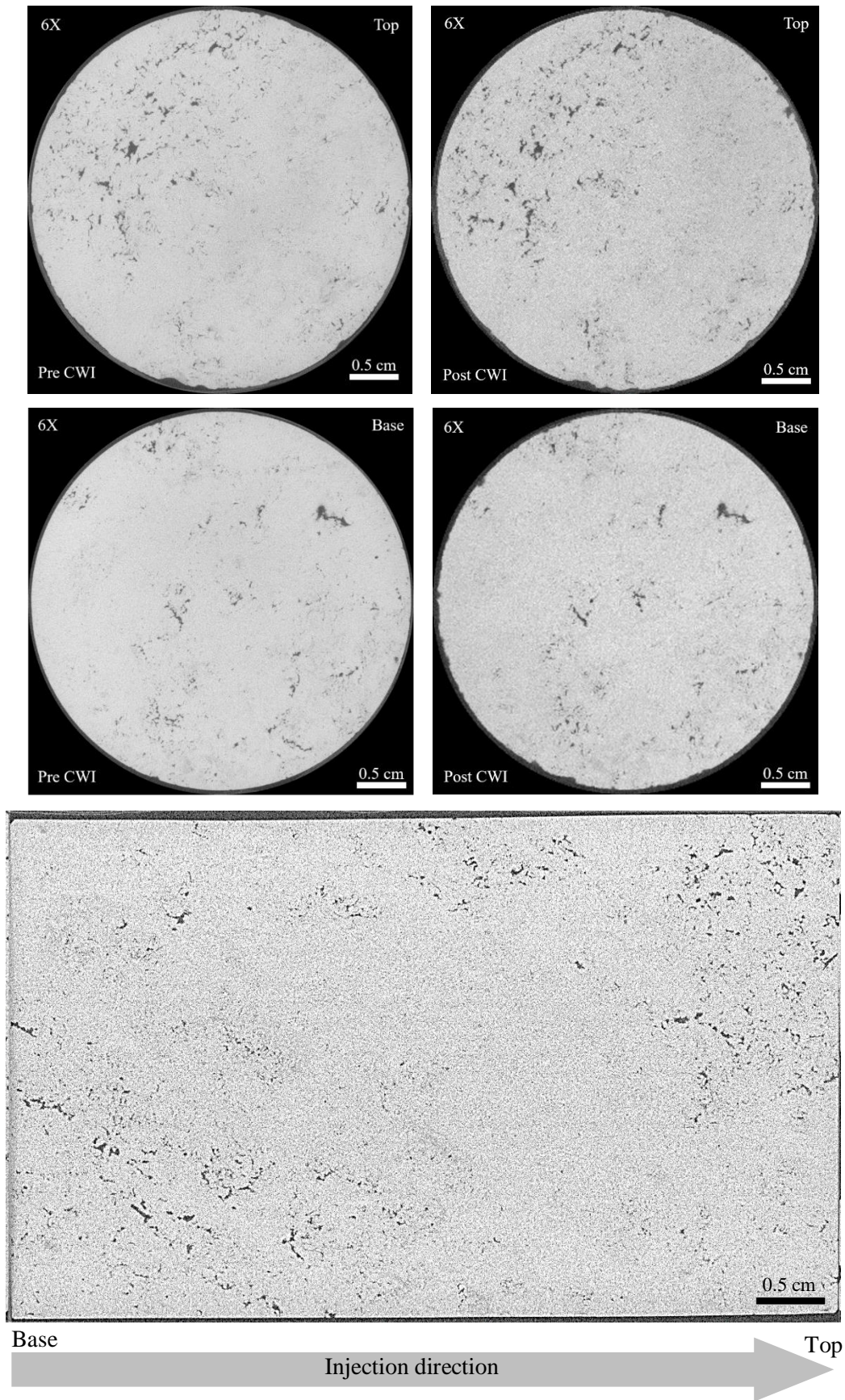


Figure 90. Sample 6X micro-CT images.  
Upper images: plug's top and bottom face, pre and post-CWI;  
Bottom image: plug's cross-section pre-CWI.



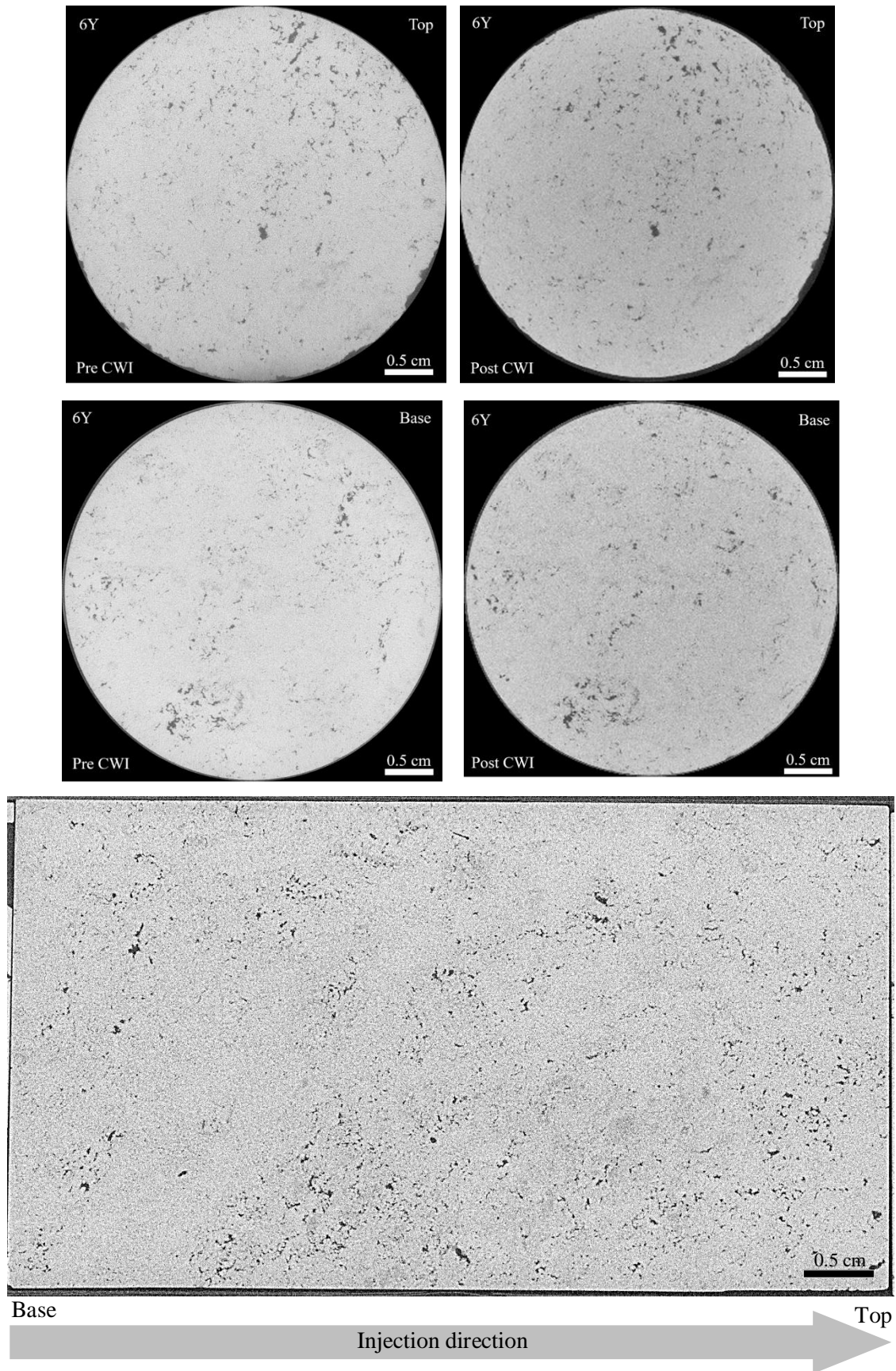


Figure 91. Sample 6Y micro-CT images.  
Upper images: plug's top and bottom face, pre-CWI;  
Bottom image: plug's cross-section pre-CWI.

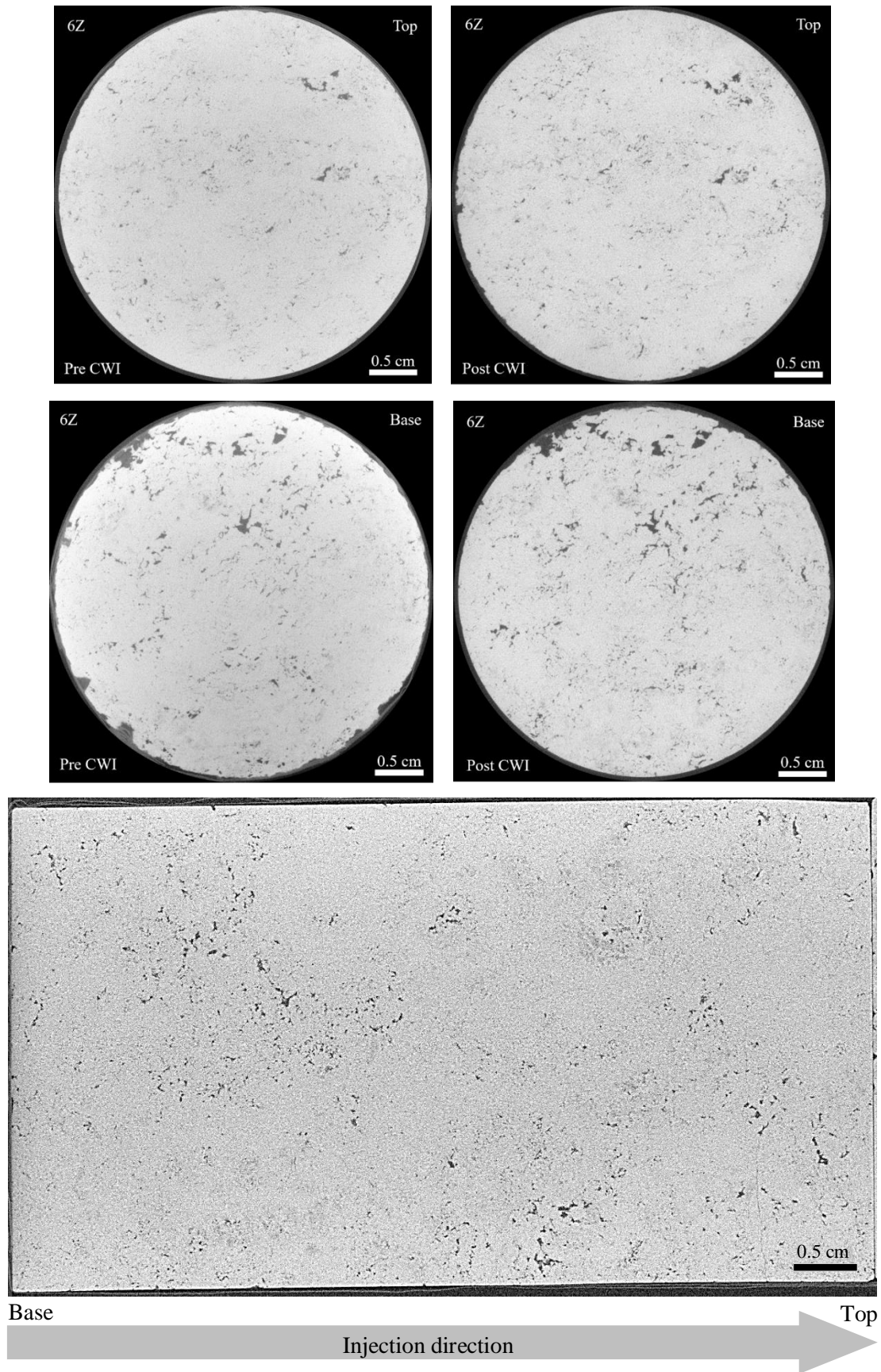


Figure 92. Sample 6Z micro-CT images.  
Upper images: plug's top and bottom face, pre and post-CWI;  
Bottom image: plug's cross-section pre-CWI.

## CHAPTER 4. RESULTS AND DISCUSSION

Samples 1X and 3Y are highly vugular and heterogeneous, with several fractures, not presenting a layering or preferential orientation. Sample 3Z presents the contact between vuggy/microbial and laminated/massive facies. Samples 6X, 6Y, and 6Z represent the laminated/massive facies, with light lamination on the first two.

The following graphs gather the samples' micro-CT porosities along the length, pre and post-CW injection and the difference between the two ( $\Delta$ CT porosity = post-CWI porosity - pre-CWI porosity).

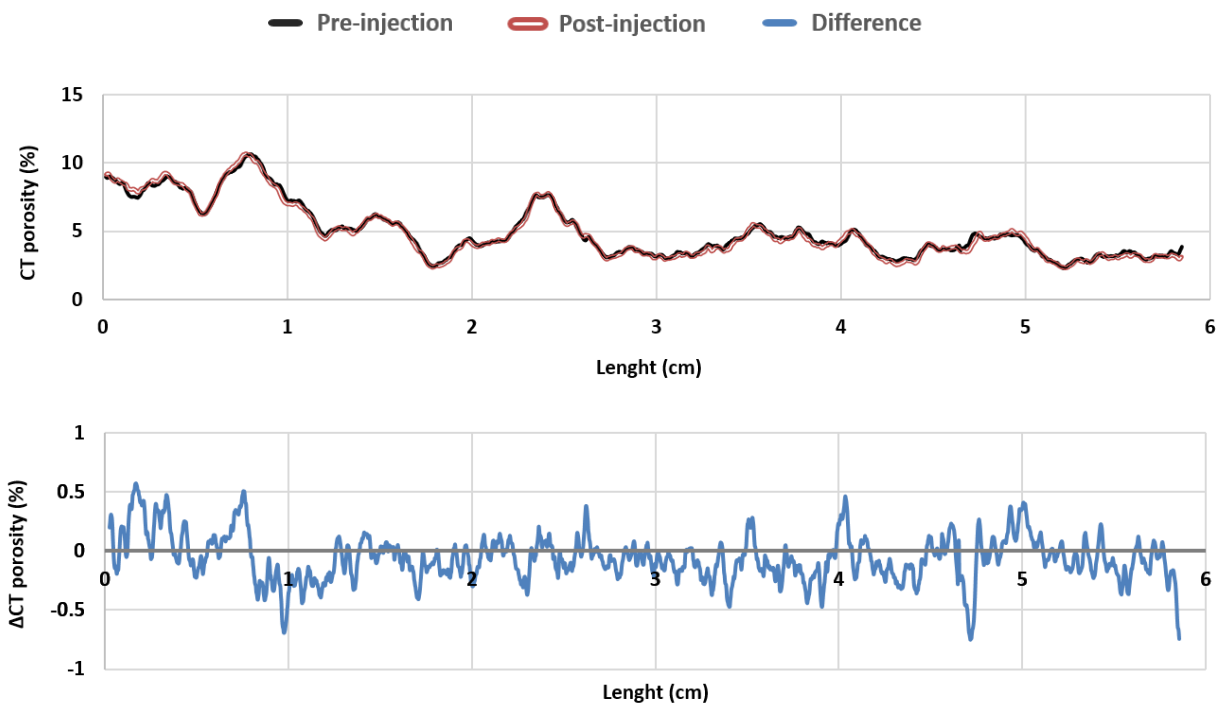


Figure 93. 1X micro-CT porosity variation along the sample's length.

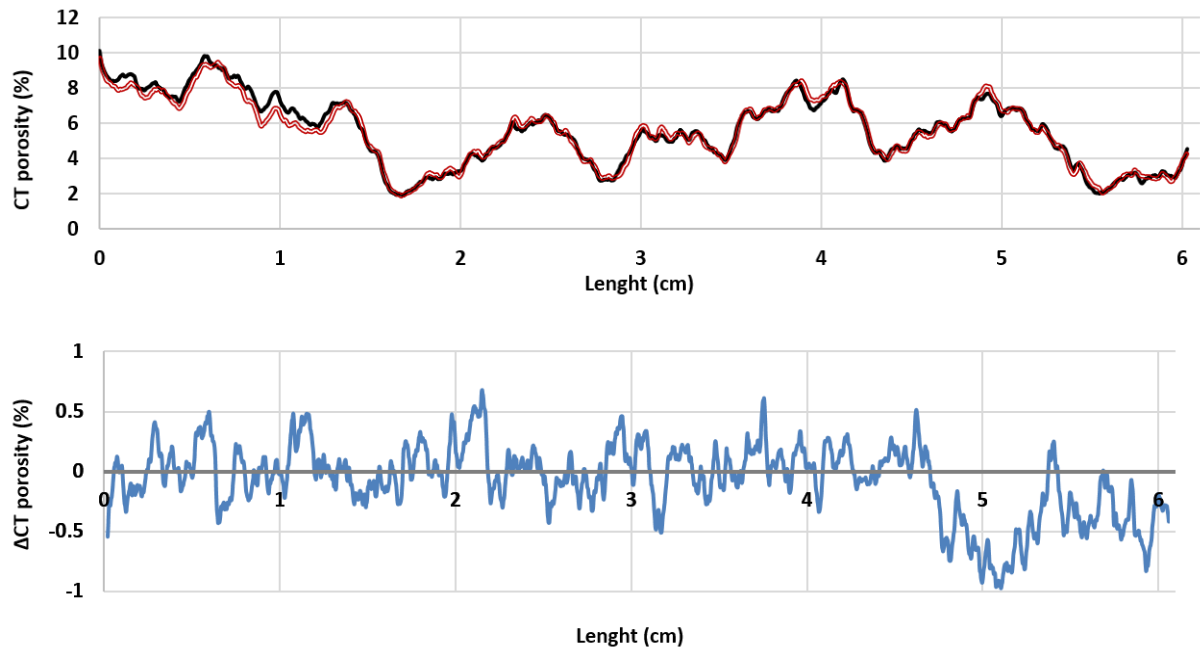


Figure 94. 3Y micro-CT porosity variation along the sample's length.

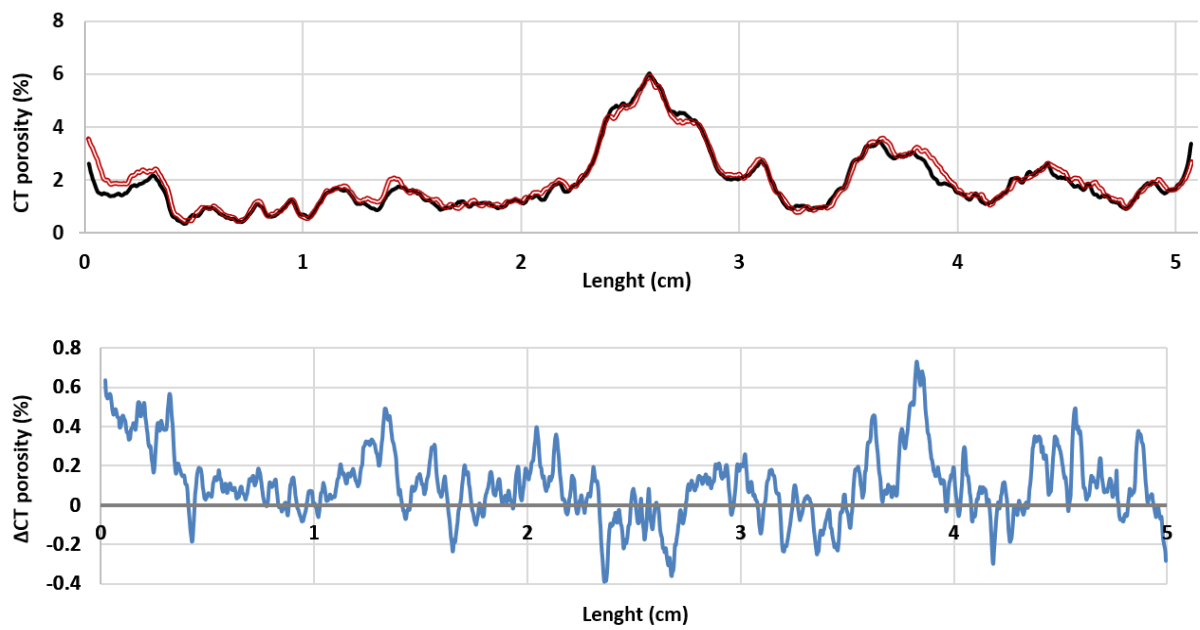


Figure 95. 3Z micro-CT porosity variation along the sample's length.

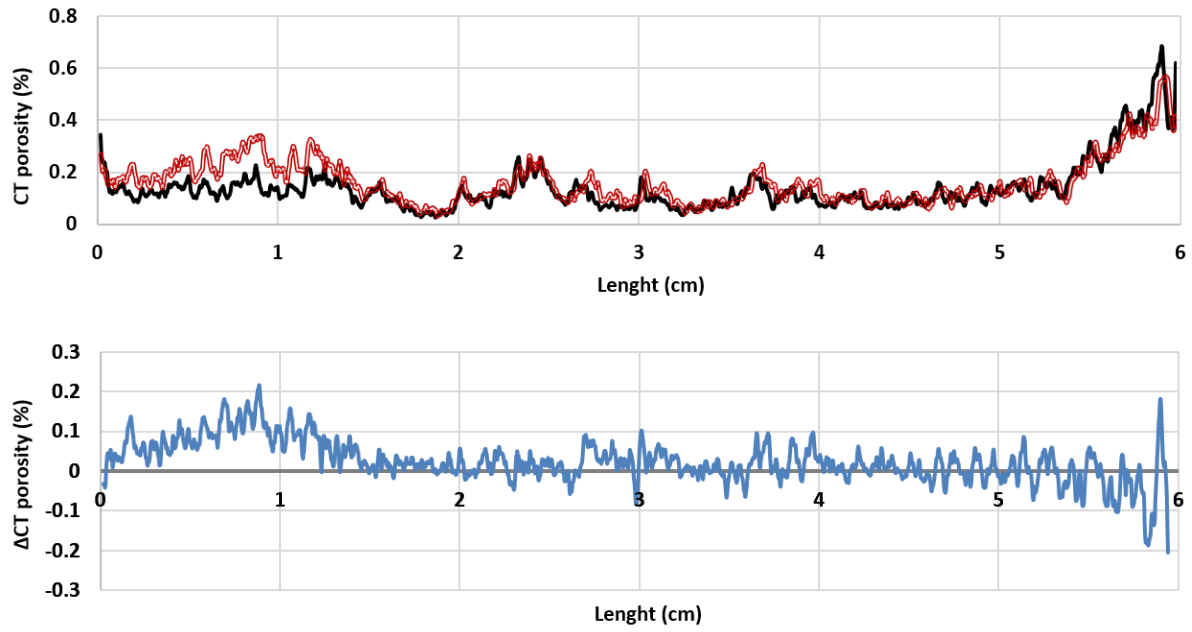


Figure 96. 6X micro-CT porosity variation along the sample's length.

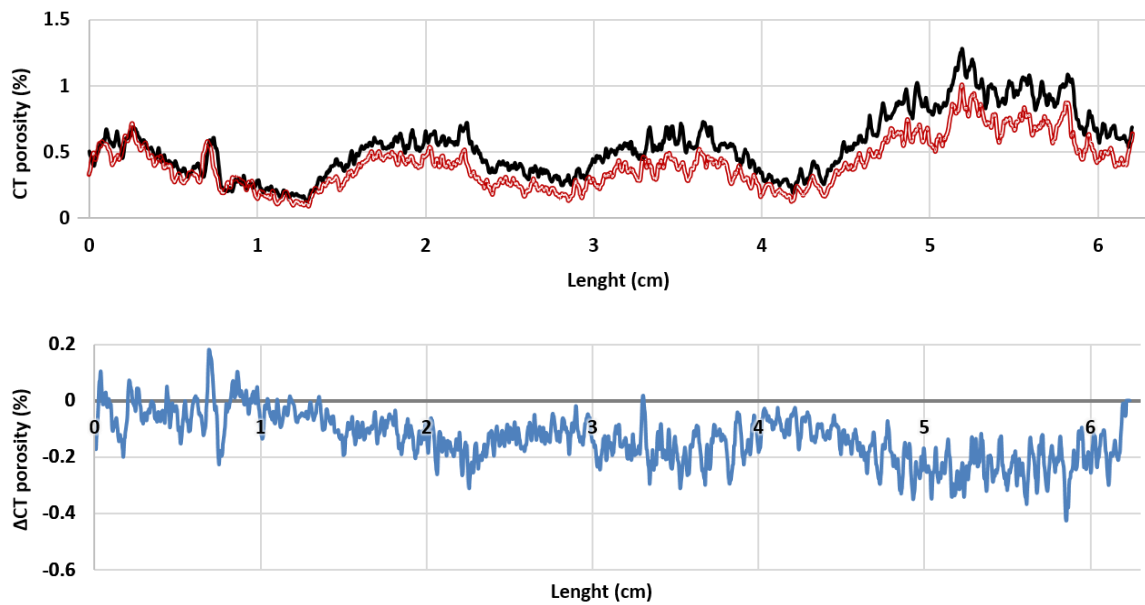


Figure 97. 6Y micro-CT porosity variation along the sample's length.

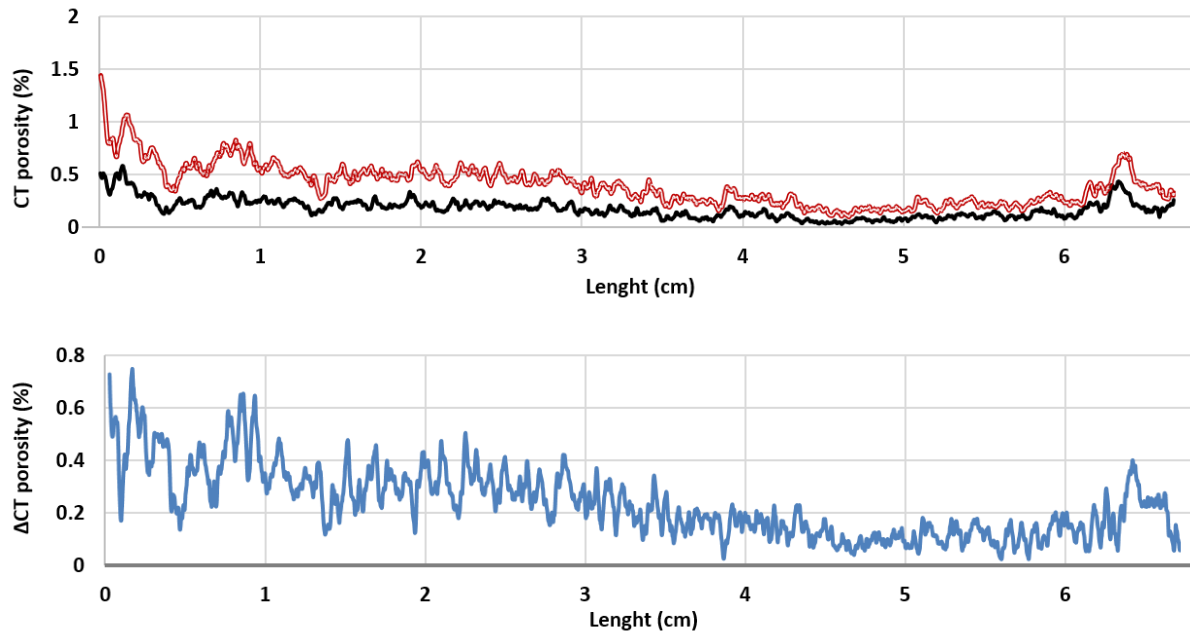


Figure 98. 6Z micro-CT porosity variation along the sample’s length.

Samples 6X, 6Y, and 6Z – the non-vugular samples – presented a trend of decrease in porosity towards the CW outlet face. 1X, 3Y, and 3Z – the vugular samples – presented a more homogeneous porosity variation along the samples’ length. 3Y exhibited a sharp decrease in porosity close to the outlet face.

Table 12 indicates the average micro-CT porosity of each plug. For all, the results indicate very little variation pre- and post-CWI.

Table 12. Average samples’ micro-CT porosity before and after CWI.

Sample	CT porosity (%)		
	Pre-CWI	Post-CWI	$\Delta\phi$
6Y	0.55	0.41	- 0.14
6X	0.14	0.16	+ 0.02
6Z	0.18	0.40	+ 0.22
3Z	1.87	1.99	+ 0.12
1X	4.95	4.88	- 0.07
3Y	5.60	5.53	- 0.07

Figures Figure 99 and Figure 100 compare pre- and post-CWI images of the plug 1X's base, closer to the inlet face. The images exemplify what also happened in the other plugs. Dissolution and precipitation occurred, including in different parts of the same vugular pores, with dissolution in parts with more accelerated CW flow (where the pore narrows) and precipitation in parts with decelerated flow due to the increase in pore size, as observed by KHAN *et al.* (2019).

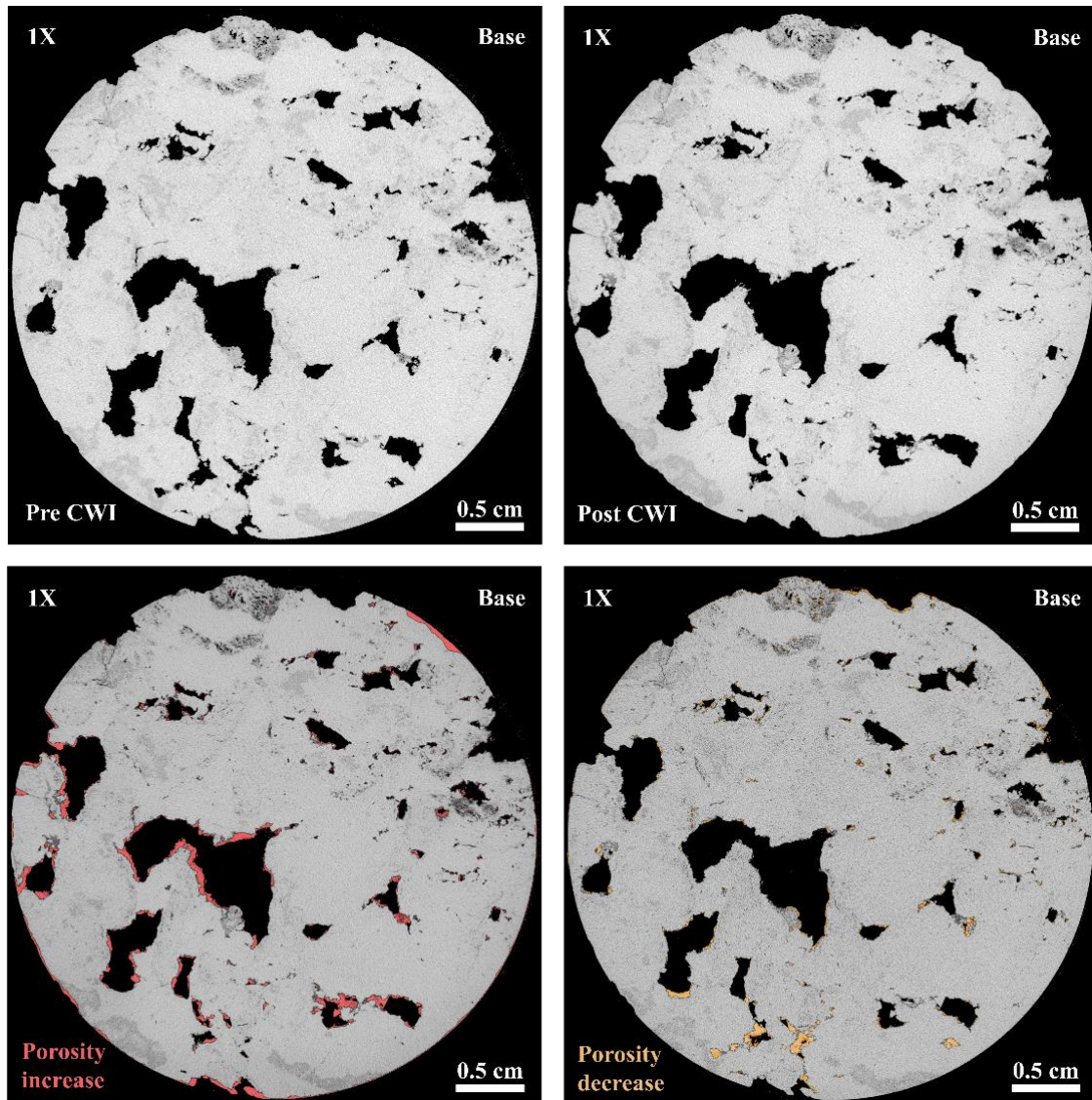


Figure 99. Images from plug 1X's base, closer to the inlet face. Top left: pre-CWI; Top right: post-CWI; Bottom left: the post-CWI image above and pre-CWI image below in red (material lost), highlighting porosity increase; Bottom right: the pre-CWI image above and post-CWI image below in yellow (material gained), highlighting porosity decrease.

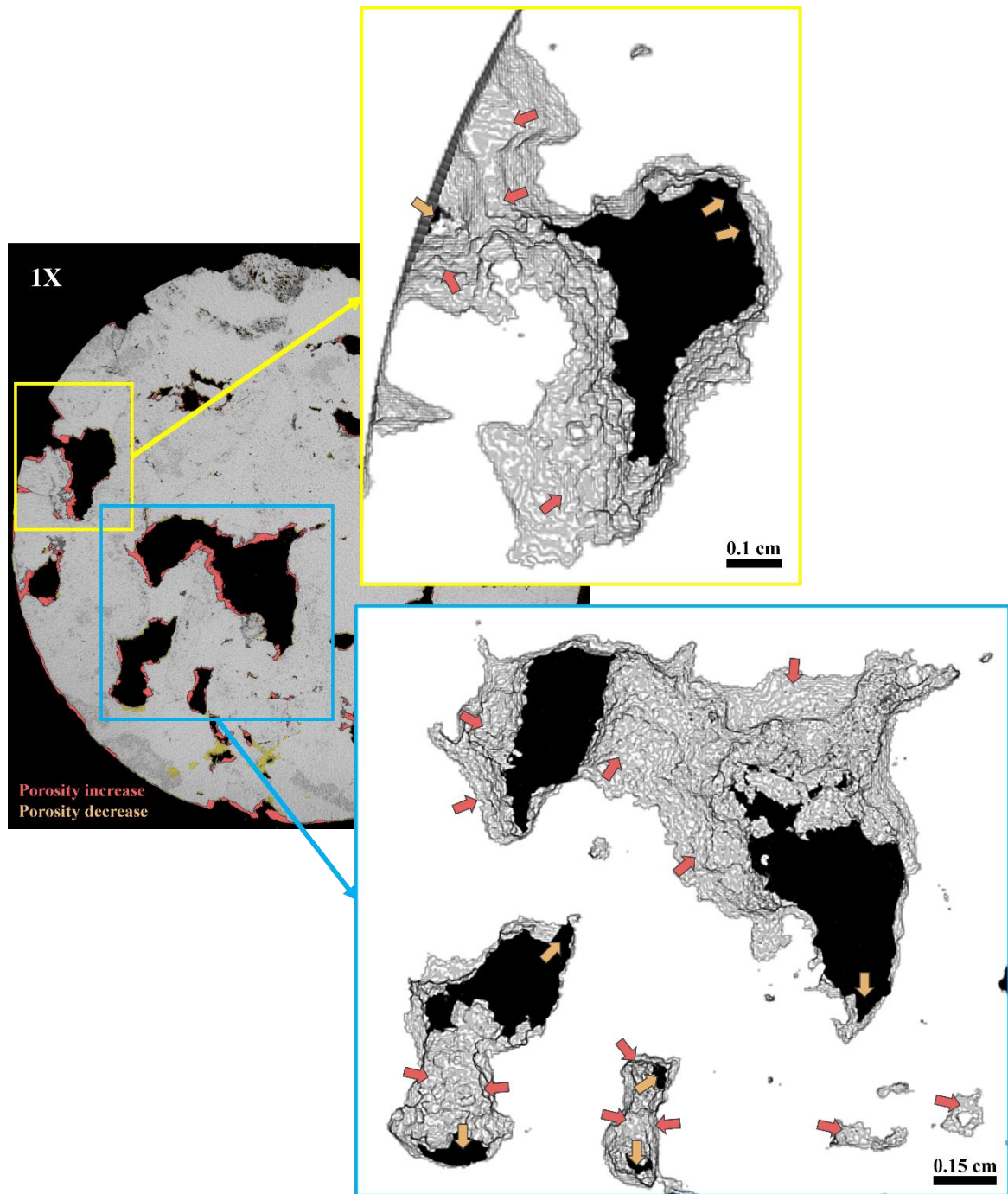


Figure 100. 3D image of pores from plug 1X's 15 cm from its base, including 60 slices (16 below the slice in Fig. 8 and 43 slices above it). The magenta arrows indicate the main areas where dissolution occurs due to pore narrowing and the yellow arrows indicate precipitation areas due to an increase in pore size, which causes flow deceleration.



## 4.6. Carbonated Water Injection results

The gas permeability values before injection, DSW permeability calculated from the differential pressure after stabilization, porous volume, and pore volumes injected in each sample are gathered in Table 13.

Table 13. Gas and DSW permeability and pore volume for each sample before CWI and pore volumes of CW injected in each sample.

Sample	N <sub>2</sub> permeability – Klinkenberg effect corrected (mD)	DSW permeability (mD)	Pore volume (cc)	Pore volumes of CSW injected
6Y	0.63	0.42	5.63	5
6X	0.19	0.18	4.18	8
6Z	1.53	1.67	5.60	5
3Z	3.31	2.2	3.63	10
1X	1748.76	~2000	7.89	5
3Y	1795.41	~250	8.37	10

The permeability values to nitrogen (after correction of the Klinkenberg effect) and to DSW were very similar in 5 of 6 samples. The difference in the 3Y sample may have been caused by the thread seal tape pellets placed in its vugs to avoid causing a tear in the plastic sleeve in which the sample was involved (Figure 101).

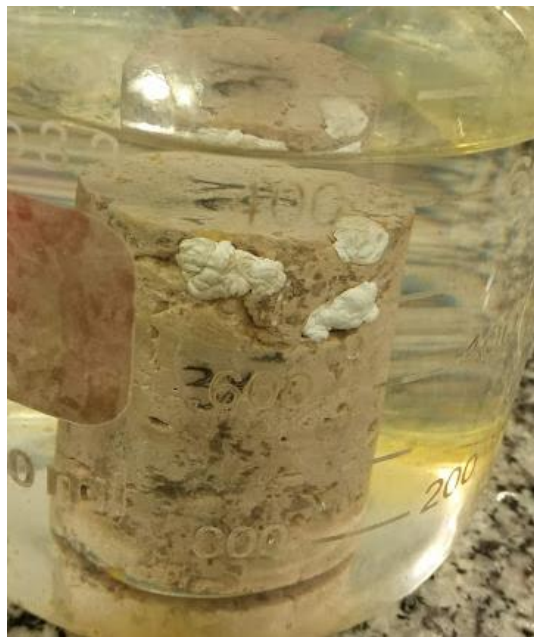


Figure 101. Thread seal tape pellets placed in the vugs of sample 3Y.

CHAPTER 4. RESULTS AND DISCUSSION

Following are gathered the graphs of differential pressure variation through injection time, obtained from data collected by the LabVIEW 2016 software, and permeability variation through injection time, generated from the calculation of permeability from the differential pressure using Darcy's Law (Equation 5). In each graph are also indicated the time intervals for collecting effluents from the DSW injection, each pore volume of the CWS injection effluents, and the samples of CIW effluent at the end of the injection analysis.

Table 14 brings together the variations in pressure and permeability during carbonated water injection. These values are covered in more detail in the following charts.

Table 14. Pressure and permeability values in the beginning and of CW injection and permeability increase for each sample.

Sample	CWI onset		CWI end		$\Delta k$
	Pressure (psi)	k (mD)	Pressure (psi)	k (mD)	
6Y	340	0.41	20	6.90	+1600%
6X	830	0.16	14	9.61	+5829%
6Z	97	1.57	37	4.13	+162%
3Z	54	2.13	3.5	32.83	+1443%
1X	Uncertain				
3Y	0.6	227.26	0.45	303.01	+33%

**Samples 6Y and 6X**

Samples 6Y and 6X presented a quick pressure drop after the CW injection started, dropping from a  $\Delta P$  of 340 psi to 20 psi in 28 minutes in sample 6Y (Figure 102) and from 830 psi to 100 psi in 21 minutes and to 14 psi after another 32 minutes in sample 6X (Figure 104). Permeability increased from 0.4 to 6.9 psi in sample 6Y (Figure 103) and from 0.16 to 9.6 in sample 6X (Figure 105).

Gas permeability results indicated a similar increase in permeability for both samples (Table 10).

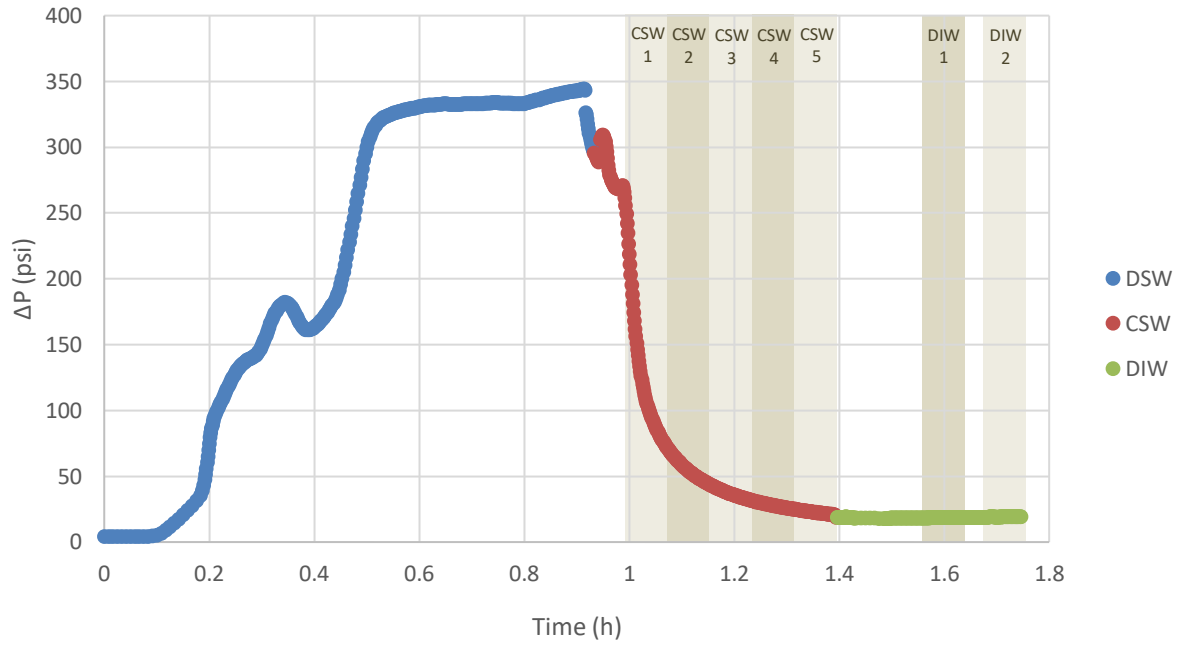


Figure 102. Differential pressure variation through injection time in sample 6Y.

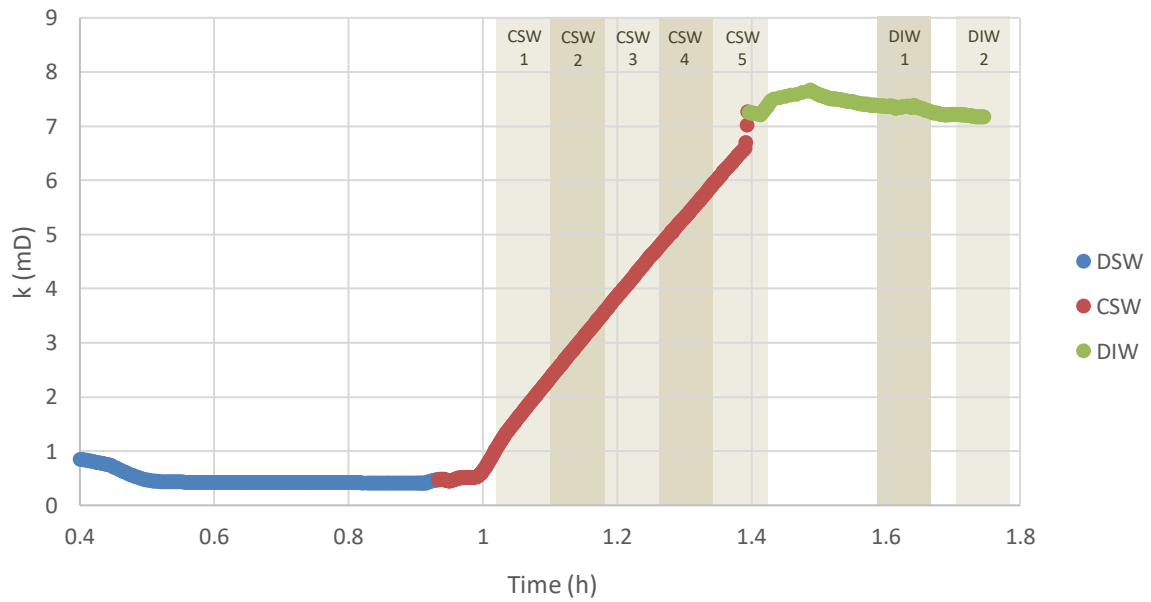


Figure 103. Permeability variation through injection time in sample 6Y.

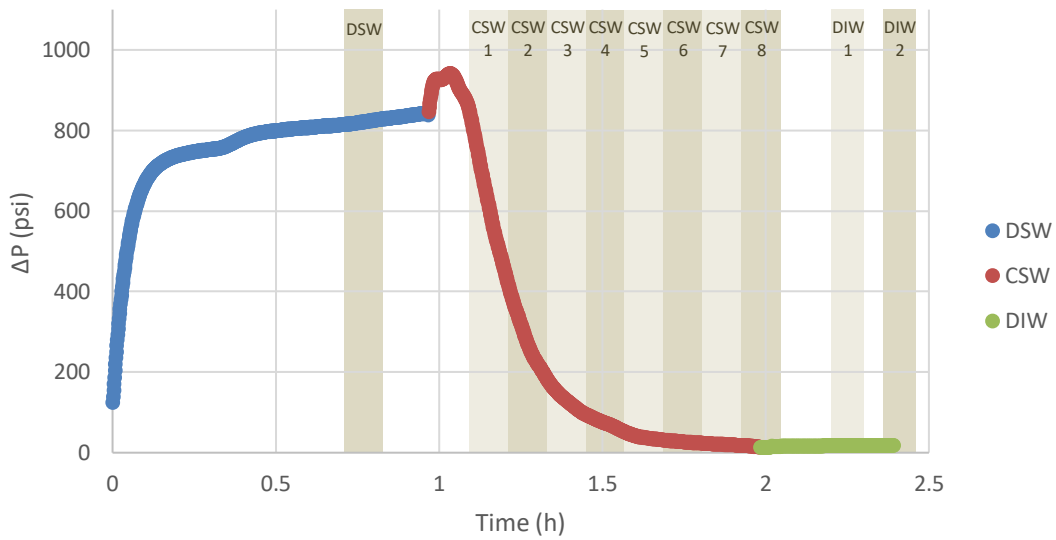


Figure 104. Differential pressure variation through injection time in sample 6X.

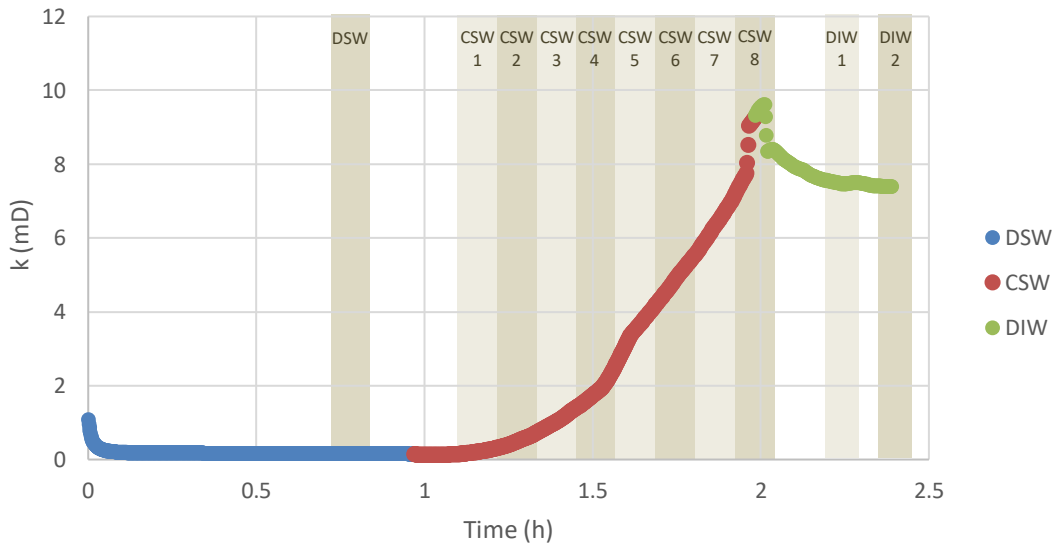


Figure 105. Permeability variation through injection time in sample 6X.

### Samples 6Z and 3Z

Samples 6Z and 3Z presented a sharper peak in differential pressure at the start of CSW injection. After this initial rise and subsequent stabilization, sample 6Z presented a slow decrease in  $\Delta P$ , from 97 to 37 psi in 57 minutes (Figure 106), and a small permeability rise, from 1.6 to 4.1 mD (Figure 107).

The 3Z sample, on the other hand, had a quicker initial fall in  $\Delta P$ , from 54 to 14 psi in 14 minutes, and then stabilization, decreasing to 3.5 psi after another 32 minutes (Figure 108). Permeability had a large total increase, from 2 to 32 mD (Figure 109).

CHAPTER 4. RESULTS AND DISCUSSION

Gas permeability results indicated a similar increase in permeability for sample 6Z and a greater increase (twice the value) for sample 3Z (Table 10).

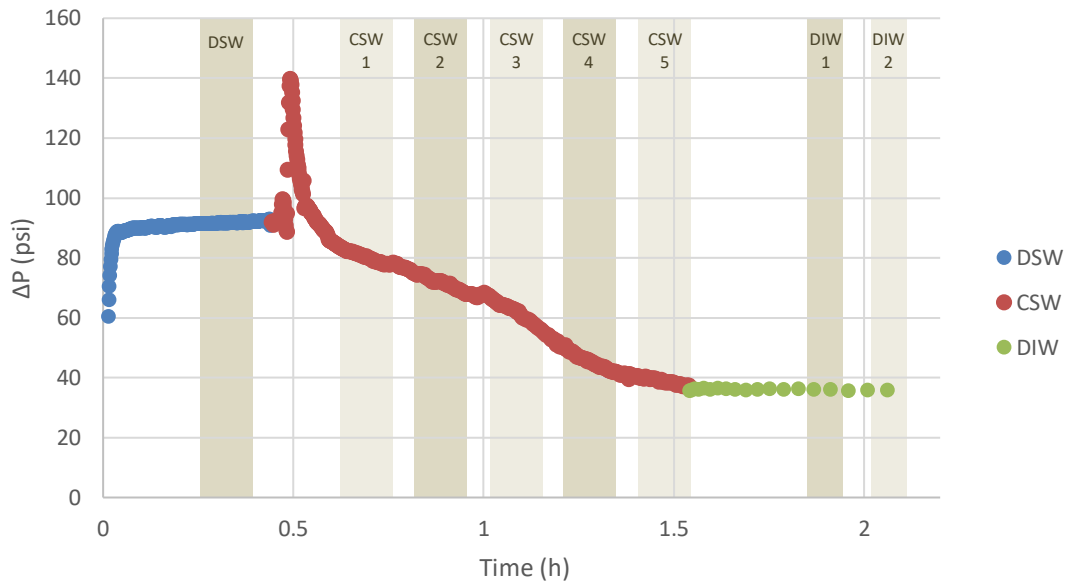


Figure 106. Differential pressure variation through injection time in sample 6Z.

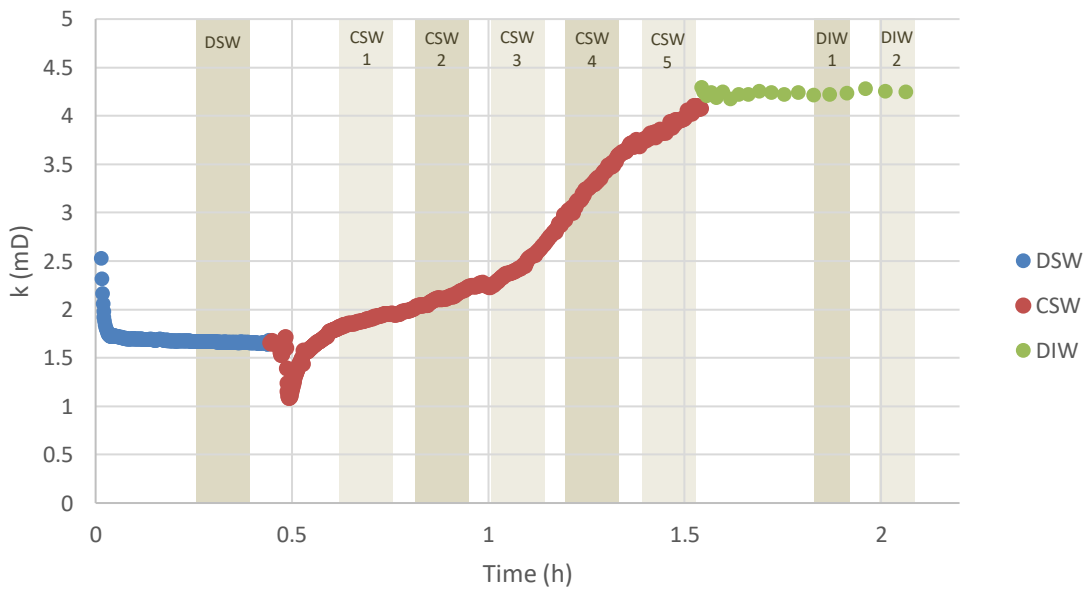


Figure 107. Permeability variation through injection time in sample 6Z.

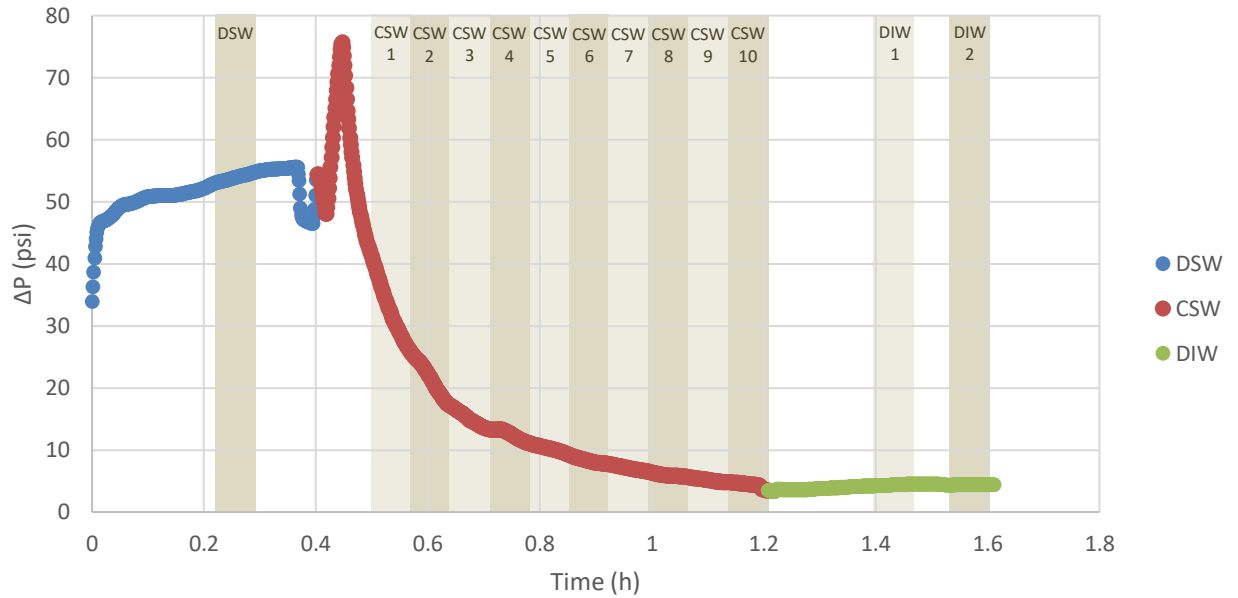


Figure 108. Differential pressure variation through injection time in sample 3Z.

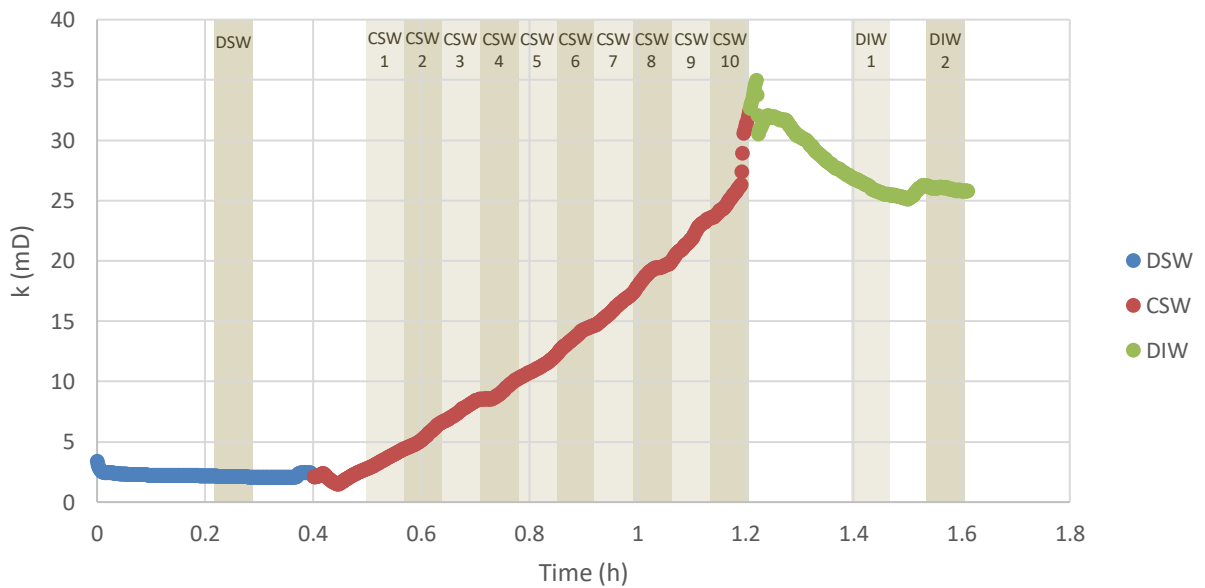


Figure 109. Permeability variation through injection time in sample 3Z.

### Samples 1X and 3Y

Sample 1X, due to its very high permeability, presented very low  $\Delta P$  values, making it impossible for the absolute transducers to reliably detect the pressure variation. Therefore, it is not possible to perform reliably interpretations from the graphics in Figure 110 and Figure 111.

Sample 3Y, also with high permeability, likewise presented low  $\Delta P$  values, stabilizing

## CHAPTER 4. RESULTS AND DISCUSSION

at around 0.45 psi after 18 minutes of CW injection and having small variations until the end of the experiment (Figure 112). Permeability values also stabilized around 300 mD (Figure 113).

Gas permeability results indicated a decrease in permeability for both samples (Table 10).

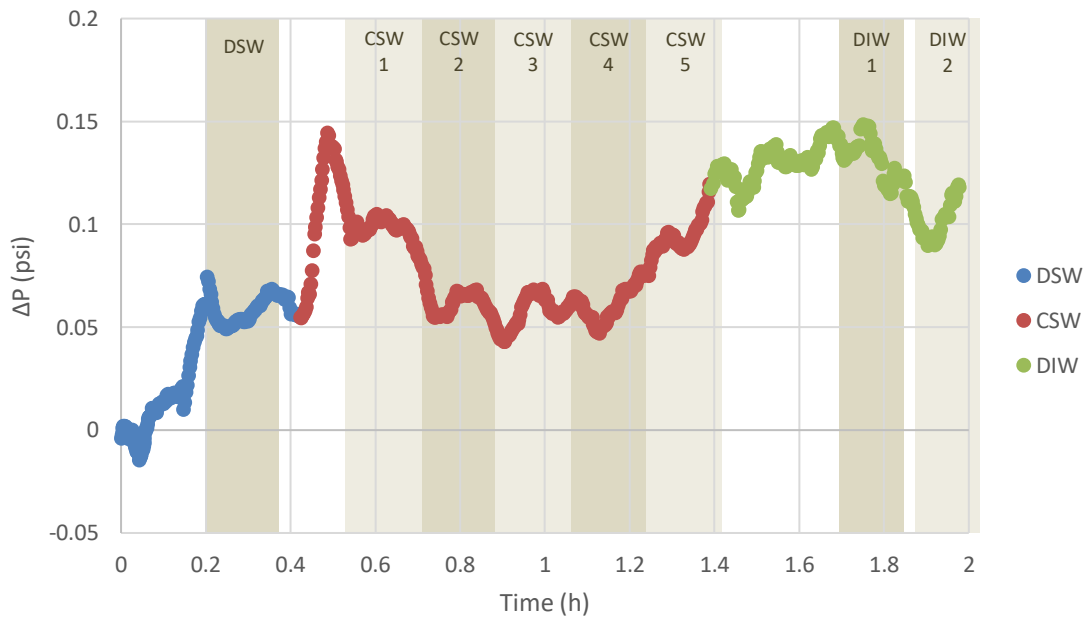


Figure 110. Differential pressure variation through injection time in sample 1X.

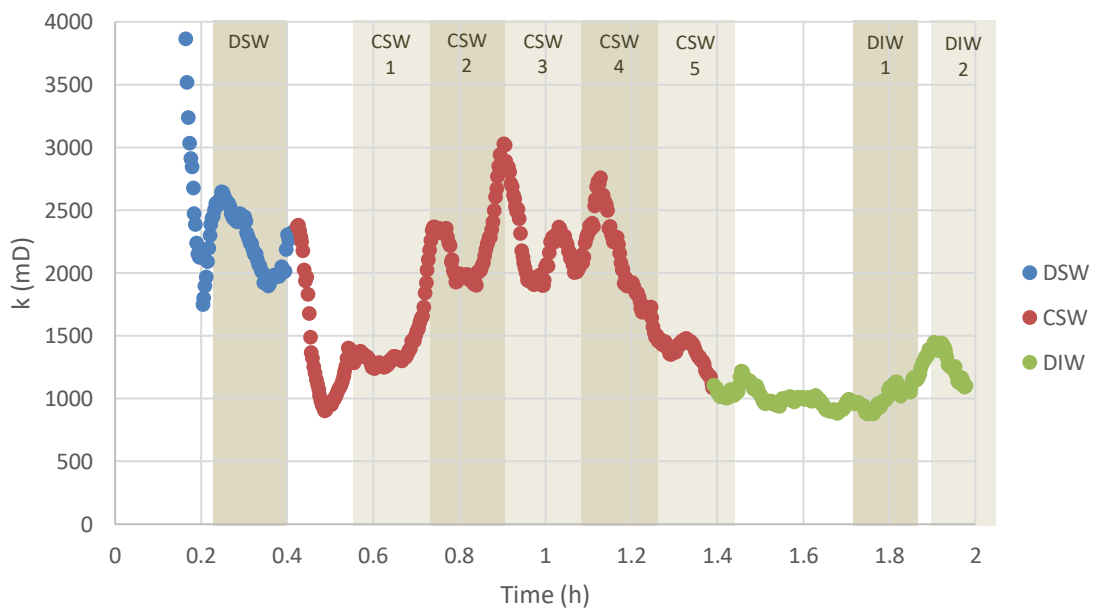


Figure 111. Permeability variation through injection time in sample 1X.

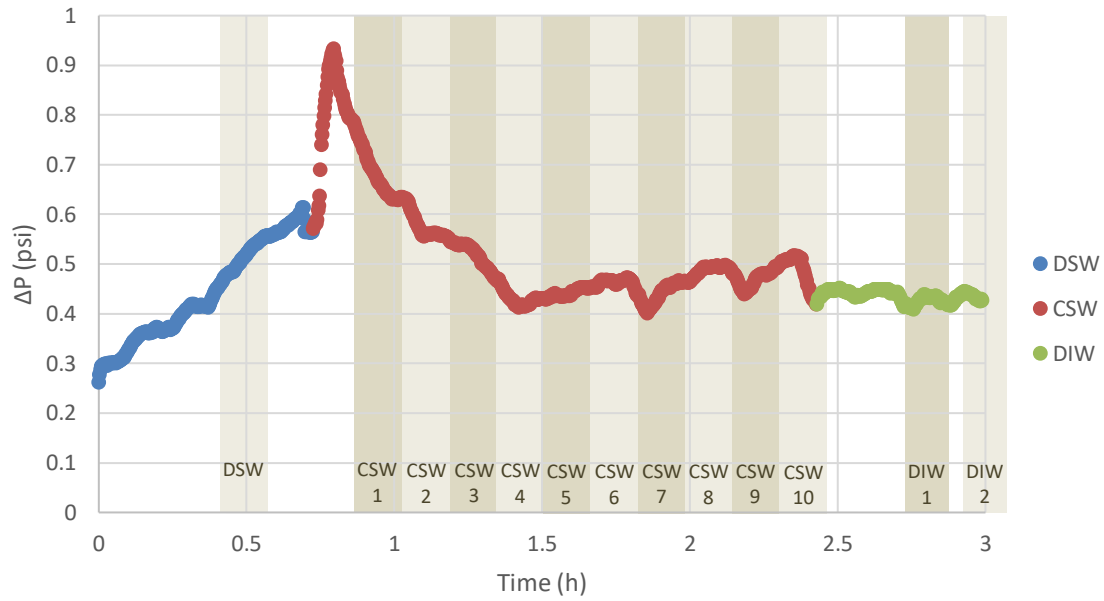


Figure 112. Differential pressure variation through injection time in sample 3Y.

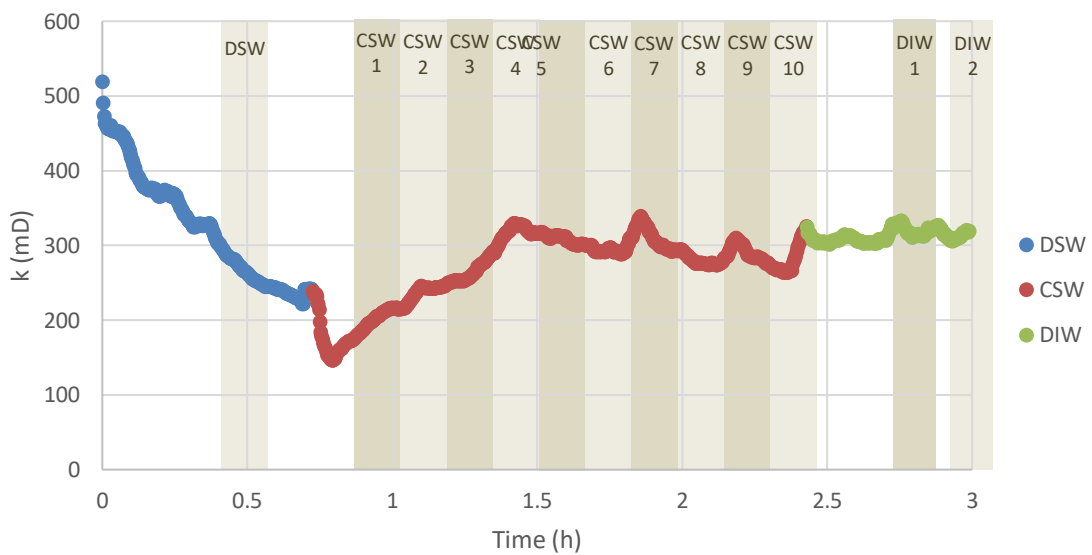


Figure 113. Permeability variation through injection time in sample 3Y.

#### 4.7. Ion chromatography results

The results of the ion chromatography analyze performed on the effluent fluid samples are gathered in Table 15.



Table 15. Ion chromatography results.

	Effluent sample	Cations (ppm) 1:100 dilution				Anions (ppm) 1:200 dilution	
		Na	K	Ca	Mg	Cl	SO <sub>4</sub>
<b>DSW</b>	DSW	9543.1	356.9	349.8	1150.1	18990	96.02
<b>1X</b>	DSW	8481.2	312.4	327.2	1027.7	16893.8	86.79
	CSW 1	9143.6	345.7	1077.6	1111.7	18205.9	96.75
	CSW 2	8585.3	315	949	1058.9	17107.7	90.3
	CSW 3	9335.2	342.7	756.3	1133.4	18575.6	95.3
	CSW 4	9268.8	337.4	967.1	1129	18460.8	96.95
	CSW 5	8097.8	299	825.1	989.4	16116.3	85.25
	DIW 1	571.6	23.9	210.3	108.7	1141.8	16.82
	DIW 2	298.6	22.5	164.2	77.4	595.6	13.97
<b>3Y</b>	DSW	9493.3	347.8	355.2	1141.7	18927.7	97.69
	CSW 1	9386.5	345.5	1054	1133.4	18763.6	97.42
	CSW 2	9256.5	340.6	1343.3	1128.1	18491.4	100.49
	CSW 3	9442.4	347.4	1322	1142.8	18878.1	102.52
	CSW 4	9800.2	384.2	1122.5	1245.3	19799	101.7
	CSW 5	9575.3	363.4	1191.4	1172.9	19113.5	101.54
	CSW 6	9406.6	349.9	1221.1	1152.3	18773.5	100.57
	CSW 7	9630.4	352.3	1177.8	1165.7	19229.7	102.15
	CSW 8	9862.1	358.8	1205.5	1204.6	19663.1	103.89
	CSW 9	9771	355.7	1200.2	1178.5	19503	103.56
	CSW 10	9517.8	358.8	1178.3	1133.8	18981.5	100.89
	DIW 1	793.3	33.7	200.8	132.7	1582.2	19.06
	DIW 2	490.4	22.1	171.8	97.2	975.6	16.22
<b>3Z</b>	DSW	8913.6	331.5	356.5	1086.2	17743.2	92.35
	CSW 1	8793.9	328.2	918.3	1067	17515.3	88.26
	CSW 2	7707.3	288.9	568.6	923	15358.1	80.11
	CSW 3	8852.4	323.8	1096.4	1083.4	17619.6	92.95
	CSW 4	7671.1	279.6	923.7	940.4	15273	81.56
	CSW 5	7487	276.7	1025.4	923.9	14913.2	81.49
	CSW 6	7721.1	281.9	956.2	950.3	15367	83.6
	CSW 7	7743.7	294.9	915.3	959.4	15418.1	82.24
	CSW 8	8626.8	316.3	955.7	1053.6	17180	90.92
	CSW 9	9301.6	343.1	968.8	1130.6	18512.81	85.89
	CSW 10	8392	309.1	918.9	1027.7	16711.2	87.7
		DIW	877.4	39.4	203.5	149.3	1750
<b>6X</b>	DSW	9864	358.5	393.1	1180.8	19653.5	99.2
	CSW 1	9636.1	348.3	941.3	1166.1	19190.1	91.95
	CSW 2	9347.4	342.6	926.7	1121.5	18628.7	91.75
	CSW 3	9362.7	341	885.7	1126.7	18633.4	91.92
	CSW 4	9557.6	351.2	931.1	1148.5	19043.9	94.18
	CSW 5	9502.6	349.3	958.8	1140.6	18906	94.39
	CSW 6	9755.2	357.3	968.4	1176.2	19433.6	97.14
	CSW 7	9437.2	346.9	1019.9	1743.1	18783.9	95.64
	CSW 8	9415.5	347.1	984.8	1148.4	18755.3	95.06
	DIW 1	811.7	41.9	201.2	138.7	1623.2	18.9

CHAPTER 4. RESULTS AND DISCUSSION

	DIW 2	342.6	16.3	118.2	87.7	688.9	14.56
<b>6Y</b>	CSW 1	9182	339.4	903.2	1154.6	18282.7	83.97
	CSW 2	9202	337.9	891.2	1125.8	18331.1	86.03
	CSW 3	9292.1	343.1	889.2	1126.1	18508.8	87.61
	CSW 4	9298	344.8	831.1	1119.2	18503	87.65
	CSW 5	9175.9	334.9	825.2	1103.5	18265.8	87.72
	DIW 1	1939.2	80.7	496.9	266.7	3872.5	29
	DIW 2	780.1	35.2	326	135.3	1541.8	18.82
<b>6Z</b>	DSW	9153.8	334.6	372.6	1106.3	18226.3	94.54
	CSW 1	9212.9	338.3	947.8	1115.7	18349.4	86.27
	CSW 2	8616.3	312.4	865.3	1037.6	17159.9	82.89
	CSW 3	9122.9	336.6	928.4	1097.1	18144.9	87.84
	CSW 4	9074.7	330.9	916.2	1095.8	18064.1	88.42
	CSW 5	9447.5	344.6	936	1131.1	18794.1	91.92
	DIW 1	1567.8	62.5	470.6	225.5	3108.2	26.68
	DIW 2	836.4	37.2	101.8	135.6	1656.4	19.48

The concentration in ppm of sodium (Na), potassium (K), calcium (Ca), magnesium (Mg), chlorine (Cl), and sulfate (SO<sub>4</sub>) in the effluents of each sample is indicated in the following graphs, together with two dotted horizontal lines indicating the values for the DSW injected into the samples for comparison (Figure 114 to Figure 116).

Calcium concentrations in CSW effluents are 62 to 284% higher than in the injected DSW concentration, indicating the dissolution of calcium minerals, especially calcite (CaCO<sub>3</sub>), generated by the solution injection. In samples 1X, 3Y, and 3Z, calcite dissolution oscillated during CSW injection, while in the samples 6X, 6Y, and 6Z, Ca concentration in the effluent presented less variation. DIW 1 results from samples 6Y and 6Z indicate that calcite dissolution continued beyond the start of DIW injection.

Magnesium concentrations in CSW effluents are 20% lower to 8% higher than those of DSW (with the exception of the sample 6X, in which the CSW 7 effluent is 51% higher), indicating precipitation and dissolution of magnesium, possibly from the Mg present at the calcite in the samples or from dolomite minerals (CaMg(CO<sub>3</sub>)<sub>2</sub>), caused by dolomitization.

Sodium concentrations in CSW effluents are 21% lower to 3% higher than those of DSW; potassium concentrations are 22% lower to 8% higher; chlorine concentrations are 21% lower to 4% higher; and sulfate concentrations are 16% lower to 8% higher. The lower values of these elements in the effluents compared to the concentration in the injected fluid indicate precipitation of salts in the pore space of the samples, mainly in 3Z, 1X, 6Z, and 6Y.

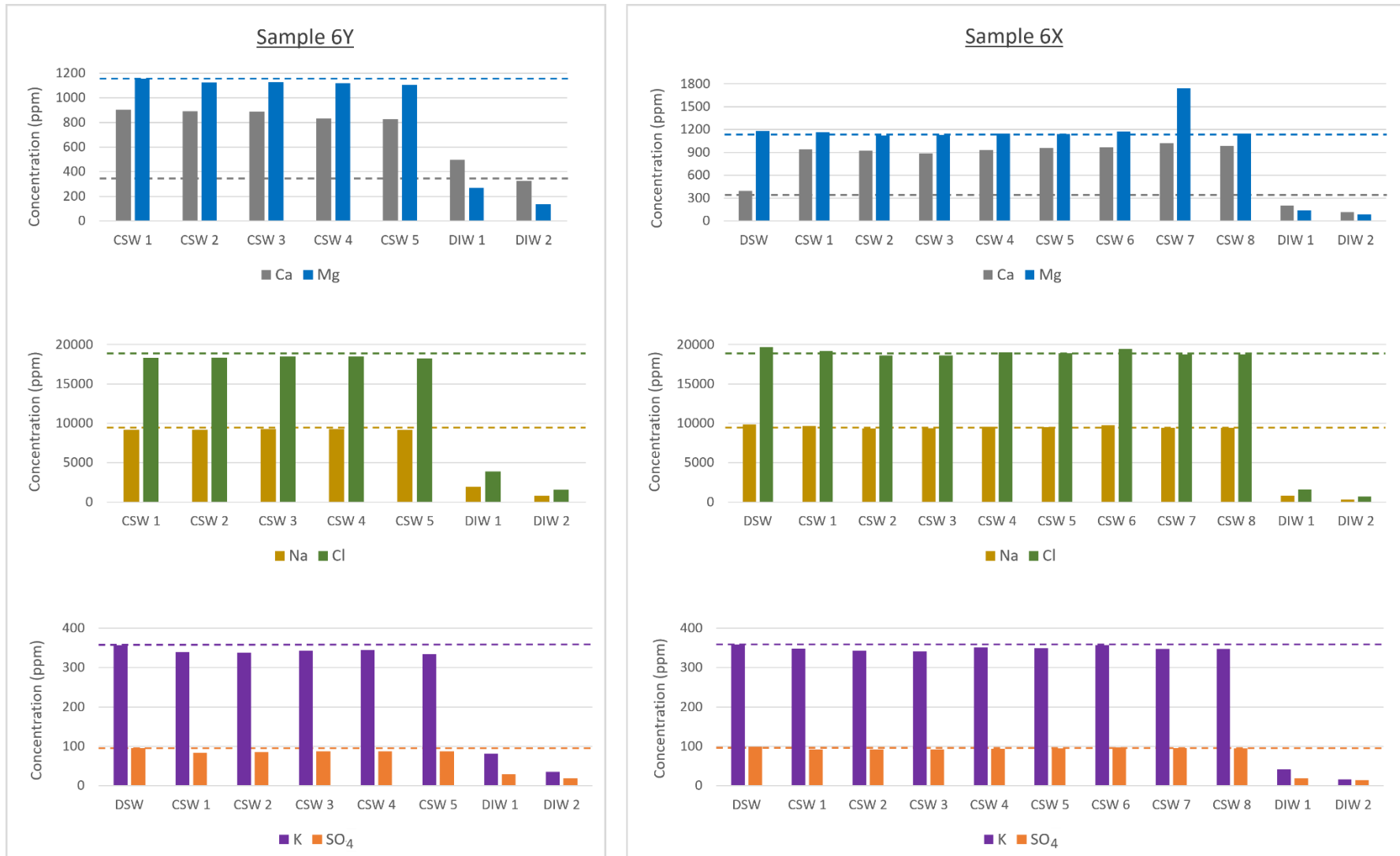


Figure 114. Cations and anions concentration, in ppm, from 6Y and 6X samples effluents. Dotted lines indicate the concentrations of each element in the injected DSW for comparison.

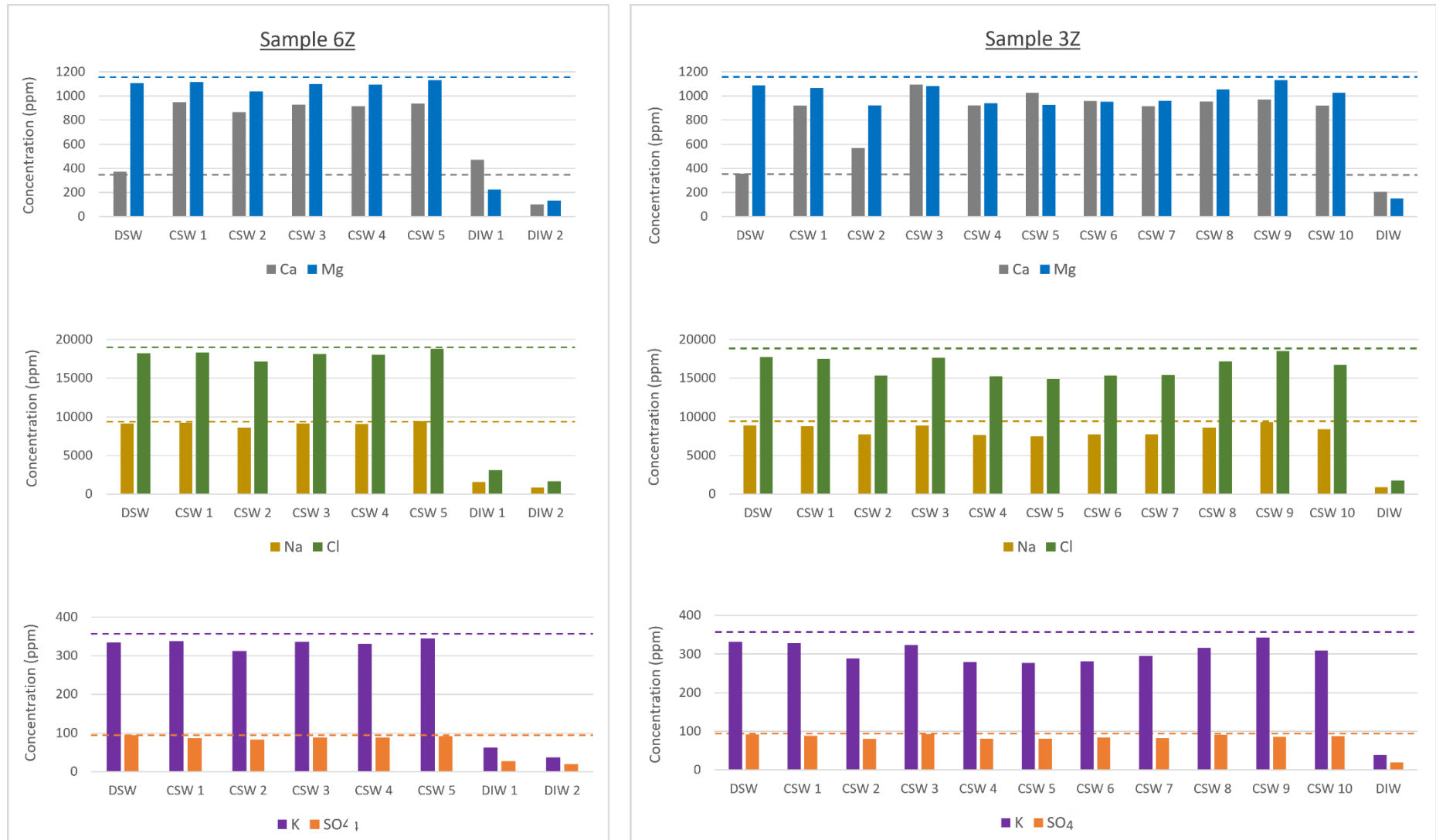


Figure 115. Cations and anions concentration, in ppm, from 6Z and 3Y samples effluents. Dotted lines indicate the concentrations of each element in the injected DSW for comparison.

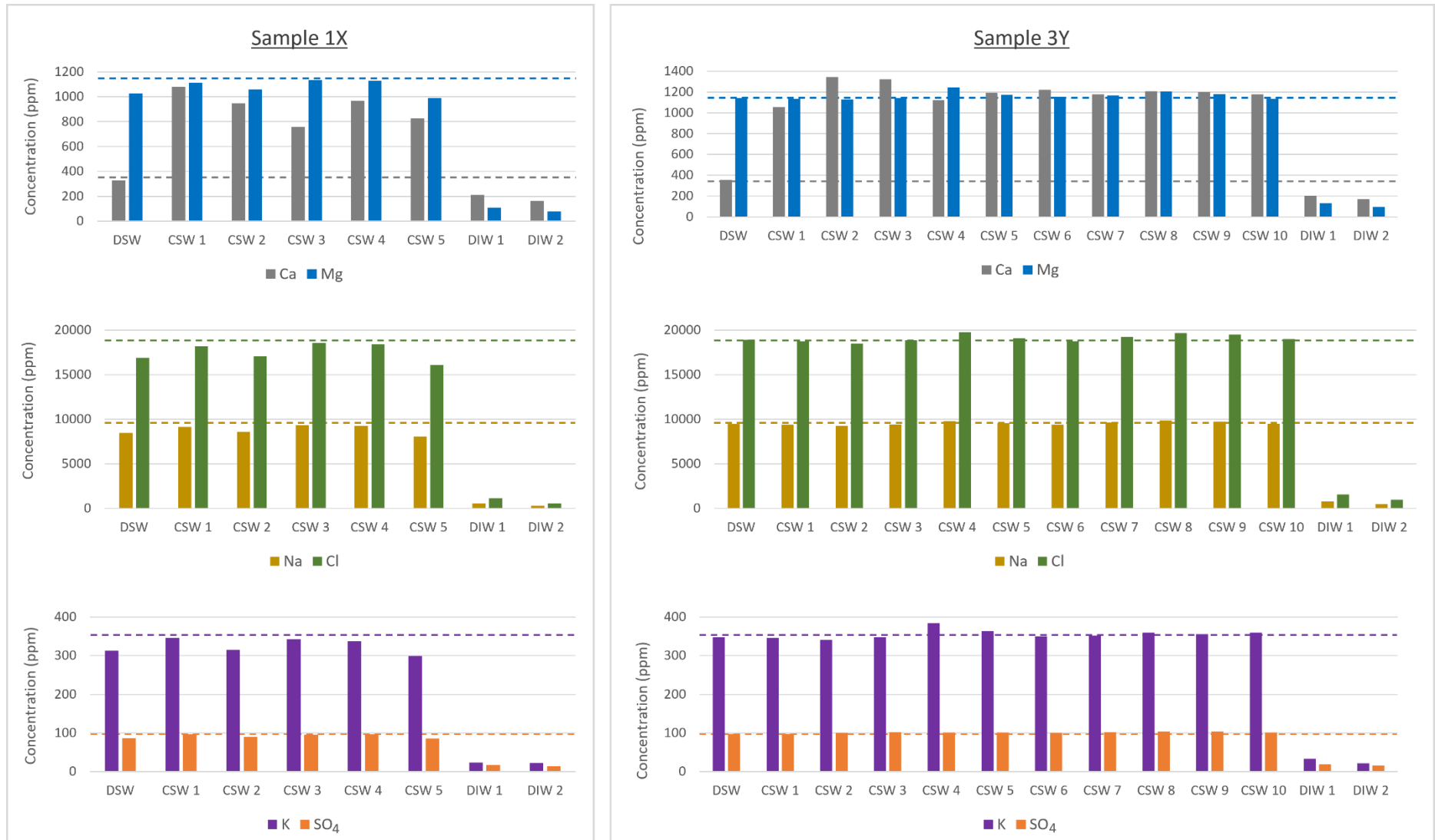


Figure 116. Cations and anions concentration, in ppm, from 1X and 3Y samples effluents. Dotted lines indicate the concentrations of each element in the injected DSW for comparison.

## CHAPTER 4. RESULTS AND DISCUSSION

Figures 117 and 118 show the difference between the amount (in ppm) of ions that outflowed from the sample and the amount that was injected. Positive values indicate dissolution and negative values indicate precipitation of minerals and salts.

All samples showed high dissolution of Ca minerals, especially 3Y (Figure 117). The dissolution of samples in which 5 pore volumes were injected (6Y, 6Z, and 1X) was very similar, despite the difference between the pore volume of each sample (sample 1X has 40% more pore volume in comparison with 6Y and 6Z). The dissolution of the low permeability samples that had higher pore volumes injection (6X and 3Z) was also similar (considering that 6X was injected with two pore volumes less than the 3Z). 3Y sample showed greater dissolution in comparison (50% more than 3Z). This may be due to the porous structure of 3Y facilitating fluid percolation or the value of 10 nPV, compared to 5 nPV, together with the larger porous volume of the sample (corresponding to 5cc of CO<sub>2</sub> dissolved in water) being decisive for the significant increase in dissolution.

Four samples - especially 3Z - showed precipitation of Mg minerals and two samples showed its dissolution. These two may be due to the dolomitization that occurred in these samples (dolomite being a calcium and magnesium carbonate mineral abundant in nature).

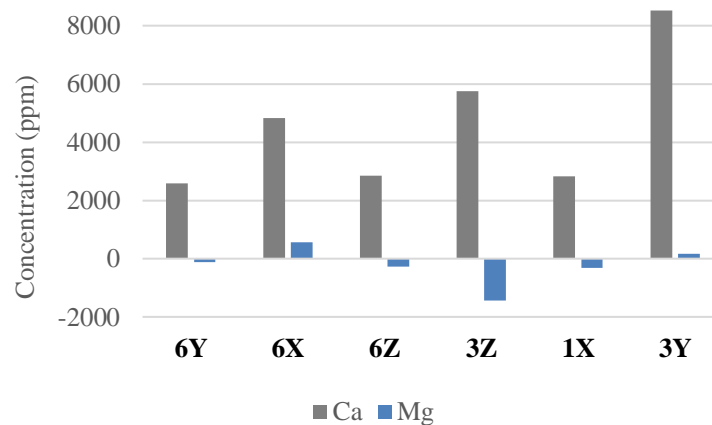


Figure 117. Difference between the amount (in ppm) of Ca and Mg that outflowed from the sample and the amount that was injected. Positive values indicate dissolution of calcium minerals (especially calcite) and magnesium minerals (possibly dolomite) and negative values indicate precipitation of these minerals.

Figure 118 represents the difference between the amount (in ppm) of chlorine (Cl), sodium (Na), potassium (K), and sulfate (SO<sub>4</sub>) that outflowed from the sample and the amount that was injected. Positive values indicate dissolution and negative values indicate salt precipitation.

Five samples showed precipitation of salts, mainly NaCl and, to a lesser extent, K and

SO<sub>4</sub> salts, and 3Y showed little dissolution of these.

Salt precipitation wasn't directly related to the samples' porous volume, or the amount of CW injected, probably due to the pore structure of each one. 3Z, being the most heterogeneous sample, due to the having a contact between the vuggy/microbial facies and the laminated/massive facies, had the highest amount of precipitation.

Since the samples were cleaned for salts' removal after CWI (using the hot Soxhlet extraction), it is assumed that salt precipitation did not change the post-injection analysis results.

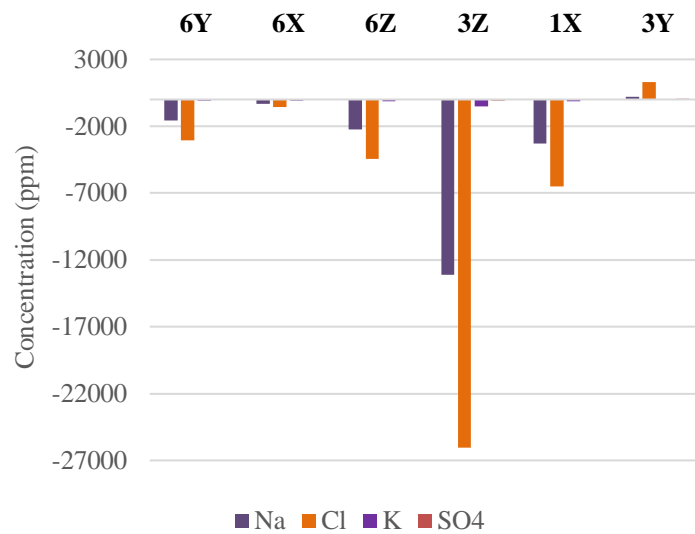


Figure 118. Difference between the amount (in ppm) of Cl, Na, K, and SO<sub>4</sub> that outflowed from the sample and the amount that was injected. Positive values indicate dissolution and negative values indicate salt precipitation.

#### 4.8. Results correlation

Table 16 gathers key information obtained during this research: gas porosity and permeability variation (in percentage), gas permeability pre-CWI, the total volume of carbonated water (CW) injected (obtained by multiplying each sample's pore volume by the volume of pores injected, being 5, 8 or 10 PV) and the total calcium output (obtained by summing all the calcium effluent from the CWI samples minus the value of Ca in the desulfated water (DSW) multiplied by the pore volume of CW injected in each plug).

The comparison in the table shows some interesting results. For samples 6Y and 6Z, in which very similar pore volumes of CW were injected (28.15 cc for 6Y and 28 cc for 6Z) and which presented similar amounts of effluent calcium (2591 ppm for 6Y and 2845 ppm for 6Z), there were no similar changes in permeability values. 6Y, whose pre-CWI

CHAPTER 4. RESULTS AND DISCUSSION

permeability was 59% lower than that of the 6Z sample, showed almost 4 times greater permeability variation in comparison.

Table 16. Gas porosity variation, gas permeability pre-CWI, gas permeability variation, total volume of carbonated water (CW) injected and calcium output for each sample.

Sample	Gas porosity variation (%)	Gas permeability pre-CWI* (mD)	Gas permeability variation (%)	CW total pore volume injected (cc)	Calcium output (ppm)
6Y	-5.40%	0.63	+1006%	28.15	2591
6X	+1.60%	0.19	+5433%	33.44	4818
6Z	-6.90%	1.53	+256%	28.00	2845
3Z	-8.30%	3.31	+1845%	36.30	5749
1X	+2.90%	1748.76	-5.60%	39.45	2826
3Y	-1.60%	1795.41	-10.70%	83.70	8518

\* Klinkenberg effect corrected.

Comparing samples 6X and 3Z, the volume of CW injected in 6X was 8% smaller than that injected in 3Z (33.44 cc for 6X and 36.3 cc for 3Z) and the Ca outflow was 16% smaller (4818 ppm for 6X and 5749 ppm for 3Z). However, the permeability variation of these two samples is not directly correlated with the results mentioned above, being almost 3 times greater for the 6X sample compared to the 3Z sample.

Comparing the samples with similar permeability between each other (6Y with 6X and 6Z with 3Z), the differential pressure stabilization after 5 PV injected seems to have favored dissolution, generating a higher Ca output compared to the injected PV: an increase of injected pore volume in 16% (33.44 cc in 6X in comparison to 28.15 cc in 6Y) to 23% (36.3 cc in 3Z in comparison to 28 cc in 6Z) generated an increase of 46% (4818 ppm in 6X in comparison to 2519 ppm in 6Y) to 49% (5749 ppm in 3Z in comparison to 2845 ppm in 6Z) in calcium output and a permeability increase of 5.4 (+5433% in 6X in comparison to +1006% in 6Y) to 7.2 times (+1845% in 3Z in comparison to +256% in 6Z).

For these four low permeability samples (6Y, 6X, 6Z, and 3Z), the Ca outflow reflects (even though not directly) the permeability increase, but it doesn't reflect the porosities variation, which doesn't show a pattern. The CWI flow rate (1cc/min), high for these samples due to its low permeabilities, and the more uniformed pore sizes probably led to a uniform calcite dissolution with low precipitation, increasing its permeabilities while not affecting porosity considerably.



The two high permeability samples (1X and 3Y), however, do not show a relationship between the amount of dissolved calcium and permeability variation. Comparing samples 1X and 3Y, the volume of CW injected in 1X was 53% smaller than for 3Y (39.45 cc for 1X and 83.7 cc for 3Y) while the Ca output was 67% smaller (2826 ppm for 1X and 8518 ppm for 3Y) and permeability variation was almost 2 times smaller. Porosity variation didn't show a pattern for these samples as well.

The vugs in the high permeability samples probably increased turbulence in the fluid streamlines – as interpreted by KHAN *et al.* (2019) –, causing less dissolution and more precipitation, in comparison with the non-vugular (low permeability) samples, which probably had linear flow during injection, leading to a more uniform dissolution.

#### 4.9. Brazilian Pre-salt applications

As previously discussed, the lithologies studied in this research are partial analogues of carbonates from the Brazilian pre-salt, the most important oil reservoir in the country. Due to the high costs of taking core samples from offshore drilling, especially in Brazilian pre-salt carbonate deepwater wells, analogues were used, which is a common practice in the oil and gas industry.

In this work, samples were injected with carbonated water under laboratory conditions, at 500 psi (or 3.45 MPa) and 20°C (or 68°F). Reservoir conditions found in the Brazilian pre-salt carbonates have temperatures between 80 and 100°C (176 to 212°F) and around 8700 psi (60 MPa) (HAFEMANN *et al.*, 2014). According to the CO<sub>2</sub> solubility in relation to temperature and pressure graph of Figure 119 (modified from Figure 8), solubility in pre-salt conditions would be about 70% higher, indicating that the results obtained by CWI directly in these reservoirs would be even more pronounced. However, brine salinity in pre-salt can be up to 700% of the values used in this work (FAÇANHA *et al.*, 2016), which decreases CO<sub>2</sub> solubility by around 60%, according to the CO<sub>2</sub> solubility in relation to total dissolved solids graph of Figure 120.

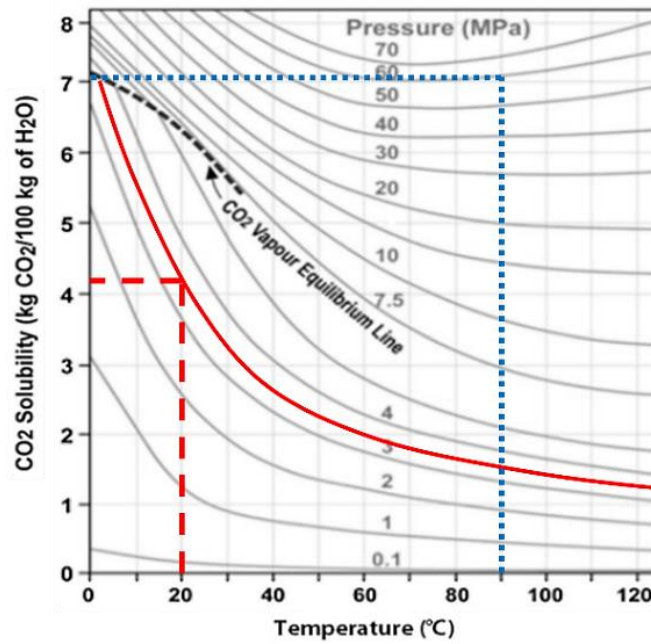


Figure 119. Solubility of CO<sub>2</sub> in water (PERKINGS, 2003). Red curve and red dashed lines indicate CO<sub>2</sub> solubility under temperature and pressure conditions used in this research (3.45 MPa and 20°C); blue dotted lines indicate solubility under Brazilian pre-salt reservoir conditions (60 MPa and 80 to 100°C).

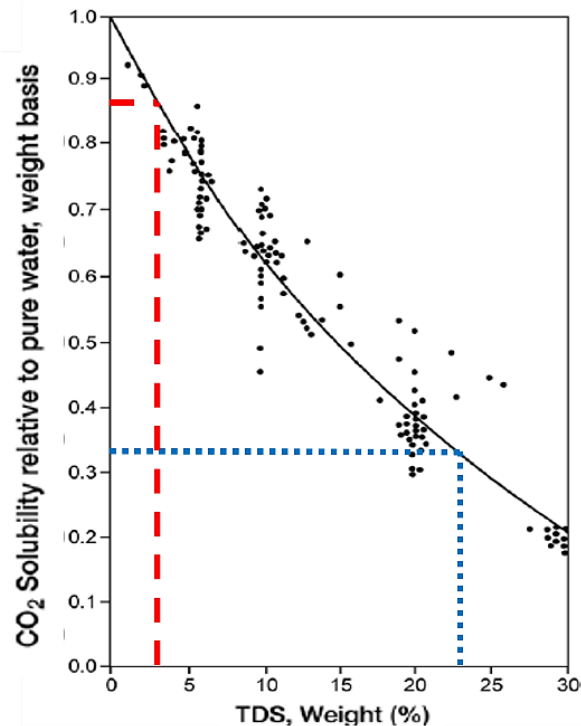


Figure 120. CO<sub>2</sub> solubility in brine relative to that in pure water, showing experimental points reported by ENICK and KLARA (1990) and correlation developed by METZ *et al.* (2005) (TDS stands for total dissolved solids). Red dashed lines indicate the CO<sub>2</sub> solubility under salinity conditions used in this research (30,500 mg/L or 3.05%); blue dotted lines indicate solubility under Brazilian pre-salt reservoir conditions (226,694 mg/L or 22.7%, according to FAÇANHA *et al.*, 2016).

## Chapter 5

# Summary of results and Conclusions

From the analyzes carried out on the Mupe Member carbonate it was possible to determine the following mineralogical, petrographic, and petrophysical properties:

- From observations with the naked eye, it was possible to determine the presence of distinctive sedimentary facies, which can be separated into two groups: a vuggy/microbial one and a laminated to a massive one.
- XRD analyses indicated the samples are composed almost entirely of low magnesium calcite, with smaller quantities of quartz and barite.
- From thin sections analysis it was observed that the vuggy/microbial facies samples have columnar thrombolytic structure and micrite matrix, being classified as a thrombolite (AITKEN, 1967), and the laminated/massive facies, rich in a micritic matrix, was classified as a wackestone (DUNHAM, 1962). Both facies have chalcedony spherules dispersed in the matrix and sparry calcite crystallized in the pore's walls. The main porosity types observed are vugular, intergranular, moldic, growth-framework, and microporosity.
- Routine petrophysical analyzes indicated that the plugs that went to the next analysis steps had variable porosity and permeability values and could be separated into three groups based on their permeabilities: very low ( $< 1$  mD), low (1 to 5 mD), and very high ( $> 1000$  mD).
- Micro-CT imaging indicated that the vuggy/microbial facies samples have relative isotropy in their porous structure and the laminated/massive facies have certain anisotropy.
- NMR results validated helium porosity values and indicated that the plugs are very heterogeneous, having pore size distributions varying from bimodal to polymodal.
  - The acquisition of measurements on different equipment made it difficult to compare the results.

## CHAPTER 5. SUMMARY OF RESULTS AND CONCLUSIONS

The following conclusions could be drawn:

- Due to the results of the XRD and thin sections analyses, the reaction of CO<sub>2</sub> with the rock was expected to generate dissolution of calcite, the main mineral constituent of the samples. In fact, ion chromatography results indicated that all samples suffered calcite dissolution, and in some occurred dissolution and precipitation of magnesium and precipitation of salts in the pore space.
- For the samples with low permeability (< 3mD) there was a significant increase in the permeability of the four samples.
  - The differential pressure stabilization after 5 PV injected seems to have favored dissolution in the later stages of injection: an increase in pore volume injected from 3 to 5 volumes in these samples was sufficient to cause an increase of up to 16 times compared to samples in which only 5 volumes were injected.
- For the high permeability samples (> 1500 mD) there was a small decrease in the permeability of the two samples.
  - Post-CWI samples' cleaning (using the hot Soxhlet extraction method) indicates that k-reduction wasn't caused by salt precipitation during the injection. Possible causes include grain displacement and/or precipitation generated by flow deceleration in the vugular pores (or vugs), causing formation damage.
- Gas porosity and micro-CT analysis results indicated small porosity variation, with small decreases and increases. For the three non-vugular samples (6X, 6Y, and 6Z), micro-CT results indicated a trend of decrease in porosity towards the CW outlet face. The other three samples – the vugular ones –, presented a more homogeneous porosity variation along the samples' length and one sample (3Y) exhibited a sharp decrease in porosity close to the outlet face.
- Salt precipitation is an issue to be considered, especially in samples with high heterogeneity, mainly in contact between rocks with different permeabilities.
- The chosen flow rate (1cm<sup>3</sup>/min) likely impacted dissolution, particle migration, and salt precipitation during injection, being high for low permeability samples and low for high permeability samples. This is a factor to be considered in practical applications.

The considerable increase in permeability for the laminated/massive low permeability facies samples together with the change in the porosity values indicate good feasibility for the use of samples similar to those of the Mupe Member in CO<sub>2</sub> storage, especially in shallow

## *CHAPTER 5. SUMMARY OF RESULTS AND CONCLUSIONS*

reservoirs, with characteristics similar to those used during the experiments. For higher temperature and pressure settings (similar to the Brazilian pre-salt conditions, for example), changes in CO<sub>2</sub> solubility must be taken into account, as should the potential for post-dissolution carbonate re-deposition once the injected cold fluid heats up to reservoir temperature.

For the vuggy/microbial facies samples, the small amount of formation damage generated can be a problem in large-scale applications. More studies on these rocks are needed to determine whether these results would preclude the application of CCS in similar formations.

The recommended future analyses for these rocks include: (1) performing CWI for longer periods, with the injection of more pore volumes, and under reservoir conditions, for the purpose of verifying if the observed results will be maintained, (2) flooding with cold water and then using that same outlet water to flood another core at temperature to examine the potential for scaling-related damage – this condition could simulate deeper reservoir interactions and impairment and (3) executing core flooding tests injecting water first to create an extensive cooling region, then moving to CWI to push that scaling risk further from the well where it should matter less.

# References

- AHR, Wayne M. **Geology of carbonate reservoirs: the identification, description and characterization of hydrocarbon reservoirs in carbonate rocks**. John Wiley & Sons, 2011.
- AITKEN, James D. Classification and environmental significance of cryptalgal limestones and dolomites, with illustrations from the Cambrian and Ordovician of southwestern Alberta. **Journal of Sedimentary Research**, v. 37, n. 4, p. 1163-1178, 1967.
- ANP (AGÊNCIA NACIONAL DO PETRÓLEO, GÁS NATURAL E BIOCOMBUSTÍVEIS). **ANP Resolution N°. 16**. 18 June 2008. Available from: <https://atosoficiais.com.br/anp/resolucao-n-16-2008?origin=instituicao&q=16/2008>. Accessed: 19 May 2022.
- ANP (AGÊNCIA NACIONAL DO PETRÓLEO, GÁS NATURAL E BIOCOMBUSTÍVEIS). **Boletim Mensal da Produção de Petróleo e Gás Natural**. 6 May 2022. Available from: <https://www.gov.br/anp/pt-br/centrais-de-conteudo/publicacoes/boletins-anp/boletins/boletim-mensal-da-producao-de-petroleo-e-gas-natural>. Accessed: 19 May 2022.
- BACHU, Stefan. Sequestration of CO<sub>2</sub> in geological media: criteria and approach for site selection in response to climate change. **Energy Conversion and Management**, vol. 41, no. 9, p. 953-970, June 2000. Available from: [https://doi.org/10.1016/s0196-8904\(99\)00149-1](https://doi.org/10.1016/s0196-8904(99)00149-1).
- BAGRINTSEVA, Ksenia I. **Carbonate reservoir rocks**. Hoboken, New Jersey: John Wiley & Sons, 2015. ISBN 9781119083573.
- BAHAR, Mohammad Mohammazadeh; LIU, Keyu. Measurement of the Diffusion Coefficient of CO<sub>2</sub> in Formation Water Under Reservoir Conditions: Implications for CO<sub>2</sub> Storage. *In*: SPE ASIA PACIFIC OIL AND GAS CONFERENCE AND EXHIBITION, Perth, Australia. **SPE Asia Pacific Oil and Gas Conference and Exhibition**. [S. l.]: Society of Petroleum Engineers, 2008. Available from: <https://doi.org/10.2118/116513-ms>.
- B EGLINGER, Suzanne E.; DOUST, Harry; CLOETINGH, Sierd. Relating petroleum system and play development to basin evolution: West African South Atlantic basins. **Marine**

## REFERENCES

- and Petroleum Geology**, v. 30, n. 1, p. 1-25, 2012. Available from: <https://doi.org/10.1016/j.marpetgeo.2011.08.008>.
- BELL, F. G. ENGINEERING GEOLOGY | Problematic Rocks. In: BELL, F. G. **Encyclopedia of Geology**. [S. l.]: Elsevier, 2005. p. 543-554. ISBN 9780123693969. Available from: <https://doi.org/10.1016/b0-12-369396-9/00220-3>.
- BISWESWAR, Ghosh; AL-HAMAIRI, Abdullah; JIN, Soo. Carbonated water injection: an efficient EOR approach. A review of fundamentals and prospects. **Journal of Petroleum Exploration and Production Technology**, v. 10, n. 2, p. 673-685, 2020. Available from: <https://doi.org/10.1007/s13202-019-0738-2>.
- BLAMEY, John *et al.* Mechanism of particle breakage during reactivation of CaO-based sorbents for CO<sub>2</sub> capture. **Energy & fuels**, v. 24, n. 8, p. 4605-4616, 2010. Available from: <https://doi.org/10.1021/ef100476d>.
- BRANTUT, Nicolas *et al.* Mechanisms of time-dependent deformation in porous limestone. **Journal of Geophysical Research: Solid Earth**, v. 119, n. 7, p. 5444-5463, 2014. Available from: <https://doi.org/10.1002/2014JB011186>.
- BRANTUT, Nicolas *et al.* Microstructural control of physical properties during deformation of porous limestone. **Journal of Geophysical Research: Solid Earth**, v. 123, n. 6, p. 4751-4764, 2018. Available from: <https://doi.org/10.1029/2018JB015636>.
- CAINELLI, César *et al.* Some remarks on the evolution of sedimentary basins along the Eastern Brazilian continental margin. **Episodes-Newsmagazine of the International Union of Geological Sciences**, v. 22, n. 3, p. 206-216, 1999.
- CANNON, Steve. **Petrophysics: a practical guide**. John Wiley & Sons, 2015.
- CARVALHO, Raissa TR *et al.* Prospective acid microemulsions development for matrix acidizing petroleum reservoirs. **Fuel**, v. 238, p. 75-85, 2019. Available from: <https://doi.org/10.1016/j.fuel.2018.10.003>.
- CHOQUETTE, Philip W., & PRAY, Lloyd C. Geologic Nomenclature and Classification of Porosity in Sedimentary Carbonates. **AAPG Bulletin**, vol. 54, 1970. Available from: <https://doi.org/10.1306/5d25c98b-16c1-11d7-8645000102c1865d>.
- CIVAN, Faruk. **Reservoir Formation Damage**. [S. l.]: Elsevier Science & Technology Books, 2015. 1042 p. ISBN 9780128018989.
- COATES, George R. *et al.* **NMR logging: principles and applications**. Houston: Haliburton Energy Services, 1999.
- D'ALMEIDA, Katia S. *et al.* Ocorrência de CO<sub>2</sub> em campos petrolíferos na margem leste brasileira. **Rio de Janeiro**, 2018.

## REFERENCES

- DE LUNA, José Leão *et al.* Petrophysical rock typing of Coquinas from the Morro do Chaves Formation, Sergipe-Alagoas Basin (Northeast Brazil). **Brazilian Journal of Geophysics**, v. 34, n. 4, p. 509-521, 2016. Available from: <http://dx.doi.org/10.22564/rbgf.v34i4.883>.
- DUNHAM, R.J. Classification of Carbonate Rocks According to Depositional Texture. In: Ham, W.E., Ed., **Classification of Carbonate Rocks**, AAPG, Tulsa, 1962. p. 108-121.
- ENICK, Robert M.; KLARA, Scott M. CO<sub>2</sub> SOLUBILITY IN WATER AND BRINE UNDER RESERVOIR CONDITIONS. **Chemical Engineering Communications**, vol. 90, no. 1, p. 23-33, Apr. 1990. Available from: <https://doi.org/10.1080/00986449008940574>.
- FAÇANHA, J.; SOHRABI, M.; DREXLER, S.; COUTO, P. Experimental Investigation of Wettability for Brazilian Pre-Salt Carbonates. **Rio Oil & Gas Expo and Conference**, Rio de Janeiro, Brazil, 24–27 October 2016.
- FIGUERA, Luis *et al.* Complex phased development for CO<sub>2</sub> EOR in oil carbonate reservoir, Abu Dhabi Onshore. In: **Abu Dhabi International Petroleum Exhibition and Conference**. OnePetro, 2014. Available from: <https://doi.org/10.2118/171967-MS>.
- GALLOIS, Arnaud. **Late Jurassic lacustrine carbonates: a multi-scale analysis of the Mupe Member (Purbeck Limestone Group) of the Wessex Basin, UK**. 2016. PhD Thesis. Royal Holloway, University of London.
- GALLOIS, Arnaud; BOSENCE, Dan. **Syn-rift lacustrine carbonates; cycles, microbial mounds, and brackish to hypersaline facies models; Purbeck Group, Wessex Basin, UK. Analogues for south Atlantic pre-salt carbonates?**. Conference on African E&P, 31<sup>st</sup> August- 1<sup>st</sup> September 2017, London UK.
- GALLOIS, Arnaud; BOSENCE, Dan; BURGESS, Peter M. Brackish to hypersaline facies in lacustrine carbonates: Purbeck Limestone Group, Upper Jurassic–Lower Cretaceous, Wessex Basin, Dorset, UK. **Facies**, v. 64, n. 2, p. 1-39, 2018. Available from: <https://doi.org/10.1007/s10347-018-0525-4>.
- GARCIA-GRANDA, S.; MONTEJO-BERNARDO, J. X-RAY ABSORPTION AND DIFFRACTION| X-Ray Diffraction| Powder. In: HAGE, D. S. (Ed.). **Reference Module in Chemistry, Molecular Sciences and Chemical Engineering**: Elsevier, 2013. ISBN 9780124095472.
- GLOBAL CCS INSTITUTE. **Global Status of CCS 2019: Targeting Climate Change**. 2019. Available from: [https://www.globalccsinstitute.com/wp-content/uploads/2019/12/GCC\\_GLOBAL\\_STATUS\\_REPORT\\_2019.pdf](https://www.globalccsinstitute.com/wp-content/uploads/2019/12/GCC_GLOBAL_STATUS_REPORT_2019.pdf). Accessed:



## REFERENCES

- 19 May 2022.
- GLOBAL CCS INSTITUTE. **Global Status of CCS 2020**: Vital to Achieve Net Zero. 2020. Available from: <https://www.globalccsinstitute.com/wp-content/uploads/2021/03/Global-Status-of-CCS-Report-English.pdf>. Accessed: 19 May 2022.
- GLOVER, P. W.; ZADJALI, I. I.; FREW, K. A. Permeability prediction from MICP and NMR data using an electrokinetic approach. **Geophysics**, v. 71, n. 4, p. F49-F60, 2006. Available from: <https://doi.org/10.1190/1.2216930>.
- GODOY, William *et al.* Computational and experimental pore-scale studies of a carbonate rock sample. **Journal of Hydrology and Hydromechanics**, v. 67, n. 4, p. 372-383, 2019.
- GREEN, Don W.; WILLHITE, G. Paul. **Enhanced oil recovery**. Richardson, TX: Henry L. Doherty Memorial Fund of AIME, Society of Petroleum Engineers, 2018.
- HAFEMANN, T. E.; FERREIRA, M. V. D.; BARBOSA Jr, J. R. Modeling of fluid flow and heat transfer in a pre-salt oil production well. **15th Brazilian Congress of Thermal Sciences and Engineering**, Belém, Pará, Brazil, 10–13 November 2014.
- HE, Zhiliang *et al.* Experiment of Carbonate Dissolution: Implication for High Quality Carbonate Reservoir Formation in Deep and Ultradeep Basins. **Geofluids**, vol. 2017, p. 1-8, 2017. Available from: <https://doi.org/10.1155/2017/8439259>.
- HERZOG, Howard J. **Carbon capture**. MIT Press, 2018.
- IEA. **CCUS in Clean Energy Transitions**. Paris, 2020. Available from: <https://www.iea.org/reports/ccus-in-clean-energy-transitions>. Accessed: 1 May 2022.
- IPCC (Intergovernmental Panel on Climate Change). **Carbon Dioxide Capture and Storage**: Special Report of the Intergovernmental Panel on Climate Change. [S. l.]: Cambridge University Press, 2005. 442 p. ISBN 9780521866439.
- KARAEI, M. A.; HONARVAR, B.; AZDARPOUR, A.; MOHAMMADIAN, E. CO<sub>2</sub> storage in low permeable carbonate reservoirs: permeability and interfacial tension (IFT) changes during CO<sub>2</sub> injection in an Iranian carbonate reservoir. **Periodica Polytechnica Chemical Engineering** **64** (4): 491-504. 2019. <https://doi.org/10.3311/PPch.14498>.
- KENDALL, Christopher G. St C.; FLOOD, Peter. Classification of Carbonates. *In*: **Encyclopedia of Modern Coral Reefs**. Dordrecht: Springer Netherlands, 2011. p. 193-198. ISBN 9789048126385. Available from: <https://doi.org/10.1007/978-90-481-2639->

## REFERENCES

2 269.

- KHAN, H. J.; PRODANOVIC, M.; DICARLO, D. A. The effect of vuggy porosity on straining in porous media. **SPE Journal** **24** (03): 1164-1178. 2019. <https://doi.org/10.2118/194201-PA>.
- KIRKHAM, Anthony; TUCKER, Maurice E. Thrombolites, spherulites and fibrous crusts (Holkerian, Purbeckian, Aptian): Context, fabrics and origins. **Sedimentary Geology**, v. 374, p. 69-84, 2018. Available from: <https://doi.org/10.1016/j.sedgeo.2018.07.002>.
- KOVACS, T.; POULUSSEN, D. F.; DE DIOS, C. Strategies for injection of CO<sub>2</sub> into carbonate rocks at Hontomin. Final Technical Report, **Global Carbon Capture and Storage Institute Ltd**, Melbourne, Australia. 2015.
- LEIDERMAN, Ricardo *et al.* Personal computer-based digital petrophysics. **Brazilian Journal of Geophysics**, v. 35, n. 2, p. 95-107, 2017. Available from: <http://dx.doi.org/10.22564/rbgf.v35i2.891>.
- LIMA, Bruno Eustáquio Moreira; DE ROS, Luiz Fernando. Deposition, diagenetic and hydrothermal processes in the Aptian Pre-Salt lacustrine carbonate reservoirs of the northern Campos Basin, offshore Brazil. **Sedimentary Geology**, v. 383, p. 55-81, 2019. Available from: <https://doi.org/10.1016/j.sedgeo.2019.01.006>.
- LOUËR, D. Powder X-Ray diffraction, applications. In: LINDON, J. C.; TRANTER, G. E., *et al* (Ed.). **Encyclopedia of Spectroscopy and Spectrometry**. Third Edition: Academic Press, v.3, 2017. p.723-731. ISBN 9780128032244.
- MARTÍNEZ-MARTÍNEZ, J.; BENAVENTE, D.; GARCÍA-DEL-CURA, M. A. Comparison of the static and dynamic elastic modulus in carbonate rocks. **Bulletin of engineering geology and the environment**, v. 71, n. 2, p. 263-268, 2012. Available from: <https://doi.org/10.1007/s10064-011-0399-y>.
- MCPHEE, Colin; REED, Jules; ZUBIZARRETA, Izaskun. **Core analysis: a best practice guide**. Elsevier, 2015. ISBN 9780444635334. Available from: <https://doi.org/10.1144/GSL.SP.2003.215.01.01>.
- MEES, Florias *et al.* Applications of X-ray computed tomography in the geosciences. **Geological Society, London, Special Publications**, v. 215, n. 1, p. 1-6, 2003. Available from: <https://doi.org/10.1029/2018JB016526>.
- MENG, Fanbao *et al.* The effect of stress on limestone permeability and effective stress behavior of damaged samples. **Journal of Geophysical Research: Solid Earth**, v. 124, n. 1, p. 376-399, 2019.

## REFERENCES

- METZ, B.; DAVIDSON, O.; DE CONINCK, H. C.; LOOS, M.; MEYER, L. IPCC special report on carbon dioxide capture and storage. Report, **Cambridge University Press**, Cambridge, UK. 2005.
- MILANI, Edison José *et al.* Bacias sedimentares brasileiras: cartas estratigráficas. **Boletim de Geociências da PETROBRAS**, v. 15, n. 2, p. 183-205, 2007.
- MME, ANP, PPSA, EPE, BNDES. **Study on the Use of the Pre-Salt Natural Gas**. Rio de Janeiro, 2020. Available from: <https://www.gov.br/anp/pt-br/centrais-de-conteudo/publicacoes/livros-e-revistas/arquivos/inglesaproveitamentognpresal.pdf>. Accessed: 19 May 2022.
- MOHAMED, Ibrahim Mohamed *et al.* Effects of Pressure, CO<sub>2</sub> Volume, and the CO<sub>2</sub> to Water Volumetric Ratio on Permeability Change during CO<sub>2</sub> Sequestration. In: ABU DHABI INTERNATIONAL PETROLEUM EXHIBITION AND CONFERENCE, Abu Dhabi, UAE. **Abu Dhabi International Petroleum Exhibition and Conference**. [S. l.]: Society of Petroleum Engineers, 2010. Available from: <https://doi.org/10.2118/136394-ms>.
- MOHRIAK, Webster Ueipass. Bacias sedimentares da margem continental Brasileira. **Geologia, tectônica e recursos minerais do Brasil**, v. 3, p. 87-165, 2003.
- NORTH, Laurence *et al.* Laboratory determination of the full electrical resistivity tensor of heterogeneous carbonate rocks at elevated pressures. **Geophysical Prospecting**, vol. 61, no. 2, p. 458-470, 7 Jan. 2013. Available from: <https://doi.org/10.1111/j.1365-2478.2012.01113.x>.
- O GLOBO. **Com megaleilão do pré-sal, Brasil atrai 93% da renda global de rodadas de petróleo**. 3 Nov 2019. Available from: <https://oglobo.globo.com/economia/com-megaleilao-do-pre-sal-brasil-atrai-93-da-renda-global-de-rodadas-de-petroleo-1-24058661>.
- OGILVIE, S. R. *et al.* Novel methods of permeability prediction from NMR tool data. **Dialog, London Petrophysical Society, London**, p. 1-14, 2002.
- OJOVAN, Michael I.; LEE, William M. Naturally occurring radionuclides. In: **An introduction to nuclear waste immobilization**. Oxford, UK: Elsevier Ltd, 2005. p. 43-52.
- ORHAN, Kaan (Ed.). **Micro-computed Tomography (micro-CT) in Medicine and Engineering**. Cham: Springer, 2020.
- OTSU, Nobuyuki. A threshold selection method from gray-level histograms. **IEEE transactions on systems, man, and cybernetics**, v. 9, n. 1, p. 62-66, 1979.

## REFERENCES

- PATUSCO, João Antonio Moreira *et al.* **Resenha Energética Brasileira**. 30 May 2020. Available from: <http://antigo.mme.gov.br/web/guest/secretarias/planejamento-e-desenvolvimento-energetico/publicacoes/resenha-energetica-brasileira>. Accessed: 21 July 2020.
- PERKINS, Ernie. **Fundamental geochemical processes between CO<sub>2</sub>, water and minerals**. Alberta Innovates–Technology Futures. Alberta, 2003.
- PIETZSCH, Raphael *et al.* Palaeohydrology of the Lower Cretaceous pre-salt lacustrine system, from rift to post-rift phase, Santos Basin, Brazil. **Palaeogeography, Palaeoclimatology, Palaeoecology**, v. 507, p. 60-80, 2018. Available from: <https://doi.org/10.1016/j.palaeo.2018.06.043>.
- PIZARRO, Jorge Oscar de Sant'Anna; BRANCO, Celso Cesar. Challenges in implementing an EOR project in the pre-salt province in deep offshore Brasil. In: **SPE EOR Conference at Oil and Gas West Asia**. OnePetro, 2012. Available from: <https://doi.org/10.2118/155665-MS>
- POPPE, Lawrence J. *et al.* A laboratory manual for X-ray powder diffraction. **US Geological Survey open-file report**, v. 1, n. 041, p. 1-88, 2001.
- RIDING, Robert. Microbialites, Stromatolites, and Thrombolites. In: RIDING, Robert. **Encyclopedia of Geobiology**. Dordrecht: Springer Netherlands, 2011. p. 635-654. ISBN 9781402092114. Available from: [https://doi.org/10.1007/978-1-4020-9212-1\\_196](https://doi.org/10.1007/978-1-4020-9212-1_196).
- RITCHIE, Hannah; ROSER, Max; ROSADO, Pablo. **Energy**. 2020. Available from: <https://ourworldindata.org/energy>. Accessed: 20 Aug. 2020.
- SCHÖN, Jürgen H. **Physical properties of rocks: Fundamentals and principles of petrophysics**. Elsevier, 2015.
- SEYYEDI, M.; MAHMUD, H. K. B.; VERRALL, M.; GIWELLI, A.; ESTEBAN, L.; GHASEMIZIARANI, M.; CLENNELL, B. Pore structure changes occur during CO<sub>2</sub> injection into carbonate reservoirs. **Scientific reports** **10** (1): 1-14. 2020. [https://doi.org/10.1016/s0196-8904\(96\)00268-3](https://doi.org/10.1016/s0196-8904(96)00268-3).
- SMITH, M. M.; SHOLOKHOVA, Y.; HAO, Y.; CARROLL, S. A. CO<sub>2</sub>-induced dissolution of low permeability carbonates. Part I: Characterization and experiments. **Advances in Water Resources** **62**: 370-387. 2013. <https://doi.org/10.1016/j.advwatres.2013.09.008>.
- SOHRABI, Mehran *et al.* Coreflooding studies to investigate the potential of carbonated water injection as an injection strategy for improved oil recovery and CO<sub>2</sub> storage. **Transport**

## REFERENCES

- in **porous media**, v. 91, n. 1, p. 101-121, 2012. Available from: <https://doi.org/10.1007/s11242-011-9835-5>.
- SUN, Yankun *et al.* Laboratory core flooding experimental systems for CO<sub>2</sub> geosequestration: An updated review over the past decade. **Journal of Rock Mechanics and Geotechnical Engineering**, v. 8, n. 1, p. 113-126, 2016. Available from: <https://doi.org/10.1016/j.jrmge.2015.12.001>.
- TIAB, Djebbar; DONALDSON, Erle C. **Petrophysics: Theory and Practice of Measuring Reservoir Rock and Fluid Transport Properties**. [S. l.]: Elsevier Science & Technology Books, 2011. 976 p. ISBN 9780123838490.
- UNFCCC (United Nations Framework Convention on Climate Change). **The Paris Agreement**. 18 April 2018. Available from: <https://unfccc.int/process-and-meetings/the-paris-agreement/the-paris-agreement>. Accessed: 19 May 2022.
- VELOSO, Fernanda ML *et al.* Outcrop scale reservoir characterisation and flow modelling of CO<sub>2</sub> injection in the tsunami and the barrier island—Tidal inlet reservoirs of the Camarillas Fm. (Galve sub-basin, Teruel, NE Spain). **International Journal of Greenhouse Gas Control**, v. 55, p. 60-72, 2016. Available from: <https://doi.org/10.1016/j.ijggc.2016.11.007>.
- WANG, Ying *et al.* Effective stress law for the permeability and deformation of four porous limestones. **Journal of Geophysical Research: Solid Earth**, v. 123, n. 6, p. 4707-4729, 2018. Available from: <https://doi.org/10.1029/2018JB015539>.
- ZHANG, Ronghua *et al.* Dissolution Kinetics of Dolomite in Water at Elevated Temperatures. **Aquatic Geochemistry**, vol. 13, no. 4, p. 309-338, 1 Nov. 2007. Available from: <https://doi.org/10.1007/s10498-007-9022-z>.